THE UNIVERSITY of ADELAIDE

Carbon dots engineered carbon nitride as green catalysts for environmental purification

By Yu Yao

School of Chemical Engineering

Faculty of Sciences, Engineering, and Technology

A thesis submitted for the degree of Master by Research

The University of Adelaide

April 2023

Contents

Abstract

The mitigation of environmental pollution is one of the hot topics in sustainable development. Diverse pollutants are posing a threat to human physical health and psychological development. Especially, the abuse of antibiotics and their discharge in the aqueous systems during the Covid-19 pandemic has caused great burdens to the ecosystem. Novel techniques have been developed to remove antibiotics from water, aiming to achieve high degradation efficiency with high-performance catalysts. In this project, we designed polymer dots (PDs) via a simple and low-cost method and used the PDs as a dopant (carbon or nitrogen) source to produce heterojunction metal-free catalysts. These catalysts were coupled with visible light or peroxymonosulfate (PMS) to treat pollutants in water. The systems are featured with no secondary contamination compared with metal-based catalysts. The cheap urea and citric acid were used as raw materials to synthesize PDs. Then, the obtained PDs were encapsulated by urea to generate carbon nitride with more carbon rings or nitrogen-doped carbons under low-temperature calcination without using a protective gas. During the synthesis, we controlled the PDs dose to produce two different metal-free catalysts with high catalytic activity in photocatalytic degradation and advanced oxidation processes for PMS activation. Without PDs, urea will be transferred into graphitic carbon nitride (CN). In contrast, urea will be transferred into a homojunction of CN with abundant carbon rings in the presence of PDs. These generated carbon rings greatly improve the optical property and catalytic performance. In addition, urea will be transformed into nitrogen-doped carbon upon adding overdosed polymer dots. The N-doped carbon can activate PMS to oxidize pollutants via radical and nonradical pathways. Both naproxen and 1,4-dihydro-2,6-dimethylpyridine-3,5dicarboxylate (1,4-DHP) are selected as the target contaminants in the aqueous solution for performance evaluation.

Chapter 1 provides an introduction of carbon dots in the environmental application and the structure of this thesis. Chapter 2 presents a literature review of carbon dots. We discussed its various fabrication methods from different parent materials, optical characteristics, and applications. Specifically, the carbon dots can be used in photocatalytic splitting water, production of hydrogen peroxide, photodegradation, and as a PMS activator for pollutant degradation. In Chapter 3, we report a carbon nitride modified with carbon rings for photocatalytic degradation of antibiotics. In this process, polymer dots covered by urea are calcinated at a low temperature to develop carbon rings in the planar structure of carbon nitride. The produced carbon rings significantly modulate the structure of CN and improve the optical characteristics to achieve outstanding photocatalytic performance. In Chapter 4, we further present an investigation of N-rich carbon materials obtained by adding excessive polymer dots in the urea precursor and conducting the same calcination process. We compared the physicochemical properties and performance of the derived N-doped carbon with CN, graphene plates and multi-wall carbon nanotube. The abundant nitrogen dopants and amorphous structure remarkably promoted the activity for PMS activation and degradation of 1,4-DHP. The conclusion is presented in Chapter 5, following by discussion of challenges and perspectives of carbon dots.

Declaration

I certify that this work contains no material which has been accepted for the award of any other degree or diploma in my name, in any university or other tertiary institution and, to the best of my knowledge and belief, contains no material previously published or written by another person, except where due reference has been made in the text. In addition, I certify that no part of this work will, in the future, be used in a submission in my name, for any other degree or diploma in any university or other tertiary institution without the prior approval of the University of Adelaide and where applicable, any partner institution responsible for the joint-award of this degree.

I acknowledge that copyright of published works contained within this thesis resides with the copyright holder(s) of those works.

I also give permission for the digital version of my thesis to be made available on the web, via the University's digital research repository, the Library Search and also through web search engines, unless permission has been granted by the University to restrict access for a period of time.

Name of Candidate: Yu Yao

Signature:

Date: 23rd March 2023

Acknowledgments

This thesis would not have come to fruition without the support and help from my supervisors, friends, and families. Here, I would like to express my gratitude to them all.

First and foremost, I would like to thank my principal supervisor, Dr. Xiaoguang Duan, for offering me professional suggestions and continuous support for my research. Under his supervision, I learned how to conduct research in the right way with a positive attitude. More importantly, he also enlightens me throughout my MPhil research with his enthusiasm, fortitude, and sagacity. I could not have these achievements without his generous encouragement and support. I sincerely appreciate my co-supervisor, Dr. Jinqiang Zhang, for his insightful suggestions and continuous encouragement.

Importantly, I am also grateful to my co-supervisor, Prof. Shaobin Wang, who allows me to join his group during my study and provides me tremendous help and suggestions with patience.

I would also like to acknowledge the Australian Government, The University of Adelaide for their support.

I am also grateful to the members in the group who give me many supports during my MPhil study. I express my thanks to Dr. Huayang Zhang, Dr. Wenjie Tian, Dr. Gang Nie, Dr. Yangyang Yang, Dr. Kunsheng Hu, Mr. Shiying Ren, Mr. Jingkai Lin, Mr. Shuang Zhong, Ms. Zhongshuai Zhu for their generous help and inspiring discussions.

Finally, I would express my heartfelt appreciation to my family, my parents Ying Yao and Jun Bu, and my wife, Vicky, for their forever love and support. I could not have completed my MPhil research without their unconditional trust and support. It would be a great pleasure to dedicate this thesis to my family. And my sincere gratitude goes to my dear friends in China and Australia for their support.

Chapter 1: Introduction

1.1 Significance of the Project

Humans have been using plenty of drugs as a precautionary measure to prevent the disease during the environmental crisis, especially during the Covid-19 pandemic [1]. Meanwhile, some contaminants due to daily consumption, such as drugs and antibiotics, are being exposed to the environment, and pose a threat to human health. These generated pollutants would also cause harmful consequences to soil and water resource [1]. It is still a challenge to explore a green and sustainable technology to remove these pollutants. Advanced Oxidation Process (AOP) is one of the promising strategies for treating wastewater environments, as it generates reactive oxygen species (ROS) in situ with high oxidative capacities to decompose the refractory organic pollutants [2, 3]. Recently, the persulfate-based AOPs have been intensively researched to remove the toxic and refractory contaminants in aqueous solution via generating diverse reactive oxygen species, such as peroxide ion radicals ($O_2^{\bullet-}$), hydroxyl radicals (•OH), and sulfate radicals ($SO_4^{\bullet-}$) [4]. Some active species are formed by the cleavage of the peroxide bond in persulfates (e.g., peroxymonosulfate-PMS and peroxydisulfate-PDS) through energy transfer [5, 6]. Normally, the theoretical redox potential of $SO_4^{\bullet-}$ (E°= 2.6 – 3.1 V) is greater than •OH (E°= 1.9 – 2.7 V), leading to faster oxidation of organic pollutants. The degradation regimes are typically associated with the generation of radical adduct, and transformation of electron and hydrogen atoms [7].

In AOPs, the oxidative efficiency of radicals is influenced by the presence of natural organic matters and inorganic anions in the background. These substances can give rise to a negative influence on practical remediation via scavenging ROS or forming secondary contaminants in the aqueous environment [7, 8]. Additionally, heterogeneous catalysts can mediate the generation of nonradical species by activating persulfate in aqueous solution, such as N-

doped carbon materials [9, 10]. The generation of nonradical species in AOPs includes three mainstreams of high-valent metal, singlet oxygenation and electron transfer [11].

PMS-based AOP is one of the promising technologies for the remediation of organic contaminants due to their high oxidation capacity and stability. The asymmetric structure PMS, as a typical persulfate salt, is widely used in the catalytic oxidation reactions through the cleavage of O-O bond of PMS [2]. Various activating methods have been identified to activate PMS, such as photothermal treatment, ultrasound, alkalines, heat, ultraviolet, piezoelectric methods, and catalysts. Among these activation techniques, photothermal and piezoelectric activations are novel and less frequently used routes. Metal and carbonaceous materials are commonly used catalysts and implemented in the activation of persulfate. For metals/oxides, metal leaching and the associated secondary contamination are key issues in traditional AOP systems [12]. Carbon catalysts are gaining increasing attention in catalysis due to their low cost, nontoxicity, environmental friendliness and abundant original resources [2, 13].

Carbonaceous materials, such as graphene oxide [14], reduced graphene oxide, N-graphene [10], N-carbon nanotubes [15], N-nondiamond [16], have become popular candidates to activate PMS and generate reactive oxygen species. In addition, carbon dots, as an emerging carbon material, have stimulated a strong impetus among researchers in the catalysis, due to the superior biocompatibility, physicochemical and great resistance toward acid and base [17]. There still exists controversy about their associated mechanism in environmental catalysis. Researchers have classified CDs into carbon quantum dots (CQDs), polymer dots (PDs), and carbon nanodots (CNDs). They typically exhibit a spherical morphology with a diameter below 10 nm, and some have obviously crystal structures [18]. CDs demonstrate excellent properties of absorption, bioluminescence, photoluminescence, and up-conversion [19, 20]. Compared with other metal quantum dots, CDs exhibited high biocompatibility and low

toxicity properties [21]. Moreover, when CDs are loaded onto supporting carriers such as CN, they present high resistance against acid and base and excellent light-harvesting properties. Therefore, developing high-performance photocatalytic catalysts based on CDs/CN is critical for photocatalytic degradation. The electrons and hole pairs generated by photons trigger the production of radicals, which attack the pollutants in the aqueous environment.

Herein, we have designed a simple and advanced method to synthesize CN with rich carbon rings and N-rich carbon materials, which are applied in photodegradation and PMS systems, respectively. Both the catalysts differ in their structure and chemical bonds due to varying amounts of PDs when pyrolysis together with urea and display excellent catalytic performance in the purification of aqueous solutions. With the development of advanced analytic technologies, various images and spectroscopic techniques have been utilized to study the transformation of structure and chemical bonds from CN to N-doped carbon, such as transmission electron microscopy (TEM), X-ray diffraction (XRD), and synchrotron-based X-ray absorption spectroscopy (XAS). Hence, the goal of this thesis is to research the use of PDs as the sources of carbon and nitrogen to incorporate carbon rings in CN or to induce N dopants in carbocatalysts. These catalysts can be used as metal-free catalysts to purify contaminated water via photocatalysis and persulfate chemistry.

1.2 Research Objectives

This project intends to develop a family of green, sustainable and low-cost carbon dots derived photocatalysts or AOP catalysts. The PDs growth with urea generates CN with carbon rings to decrease its bandgap and increase the conductivity of the composites, giving rise to improved performance in the treatment of organic contaminants in the aqueous solution. The detailed objectives for this project are listed below:

1. Fabrication of polymer dots with high luminescence and outstanding absorption properties via a simple hydrothermal method.

2. Using PDs to modify graphitic carbon nitride as a carbon composite to reduce the bandgap of CN.

3. Analysing the mechanism of CN-PDs for improved harvest of photons to excite generation and the separation of electrons and holes.

4. Probing the mechanisms of naproxen degradation in the CN-$PDs_{0.1}$ photocatalytic system.

5. Synthesis and characterisation of N-doped carbon derived from urea and PDs using advanced characterisation techniques.

6. Researching the mechanism of PMS activation by N-doped carbon for the degradation of 1,4-DHP via heterogeneous catalysis.

1.3 Thesis Outline

This thesis is presented in the form of journal publications. The results of the reaction mechanisms study are included. Specifically, chapters in the thesis are presented in the following sequence:

Chapter 1 presents an introduction to this thesis, emphasising the significance of this project and outlining the research objectives.

Chapter 2 reviews the recent progress and challenges of carbon dots based catalysts for environmental purification.

Chapter 3 shows the polymer dots derived carbon nitride composites for enhanced photodegradation of naproxen.

Chapter 4 reports investigation of the poly mer dots as a nitride source to derive N-rich carbon for catalytic activation of PMS and degradation of pollutants.

Chapter 5 shows the conclusion and perspectives for further work on the design, fabrication and application of CDs for the environmental area.

1.4 References

[1] Heydargoy, Mohammad Hossein. The effect of the prevalence of COVID-19 on arbitrary use of antibiotics. Iran. J. Med. Microbiol. 14, no. 4 (2020): 374-378.

[2] N. Li, R. Li, X. Duan, B. Yan, W. Liu, Z. Cheng, G. Chen, L. Hou, S. Wang, Correlation of active sites to generated reactive species and degradation routes of organics in peroxymonosulfate activation by Co-loaded carbon, Environ. Sci. Technol. 55 (2021) 16163-16174.

[3] X. Duan, H. Sun, S. Wang, Metal-free carbocatalysis in advanced oxidation reactions, Acc. Chem. Res. 51 (2018) 678-687.

[4] P. Shao, Y. Jing, X. Duan, H. Lin, L. Yang, W. Ren, F. Deng, B. Li, X. Luo, S. Wang, Revisiting the graphitized nanodiamond-mediated activation of peroxymonosulfate: Singlet oxygenation versus electron transfer, Environ. Sci. Technol. 55 (2021) 16078-16087.

[5] W. Ren, L. Xiong, G. Nie, H. Zhang, X. Duan, S. Wang, Insights into the electron-transfer regime of peroxydisulfate activation on carbon nanotubes: The role of oxygen functional groups, Environ. Sci. Technol. 54 (2020) 1267-1275.

[6] W. Ren, G. Nie, P. Zhou, H. Zhang, X. Duan, S. Wang, The intrinsic nature of persulfate activation and N-doping in carbocatalysis, Environ. Sci. Technol. 54 (2020) 6438-6447.

[7] S. Zhu, X. Huang, F. Ma, L. Wang, X. Duan, S. Wang, Catalytic removal of aqueous contaminants on N-doped graphitic biochars: inherent roles of adsorption and nonradical mechanisms, Environ. Sci. Technol. 52 (2018) 8649-8658.

[8] P. Shao, S. Yu, X. Duan, L. Yang, H. Shi, L. Ding, J. Tian, L. Yang, X. Luo, S. Wang, Potential difference driving electron transfer via defective carbon nanotubes toward selective oxidation of organic micropollutants, Environ. Sci. Technol. 54 (2020) 8464-8472.

[9] X. Duan, H. Sun, Y. Wang, J. Kang, S. Wang, N-Doping-induced nonradical reaction on single-walled carbon nanotubes for catalytic phenol oxidation, ACS Catal. 5 (2014) 553-559.

[10] X. Duan, Z. Ao, H. Sun, S. Indrawirawan, Y. Wang, J. Kang, F. Liang, Z. Zhu, S. Wang, Nitrogen-doped graphene for generation and evolution of reactive radicals by metal-free catalysis, ACS Appl. Mater. Interfaces 7 (2015) 4169-4178.

[11] W. Ren, C. Cheng, P. Shao, X. Luo, H. Zhang, S. Wang, X. Duan, Origins of electron-transfer regime in persulfate-based nonradical oxidation processes, Environ. Sci. Technol. 56 (2022) 78-97.

[12] S. Zhu, X. Li, J. Kang, X. Duan, S. Wang, Persulfate activation on crystallographic manganese oxides: mechanism of singlet oxygen evolution for nonradical selective degradation of aqueous contaminants, Environ. Sci. Technol. 53 (2019) 307-315.
[13] X. Duan, Z. Ao, L. Zhou, H. Sun, G. Wang, S. Wang, Occurrence of radical and nonradical pathways from carbocatalysts for aqueous and nonaqueous catalytic oxidation, Appl. Catal. B: Environ. 188 (2016) 98-105.
[14] X. Duan, H. Sun, Z. Shao, S. Wang, Nonradical reactions in environmental remediation processes: Uncertainty and challenges, Appl. Catal. B: Environ. 224 (2018) 973-982.
[15] W. Ren, L. Xiong, X. Yuan, Z. Yu, H. Zhang, X. Duan, S. Wang, Activation of peroxydisulfate on carbon nanotubes: electron-transfer mechanism, Environ. Sci. Technol. 53 (2019) 14595-14603.
[16] X. Duan, H. Sun, S. Wang, Comment on Activation of persulfate by graphitized nanodiamonds for removal of organic compounds, Environ. Sci. Technol. 51 (2017) 5351-5352.
[17] W. Han, D. Li, M. Zhang, H. X, X. Duan, S. Liu, S. Wang, Photocatalytic activation of peroxymonosulfate by surface-tailored carbon quantum dots, J. Hazard. Mater. 395 (2020) 122695.
[18] A. Rasal, S. Yadav, A. Yadav, A. Kashale, S. Manjunatha, A. Altaee, Jia. Chang, Carbon quantum dots for energy applications: a review, ACS Appl. Nano Mater. 4 (2021) 6515-6541.
[19] S. Lim, W. Shen, Z. Gao, Carbon quantum dots and their applications, Chem. Soc. Rev. 44 (2015) 362-381.
[20] J. Liu, R. Li, B. Yang, Carbon dots: A new type of carbon-based nanomaterial with wide applications, ACS Cent. Sci. 6 (2020) 2179-2195.
[21] C. Hu, M. Li, P. Qiu, Y. Sun, Design and fabrication of carbon dots for energy conversion and storage, Chem. Soc. Rev. 48 (2019) 2315-2337.

Chapter 2: Literature Review

2.1 Introduction and Significance

This chapter introduces the category of carbon dots (CDs), synthesis methods and physical characteristics. In addition, the chapter summarizes various photocatalytic applications, such as hydrogen evolution reaction, hydrogen peroxide production, activation of peroxymonosulfate, and photodegradation. The demand for an improved quality of life has led to rapid advancements in sustainable development. As a result, there has been extensive research on novel catalytic materials as a means of achieving a clean and sustainable environment. Due to their excellent and unique optical properties, metal-free nature, and redox properties, carbon materials have recently shown great potential in environmental purification. Carbon materials, due to their environmental friendliness and sustainability, have served as metal-free catalysts to replace conventional metal catalysts. Carbon dots have a wide range of applications in chemical and biological fields. Applications of CDs include photocatalysis, biosensing, chemical sensing and photodynamic therapy. This chapter provides a comprehensive summary of the recent advances in the applications of CDs in various photocatalytic systems. The chapter places a particular emphasis on the development of materials design principles and catalytic mechanisms. These applications include the production of hydrogen and hydrogen peroxide, activation of PMS, and purification of organic pollutants in water. Furthermore, this chapter discusses the engineering perspectives of carbon dots and the challenges associated with their synthesis and mechanistic studies.

2.2 Carbon dots based photocatalysis for environmental applications

This Chapter is included as it appears as a journal paper published by **Yu Yao**[a], Huayang Zhang[a,*], Kunsheng Hu[a], Gang Nie[b], Yangyang Yang[a], Yuxian Wang[c], Xiaoguang Duan[a,*], Shaobin Wang[a]* Carbon dots based photocatalysis for environmental applications, J. Environ. Chem. Eng. 10 (2022) 107336.

Statement of Authorship

Title of Paper	Carbon dots based photocatalysis for environmental applications
Publication Status	☑ Published ☐ Accepted for Publication ☐ Submitted for Publication ☐ Unpublished and Unsubmitted w ork w ritten in manuscript style
Publication Details	Yu Yao, Huayang Zhang, Kunsheng Hu, Gang Nie, Yangyang Yang, Yuxian Wang, Xiaoguang Duan* , Shaobin Wang* Carbon dots based photocatalysis for environmental applications. J. Environ. Chem. Eng. 10 (2022) 107336.

Principal Author

Name of Principal Author (Candidate)	Yu Yao		
Contribution to the Paper	Project design and manuscript drafting.		
Overall percentage (%)	60%		
Certification:	This paper reports on original research I conducted during the period of my Higher Degree by Research candidature and is not subject to any obligations or contractual agreements with a third party that would constrain its inclusion in this thesis. I am the primary author of this paper.		
Signature		Date	20 / 03 / 2023

Co-Author Contributions

By signing the Statement of Authorship, each author certifies that:

i. the candidate's stated contribution to the publication is accurate (as detailed above);

ii. permission is granted for the candidate in include the publication in the thesis; and

iii. the sum of all co-author contributions is equal to 100% less the candidate's stated contribution.

Name of Co-Author	Shaobin Wang		
Contribution to the Paper	Supervision of the work, discussion of this manuscript and manuscript evaluation.		
Signature		Date	21/3/2023

Name of Co-Author	Xiaoguang Duan		
Contribution to the Paper	Supervision of the work, discussion of this manuscript and manuscript evaluation.		
Signature		Date	21/3/2023

Name of Co-Author	Kunsheng Hu		
Contribution to the Paper	Discussion and revision of manuscript.		
Signature		Date	20 / 03 / 2023

Name of Co-Author	Yangyang Yang		
Contribution to the Paper	Discussion and revision of manuscript.		
Signature		Date	20 / 03 / 2023

Name of Co-Author	Gang Nie		
Contribution to the Paper	Discussion and revision of manuscript.		
Signature		Date	20/03 /2023

Name of Co-Author	Huayang Zhang		
Contribution to the Paper	Discussion and revision of manuscript.		
Signature		Date	21/03 /2023

Name of Co-Author	Yuxian Wang		
Contribution to the Paper	Discussion and revision of manuscript.		
Signature		Date	21/03 /2023

Journal of Environmental Chemical Engineering 10 (2022) 107336

Contents lists available at ScienceDirect

Journal of Environmental Chemical Engineering

journal homepage: www.elsevier.com/locate/jece

Carbon dots based photocatalysis for environmental applications

Yu Yao [a], Huayang Zhang [a], Kunsheng Hu [a], Gang Nie [b], Yangyang Yang [a], Yuxian Wang [c], Xiaoguang Duan [a,*], Shaobin Wang [a,*]

[a] School of Chemical Engineering and Advanced Materials, The University of Adelaide, North Terrace, Adelaide, SA 5005, Australia
[b] Department of Environmental Science and Engineering, Wuhan University, Wuhan 430079, PR China
[c] State Key Laboratory of Heavy Oil Processing, China University of Petroleum-Beijing, 18 Fuxue Road, Beijing 102249, PR China

ARTICLE INFO

Editor: Teik Thye Lim

Keywords:
Carbon quantum dots
Photocatalysis
Hydrogen
Hydrogen peroxide
Pollutant removal

ABSTRACT

Carbon quantum dots (CQDs) have attracted intensive interest in the scientific community attributed to their quantum effect, non-toxicity, fluorescence, photoluminescence, and up-conversion properties, and have been extensively applied in sensing, biomedical, optoelectronic and catalysis fields. Especially, CQDs can act as photocatalysts and be used in energy and environmental areas, such as wastewater remediation and solar energy conversion to fuels and green chemicals. This review will briefly introduce the unique physicochemical properties of CQDs, such as light absorption, photoluminescence, and up-conversion luminescence. The advanced fabrication methods and modification strategies of CQDs will also be summarized. Finally, we will show the broad applications of CQDs in photocatalytic pollutant removal and hydrogen/hydrogen-peroxide production, discussing the structure-activity relationship of CQDs and their complexes in the field of catalysis. Lastly, the key issues and perspectives for future energy and environmental applications are presented. This comprehensive review will provide new insight and inspiration in the synthesis, improvement, and photocatalytic application of CQDs.

1. Introduction

Energy crisis and environmental pollution are the two main challenges for human sustainable developments due to the rapid growth of population and high demand for daily consumables [1,2]. Advanced and renewable technologies can help address the issues. Photocatalysis is appealing because of its clean process and use of inexhaustible solar energy, which will not cause further burdens on the environment [3–6]. Photocatalysts are typically semiconductors that can be excited under light irradiation to generate charge carriers of highly oxidative holes and reductive electrons for different redox reactions. II–VI group quantum dots (QDs) and Cd-free I-III-VI QDs have been regarded as the most promising candidates, thanks to the unique quantum confinement effect, a large surface area, and excellent optical properties. Some traditional QDs have drawn more attention in photocatalysis due to their tuneable band gap by the composition. However, these photocatalysts perform low production efficiency and poor stability. This shortcoming may be ascribed to the ability of low charge separation and photo-corrosion in I-III-VI QDs [7].

Carbon quantum dots (CQDs, also called carbon dots or CDs) are zero-dimensional and quasi-spherical dots composed of crystalline/amorphous carbons. Defined by the size and features, carbon quantum dots are below 10 nm with a crystalline structure and fluorescence characteristic, while the size of carbon dots may range from nm to mm (including CQDs) [8]. The uniform-sized CQDs can be obtained from CDs by the dialysis method. CQDs have been appealing to industry and academia due to their merits of inexpensiveness, facile scale-up synthesis [9,10], low toxicity [11,12], tuneable fluorescence [13], good environmental compatibility, electron reservoir [14] and transport [15], as well as unique up-converted photoluminescence (PL) performance [16]. Most CQDs have a carbon core inside and abundant functional groups on the external surface, such as epoxy, hydroxyl, carbonyl and carboxyl, groups. These functional groups endow CQDs with high water solubility and PL quantum properties [17]. More importantly, these functional groups afford CQDs to be widely employed in biomedicine [12], optoelectronic devices [18], anti-counterfeiting [19], and sensors [20]. Also, CQDs are used in emerging fields such as energy conversion and environmental purification [21,22]. Compared to g-C_3N_4-based quantum dots, CQDs can be fabricated in a large scale with well-defined defects, which are the vital factor to determine their optical and

* Corresponding authors.
E-mail addresses: xiaoguang.duan@adelaide.edu.au (X. Duan), shaobin.wang@adelaide.edu.au (S. Wang).

https://doi.org/10.1016/j.jece.2022.107336
Received 27 December 2021; Received in revised form 1 February 2022; Accepted 3 February 2022
Available online 8 February 2022

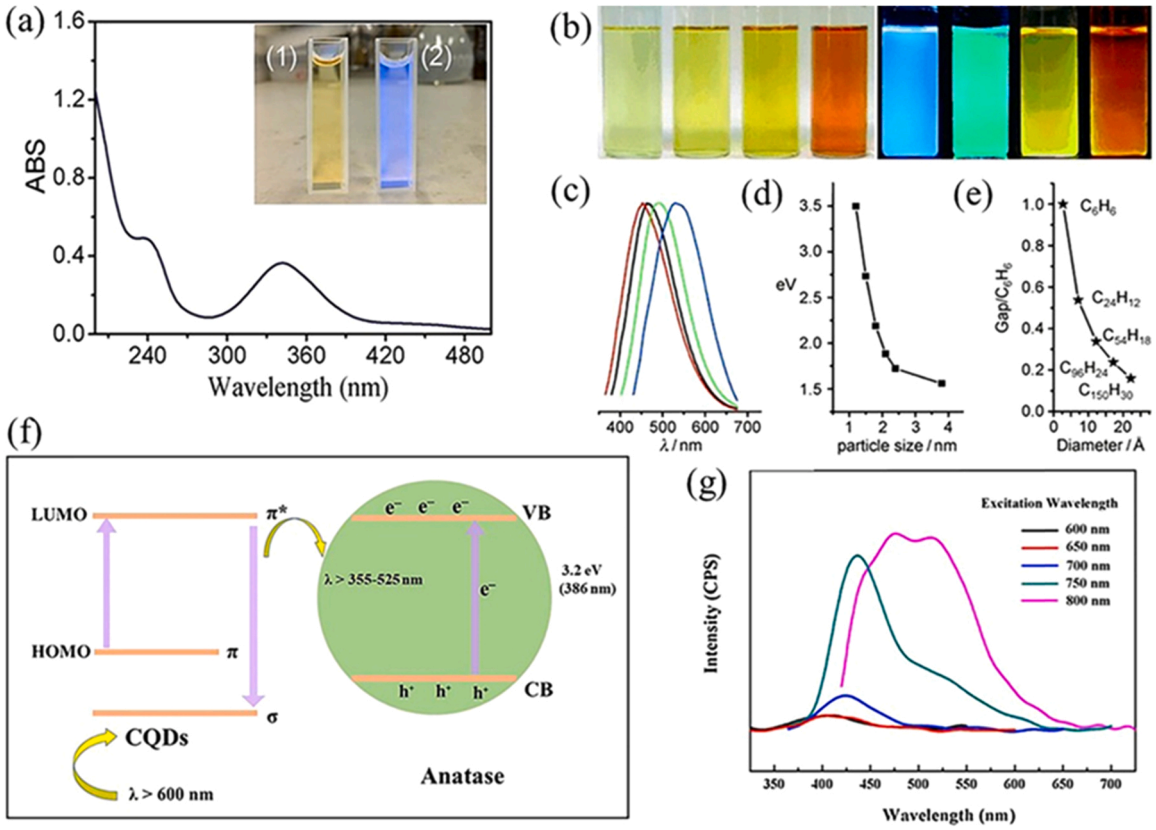

Fig. 1. (a) UV–vis absorption spectra [14]. Copyright 2018, Elsevier. (b) The optical images for CQDs shown under irradiation of a daytime lamp (Left) and UV light with the frequency of 365 nm (Right); (c) Photoluminescence spectra for typical sized CQDs: the red, black, green, and blue color lines successively refer to the PL spectra for blue-, green-, yellow-, and red emission of CQDs; (d) Change of PL properties relative to the size of CQDs; (e) HOMO-LUMO gap corresponds to the size of graphene fragments [50]. Copyright 2010, Wiley Online Library. (f) Modified schematic illustration of electronic transition of CQDs. (g) The property of up-converted PL spectra of CQDs [29]. Copyright 2016, Elsevier

electronic properties. In addition, modifications such as functionalization and heteroatom doping can be easily achieved during CQDs synthesis or post-treatment. The low toxicity, high solubility, tuneable property, and outstanding performances render CQDs ideal candidates in environmental applications such as monitoring (used in sensors) and purification in the aqueous phase [23].

CQDs are organic semiconductors that can be excited by sunlight to produce photoinduced electron-hole pairs. Additionally, CQDs can act as electron donors and acceptors in either solution or suspension, serving as a critical medium of energy shuttle. CQDs have been hence extensively used in photocatalysis for the production of hydrogen [24, 25] and hydrogen peroxide [26,27], conversion of CO_2 into value-added hydrocarbons [28–33], and purification of organic contaminants in water [34–36]. Herein, we will present a concise and critical overview of the fundamental optical and physical characteristics of CQDs and their dominant synthesis methods. We will also showcase the advanced applications of CQDs and CQDs-based nanocomposites as green and sustainable photocatalysts in solar energy conversion and environmental remediation, such as hydrogen and hydrogen peroxide production and degradation of aqueous organic pollutants (e.g., pharmaceuticals and dyes), especially in the advanced oxidation processes (AOPs) by coupling CQDs with persulfates. The unique optical properties, electronic regulatory ability, and abundant active sites of CQDs, as well as their structure-activity relationship in catalytic reactions will be mainly analyzed. Last, we will present the challenges and prospects of CQDs in these dynamic areas to state some inspiration for the exploitation of CQDs.

2. Optical properties of CQDs

2.1. Light absorption

The light absorption of CQDs is usually in the range of 240–320 nm, which can be extended to a small part of the visible light region. Fig. 1a shows the UV–vis absorption and fluorescence emission of CQDs, which present two characteristic peaks centered at 235 and 330 nm separately, due to electronic transitions of $\pi = \pi^*$ (C═C) and $n = \pi^*$ (C═O/C═N) bands, respectively [37,38]. CQDs have a low absorption intensity in the visible and near infrared regions, due to a long-wavelength light absorption capacity of 500–800 nm by some groups or π conjugated electrons in the sp^2 region connected to the surface CQDs [39–41]. Under 365 nm UV irradiation, bright blue luminescence could be observed on the CQDs suspension (Fig. 1a, inset), revealing that CQDs exhibit down-conversion fluorescent properties [14]. Absorption features of CQDs are determined by the content/types of surface functionality, dopants in the carbon core, and size of π-conjugated domains [42], which can be modulated by synthesis methods and different precursors.

2.2. Photoluminescence and up-conversion photoluminescence

The photoluminescence (PL) of CQDs has raised great enthusiasm in the field of photocatalysis [43]. However, the mechanism has not yet been well understood so far [44]. Sun et al. obtained CQDs by laser ablation and surface passivation of polyethylene glycol (PEG). For the first time, the organic polymer chain was attached to CQDs by a surface modification approach to realize the photoluminescence of CQDs [45].

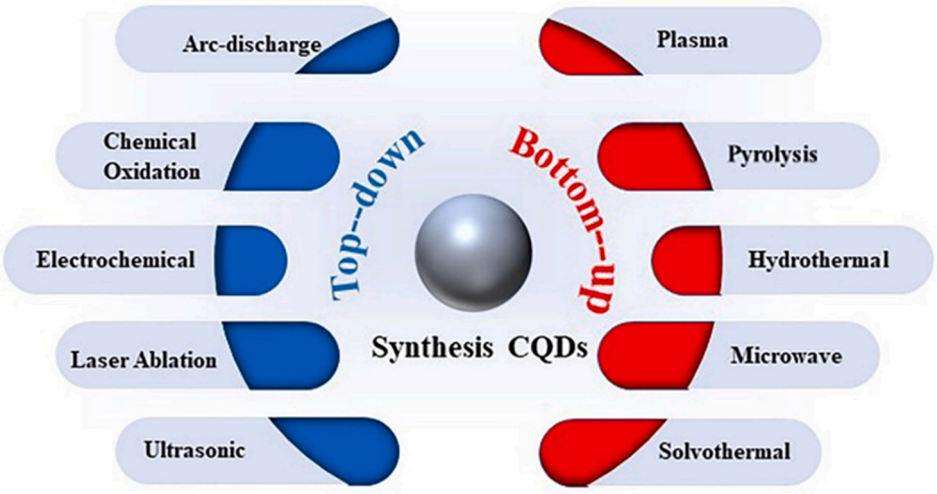

Scheme 1. A summary of CQds synthesis via bottom-up and top-down approaches.

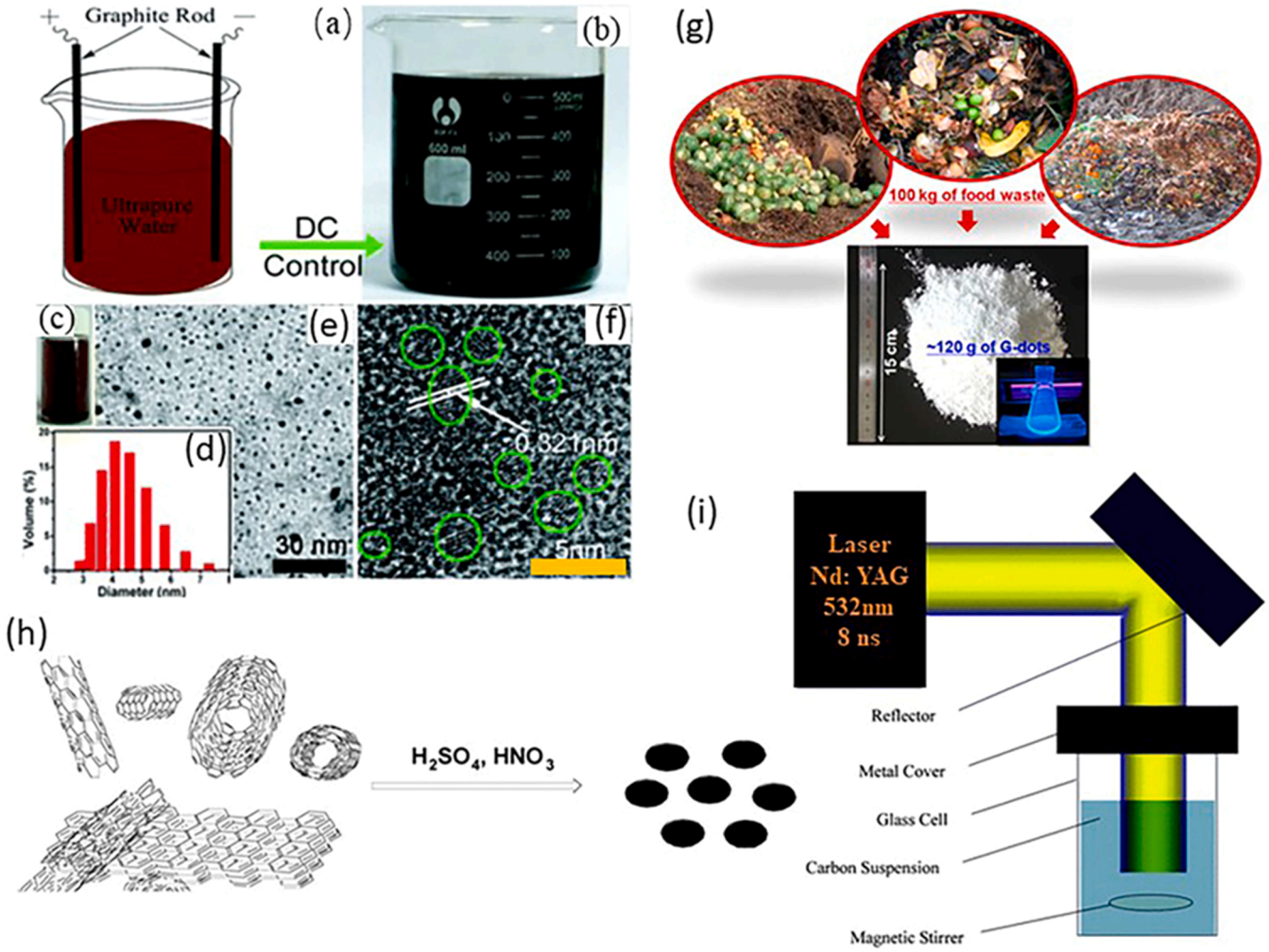

Fig. 2. (a) The simple electrochemical reaction setup for C-dots synthesis after treatment; digital image of C-dots solution (b) before and (c) after treatment; (d) indicated histogram of the average size for C-dots; (e) TEM of CDs, (f) HRTEM image of CDs [62]. Copyright 2012, Royal Society of Chemistry. (g) schematic description using ultrasonic irradiation to synthesis G-dots with waste food [59]. Copyright 2014, America Chemistry Society. (h) diagram of chemical reactions with different carbon-based materials, including single-wall carbon nanotube, graphite, and multi-wall carbon nanotube [60]. Copyright 2012, Wiley Online Library. (i) illustration of the CQDs preparation via laser ablation pathway [64]. Copyright 2011, Royal Society of Chemistry.

The photoluminescence yield of these quantum dots is mainly formed by the degree of passivation, precursors, and synthetic routes [46,47]. Meanwhile, the obvious red shift of emission peaks was witnessed within the wavelength range between 440 and 520 nm under light irradiation [48]. It is feasible to control the PL property of CQDs via tuning the excitation wavelength without changing the chemical structure and size, which is favorable in multi-color bioimaging [37,45]. The value of emitting quantum yield (QY) depends on the PL brightness of CQDs, which mainly depends on carbon precursors and synthetic pathways [49]. Fig. 1b displays optical images of CQDs in four different sizes under UV and white light. Fig. 1c shows the intensity of the emission spectra of different colors. Fig. 1d indicates that the PL of CQDs changes significantly with the size of CQDs. The CQDs around 1.2 nm can emit 350 nm UV light and CQDs at a size range of 1.5–3 nm emit visible light (400–700 nm), while CQDs (over 3.8 nm) give near-infrared emission.

The strong PL emission of CQDs is also dependent on their size and structure of quantum-grade graphite in CQDs structure [50]. Fig. 1e shows that the HOMO–LUMO gap of CQDs is impacted by the size of the graphene fragment structure in CQDs. Detailly, the HOMO–LUMO gap will diminish when the magnitude of the fragment increases [51]. Graphene fragments, at a diameter between 14 and 22 Å, enable the CQDs to have the gap energy in the visible range, which corresponds to the visible light emission of the CQDs. Also, it is effective to control the PL emission of CQDs by regulating the surface defects and functional groups. Shen et al. reported that functionalized defects and sp^2/sp^3 carbons [19] (e.g., carbonyl group) may result in multi-color emission [19,52]. These multi-colors mainly fall in the green and blue regions in the visible light spectrum [53]. Moreover, Song et al. prepared CDs and applied them as sensors for detecting H_2O_2 at a low limit of detection (0.9 ppb). The PL property and high quantum yield of CDs are mainly determined by their molecular state, and the dynamic PL could be quenched by ferrous ions and hydroxyl radicals due to the oxidation of the PL center [54]. Additionally, a higher surface oxidation degree will generate more surface defects, and some may even result in a redshift of PL emissions [55].

Up-conversion photoluminescence (UCPL) requires an energy difference of close to 1.1 eV between the excited and emitted light. Photons with lower energy can stimulate the electrons in the π orbital to a higher energy level, and up-conversion photoluminescence can be emitted when electrons fall into the σ orbital (Fig. 1f) [29]. Cao et al. observed that some CQDs have UCPL emission properties [56]. They used a pulsed laser with 800 nm (femtosecond) to excite CQDs, emitting visible light with a shorter wavelength (300–700 nm). The up-converted quantum effects are mainly derived from the active multiphoton processes that absorb two or more photons [29,57]. As shown in Fig. 1g, the up-conversion emission peak shows an apparent redshift (from 355 to 525 nm) when the excitation wavelength gradually increases from 600 to 800 nm. It has been studied that the photocatalytic activity of CQDs can be regulated by their unique UCPL properties [58].

3. Synthesis methods

Compared to metal-based quantum nanomaterials, CQDs can be produced on a large scale from various carbon-based precursors with a low cost and via some straightforward methods. Many synthesis methods are based on carbonization and post-functionalization of carbon-rich organic molecules. Scheme 1 summarizes the representative synthesis approaches of CQDs via bottom-up and top-down strategies.

3.1. Top-down

The top-down approaches are mainly for decomposition of massive carbonaceous materials into nano-sized particles under different reaction conditions such as oxidation, high temperature/pressure, or a strong acidic environment. Common top-down methods are generally involved in electrochemical oxidation [50], ultrasonic exfoliation [59], chemical oxidation [60,61], and laser ablation [45]. For instance, (quasi-) 0D-CQDs with sizes less than 10 nm can be synthesized via the exfoliation of carbon-based materials with different dimensions of carbon black, carbon nanotube (CNT) and graphene under strong oxidation conditions [46].

Li et al. reported a simple electrochemical process for generating high-quality CQDs in a mixture of alkaline ethanol/water solution using graphite rods as cathode and anode [50]. The derived CQDs were in a size range of 1.2–3.8 nm, which exhibited excellent UCPL properties and a high PL quantum yield of 12%. These CQDs can be used as fluorescent markers and high-efficient catalysts in bioscience and energy technologies. Composites based on these CQDs, such as TiO_2/CQDs and SiO_2/CQDs, can fully utilize the UCPL features to leverage the full spectrum of sunlight [50]. Ming et al. presented a facile electrochemical approach in producing high purity CQDs. In this system, pure water was selected as the electrolyte, while graphite rods were used as the anode and cathode at a DC power supply of 15–60 V (Fig. 2a). The dark yellow solution in Fig. 2b mainly contains CQDs of different sizes and a large amount of graphite oxide. After treatment, the CQDs aqueous suspension displayed light brown color (Fig. 2c). As shown from Fig. 2d and e, the average diameter of CQDs is about 4.5 nm and the CQDs were well dispersed in the aqueous solution. Fig. 2f reveals that crystal lattice spacing of CQDs is about 0.321 nm by the high-resolution transmission electron microscopy (HRTEM). These CQDs have decent photo-response to visible light, making them promising components for advanced photocatalyst construction [62].

Ultrasonication leads to the formation and collapse of vacuum bubbles due to the alternant generation of lower and higher-pressure waves in the liquid phase and has been utilized in the preparation of CQDs [43,63]. Under ultrasound irradiation, a series of dehydration, polymerization, and carbonization reactions will lead to a short burst of carbon nucleation and then nuclei growth into nanoparticle. As an example, Park and co-workers used waste foods as the precursor to fabricate green carbon nanodots (G-dots) at room temperature via an ultrasonic method (Fig. 2g) [59]. These G-dots demonstrated excellent solubility in aqueous solution due to the high contents of surface oxygen-containing groups. The simple and environmental-friendly method allows for mass production of green CQDs with a general size of 2–4 nm. The G-dots showed good size uniformity, photoluminescence properties, high photostability, and non-toxicity, making them appropriate for biomedical applications.

Chemical oxidation can feasibly produce CQDs without complicated devices. Tao et al. developed CQDs via a chemical oxidation method using three carbon precursors of single-walled CNTs (SWCNTs), multi-walled CNTs, and graphite. An acid mixture with a 3:1 ratio of sulfuric to nitric acid was used (Fig. 2h) [60]. Atomic force microscopy (AFM) revealed that the three CQDs samples were nanoparticles with diameters between 2 and 3 nm. After removing graphite and CNTs residues via refluxing and filtering, the obtained transparent liquid exhibited a yellow fluorescence emission under UV light irradiation. The obtained solution stayed high stability in physiological solutions. The aqueous solutions with dispersed CQDs can be reserved at normal temperature for nearly one year without any fluorescence loss or any generation of precipitates.

Laser ablation has been widely used to prepare CQDs with various nanostructures and morphologies [56,65]. A setup of CQDs synthesis by laser ablation is shown in Fig. 2i. A certain quantity of nano-carbon materials were poured into the solvent (water, ethanol or acetone) for continuously ultrasonicating, and this solvent was covered by the glass cell under the laser irradiation with the wavelength of 532 nm. The magnetic stirring was also used to reduce gravitational setting of pristine carbon materials. After the laser irradiation, the CQDs contained in the supernatants would be received by deposited on the copper grid [64]. Sun and his colleagues also used a pulsed laser to ablate a mixture of graphite-carbon and cement, which were then baked, cured, and

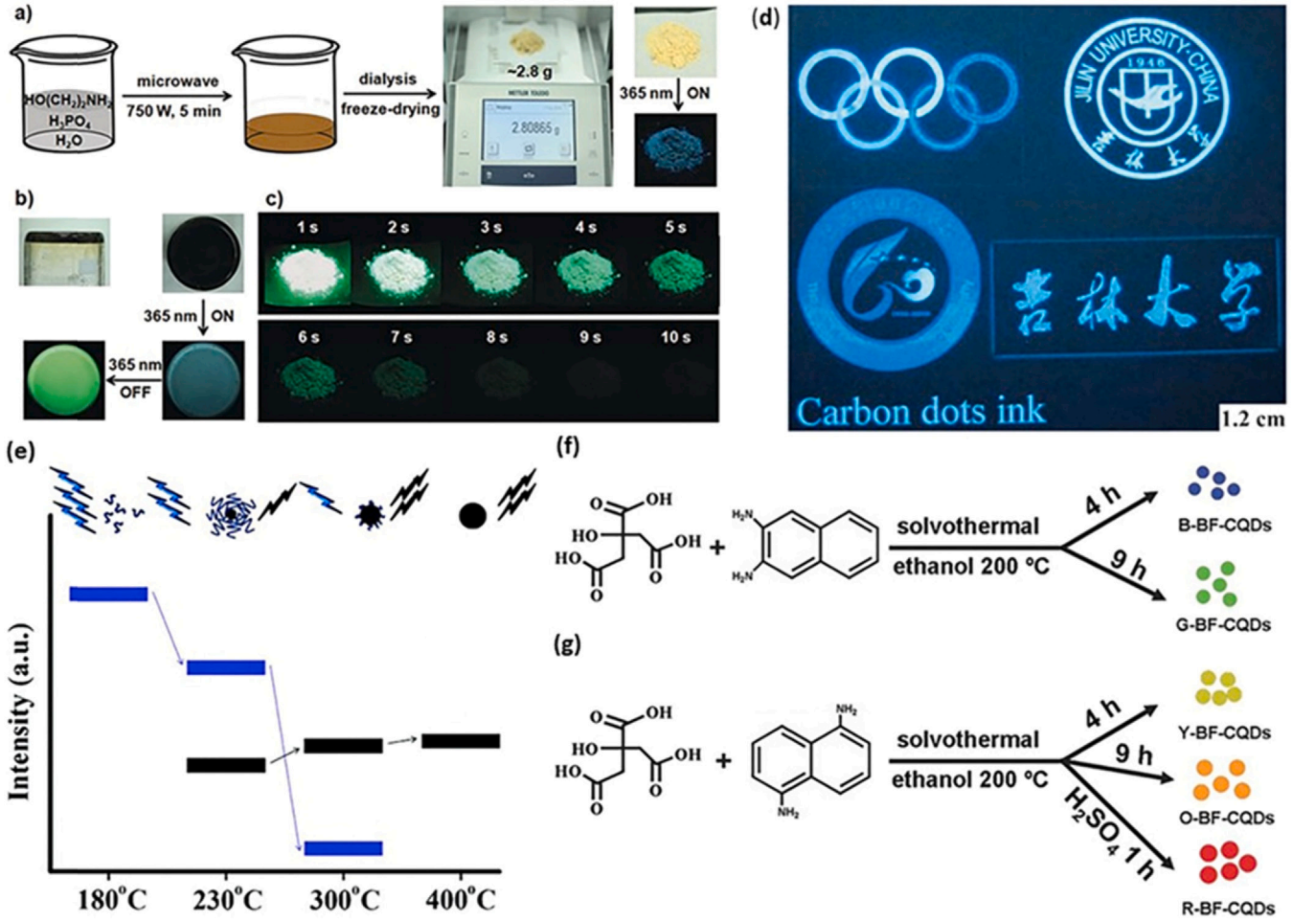

Fig. 3. (a) Schematic illustration of the CQDs preparation process in ultralong-room temperature for the (URTP) CQDs. Gram-scale product (ca. 2.8 g) can be obtained from a mixture of ethanolamine (4.0 mL), phosphoric acid (8.0 mL), and water (16 mL) under microwave irradiation (750 W) for 5 min. The mixture was subsequently purified by dialysis and freeze-drying. Right side: the purified URTP CQDs powder under daylight and 365 nm UV lamp. (b) Side-view and bottom-view images of the prepared CQDs in a beaker under ambient daylight indicated under a 365 nm UV lamp ON and OFF, respectively. (c) Corresponding afterglow images of the purified URTP CQDs powder after the UV lamp (365 nm) irradiating for 1–10 s under normal temperature conditions [11]. Copyright 2018, Wiley Online Library. (d) CQDs used in the ink and coupled with polymers, and some graphitic patterns were attached on the papers (UV light was used to illuminate CQDs) [37]. Copyright 2013, Wiley Online Library. (e) The pyrolysis of the mixture of citric acid (CA) and EA. The carbogenic core (black sphere) was built up by consuming the organic fluorophores (blue groups) to form PL component [73]. Copyright 2011, American Chemical Society. (f and g) Solvothermal methods for the fabrication of MCBF-CQDs with colours from blue to red by using CA and DAN as the precursor [41]. Copyright 2016, Wiley Online Library.

annealed to get CQDs. This reaction proceeded under argon atmosphere, where argon acted as the gas carrier in a water vapor system under harsh conditions (900 °C and 75 kPa). The aqueous CQDs synthesized by the pulsed laser exhibited higher photoluminescence properties. However, no luminescence was observed when CQDs were further treated with a nitric acid solution for 12 h. Importantly, CQDs can be treated with an acid to allow organic species to adhere to their surfaces, and their acid solution can emit bright luminescence [45].

An arc-discharge method requires a huge amount of energy to produce CQDs. Xu et al. [66] synthesized three types of carbon nanoparticles via the arc discharge method using SWCNTs as the raw material in a sealed reactor. The setup of the sealed reactor was consisted of plasma, anode electrode, and high voltage, and the decomposition mainly occurred at the anode electrode of plasma under a high voltage. Electrolyte solution was a mixture of isopropanol and deionized water with a volume ratio of 1:4. Both electrodes are connected to a negative-bias DC power supply to ignite and maintain the plasma. Under these conditions, the carbon on the anode could be vaporized at the reaction temperature of 3727 °C, forming CQDs on the cathode. The CQDs surface was functionalized with hydrophilic carboxyl groups after decomposing from bulk SWCNTs and could emit various fluorescence such as blue-green, yellow, and orange color under the 365 nm light irradiation. However, CQDs produced by the arc discharge method were not easy to be purified due to the complex impurities on the surface of CQDs [8].

3.2. Bottom-up

Bottom-up processes such as hydrothermal [67,68], microwave [11], pyrolysis [69], and solvothermal [41] processes are the primary methods to prepare CQDs directly from carbon-rich precursors. Based on these methods, CQDs can be obtained from small molecules or polymer precursors in a relatively mild environment. For example, Jiang et al. prepared a large quantity of CQDs via a microwave method within a few minutes [11,70]. In this experiment, the precursors of ethanolamine and phosphoric acid experienced microwave pyrolysis, dialysis and freeze-drying (Fig. 3a). Although some weak blue FL could be emitted from the pale and yellow CQDs powder under UV (365 nm) light irradiation (Fig. 3b), most of the obtained CQDs showed remarkably long afterglow lifetime between 1.4 and 10 s (Fig. 3c). It was revealed that the observed ultralong phosphorescence of CQDs was mainly caused by the amorphous polymer-like structure of CQDs, surface heteroatom (N

and P) dopants, and intraparticle bonds. These CQDs can be employed as a potential security ink for advanced anti-counterfeiting techniques [11]. In addition, Song [71] designed an easy and low-cost microwave method to prepare CQDs within 4–5 min using urea and citric acid as the precursors. The reactants gradually transformed from a transparent solution to a dark-brown clustered precipitate under the microwave. The obtained CQDs had an average size between 1 and 5 nm and exhibited a maximum quantum yield of up to 17% with great stability. Toxic tests verified that these CQDs demonstrated zero or low toxicity. Considering the advantages of low cost, low toxicity, unique photoluminescence properties and excellent biocompatibility, CQDs showed the potential for upscale fabrication and can be used as biocompatible fluorescent ink for versatile applications.

Hydrothermal methods have been extensively used in the preparation of CQDs. N-CQDs with single state fluorescence were prepared via a hydrothermal method, generating plenty of surface poly(vinyl alcohol) (PVA) chains. The chains can isolate the graphitized cores from π–π interactions and prevent the CQDs from aggregation. These N-CQDs showed an apparent fluorescence redshift in the solution state [72]. Zhu et al. also achieved a high quantum yield of polymer-like CQDs through a hydrothermal method by condensing and carbonizing a mixture of citric acid and ethylenediamine [37]. These CQDs were used as inks for printing and demonstrated strong fluorescence under UV light at a concentration of 1×10^3 mg/mL (Fig. 3d).

Pyrolysis is another green strategy for fabrication of CQDs. Krysmann et al. [73] synthesized CQDs by citric acid and ethanolamine at various pyrolysis conditions. The precursor ratio and pyrolysis temperature significantly impacted the photoluminescence properties of the derived CQDs. At the molar ratio of 1:3, the as-synthesized CQDs could exhibit an intense photoluminescence spectrum, mainly stemmed from amide-containing fluorophores. At higher temperatures, carbonate nuclei would be produced, resulting in the exclusive PL property of CQDs. Optimal pyrolysis conditions will secure CQDs with an intense PL spectrum (Fig. 3e) [37].

Interestingly, Wang et al. used chicken eggs as the precursor to synthesize stable CQDs by plasma-induced pyrolysis [74]. The derived CQDs presented high solubility in an extensive range of organic solvents and aqueous solution and can be applied for inkjet, silk-screen printing, and optoelectronic fields due to their fluorescent and acid resistance properties. In addition, Yuan developed CQDs with a multi-color fluorescent property by using solvothermal synthesis and selecting the citric acid (CA) and diaminonaphthalene (DAN) as the precursors [41]. The straightforward method could control the fusion and carbonization of precursors. Derived CQDs with an amino-substituted structure (Fig. 3f) could be attained with a quantum yield of up to 75%, and the fluorescence color could vary from blue to red. When doped with nitrogen, this type of CQDs demonstrated highly passivated surface and a high degree of crystallinity and can be applied in monochrome electroluminescent LEDs as they render the emission colors of voltage-independent LEDs from blue to red. Also, multicolor bandgap fluorescent CQDs (MCBF-CQDs) were regarded as an active emission layer without a hole transport layer (Fig. 3g).

Long et al. employed a solvothermal method to fabricate fluorine and nitrogen co-doped CQDs (FN-CQDs) where glucose and $(C_2H_5)_3N{\bullet}3HF$ were used as the starting materials [75]. The fluorine and nitrogen co-doping (FN-CQDs) enabled CQDs to maintain room-temperature phosphorescence (RTP), derived by the $n = \pi^*$ transiting electron of C-N or C═N bonds. The quenching of RTP could be then induced by oxygen and brace triplet excitons at room temperature due to the interdot/intradot and steric protection of hydrogen bonds and C-F bonds, respectively. Additionally, MCBF-CQDs demonstrated high solubility and strong blue fluorescence in the solution. FN-CQDs in the solid-state also performed room-temperature green phosphorescence without any treatment. This study offers a new approach to developing CQDs with RTP property.

Overall, top-down methods mainly decompose the large carbon materials into nanoparticles. It was suited to a range of raw materials under a simple operation. These products generally involved (CQDs) or graphene quantum dots (GQDs). The generated CQDs partially retain the similar structure as pristine materials and some functional groups attached on the surface as well. The lattice structure of CQDs can be easily observed through the top-down ways. But it has a relative low yield of CQDs and does not have uniform particle size. In addition, the CQDs generated by the bottom up are mostly come from small molecules or polymer precursors via dehydration and carbonization. The obtained CQDs will form a polymer structure on the surface due to the incomplete carbonization. Comparison of top-down approach, the bottom up method is relatively simple to control the size and shape. It is possible to dope heteroatom on the surface. The bottom-up processes are versatile and featured by large-scale production, low cost, and eco-friendliness, which pave the way to realizing the upscale manufacture of functional CQDs with appealing properties. As increasing the degree of carbonization, it will result in the reduction of polymer structure and luminous intensity, but greatly improve the degree of graphitization and conductivity.

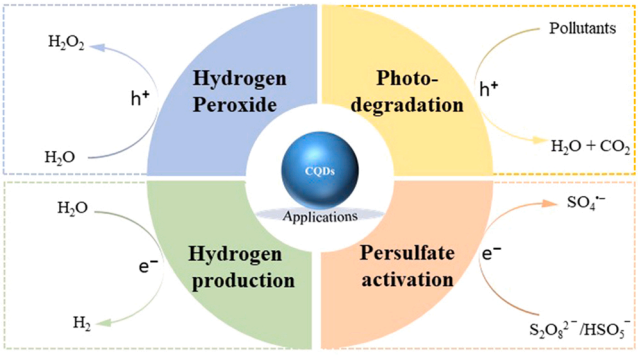

Scheme 2. Photocatalytic applications of CQDs and corresponding mechanisms.

4. Applications of CQDs in (photo)catalysis

This part will outline the applications of CQDs in photocatalytic hydrogen and hydrogen peroxide production and advanced oxidation processes for water purification. Scheme 2 showcases these applications and mechanisms.

4.1. Hydrogen production

Recently, various catalysts and manners have been utilized to produce hydrogen [76–79]. Photocatalysis is a sustainable and promising approach for the production of clean energy and fuels. Solar and water are abundant resources on the Earth, but visible light, accounting for 43% of the solar spectrum, is still poorly utilized. Conventional metal-based quantum dots have low light-absorbing and quantum efficiencies, inferior transfer efficiency, and secondary pollution. In contrast, organic CQDs show unique merits in addressing these issues. CQDs are featured in up and down photoluminescence, low toxicity, and dual capability to accept or donate electrons. These merits allow them to harvest solar energy in visible and near-infrared (NIR) zones. CQDs as active catalysts have been widely used in the photochemical generation of hydrogen by water splitting. Under light irradiation, CQDs produce photo-excited electron-hole pairs on their surface, and the separated electrons can reduce H_2O or protons into H_2 via a two-electron-transfer process.

The activity of hydrogen generation is greatly relying on the inherent character of photocatalysts, in particular the conductivity, band structure, light absorption, charge separation and transfer efficiencies. CQDs can perform exceptional photoluminescence and tuneable optical

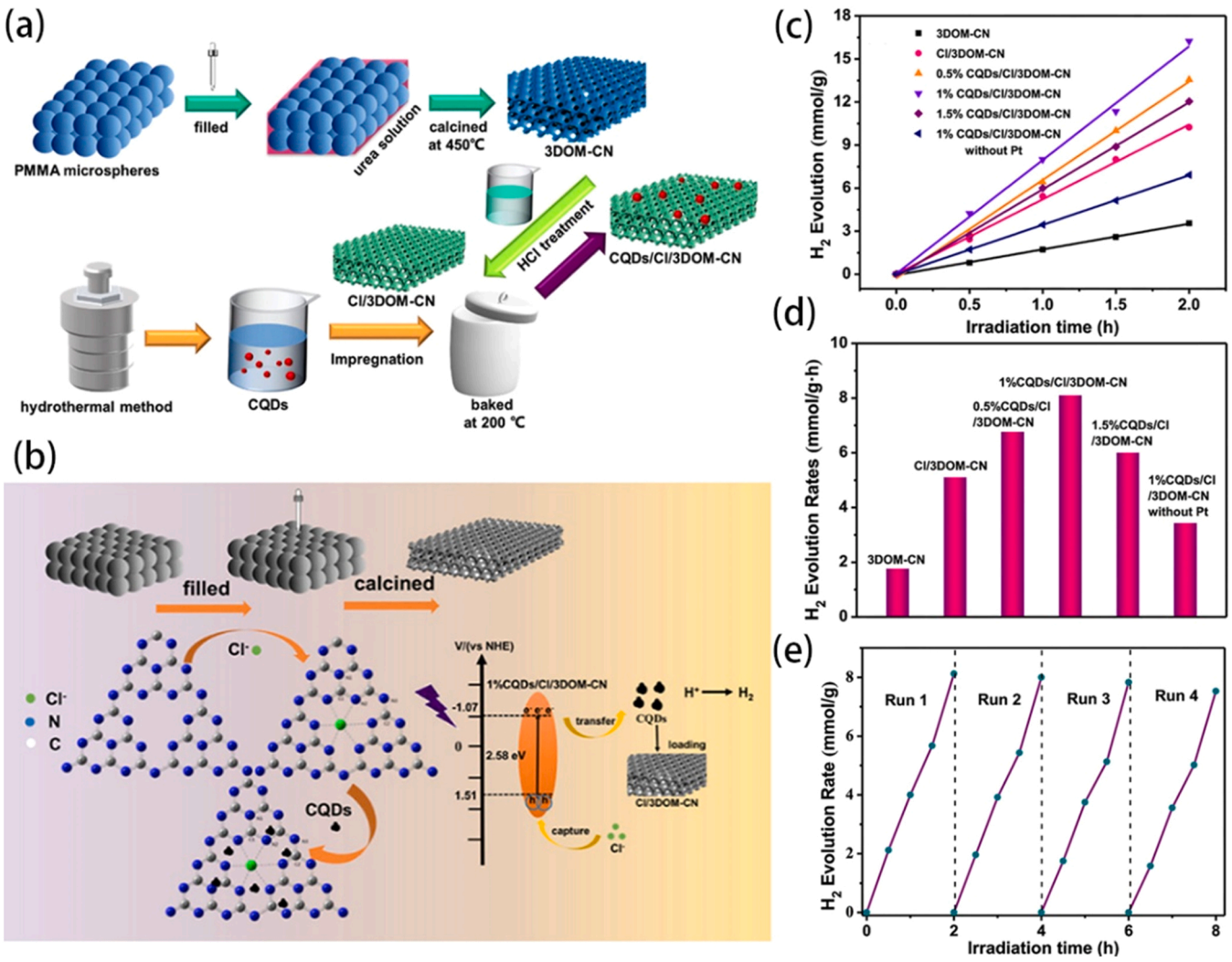

Fig. 4. (a) Fabrication of CQDs/Cl/3DOM-CN; (b) the charge transport mechanism of 1% CQDs/Cl/3DOM-CN and photoexcited electron-hole separation; (c) and (d) Photocatalytic hydrogen evolution efficiencies of 1%CQDs/Cl/3DOM-CN; 3DOM-CN without Pt; 0.5%CQDs/Cl/3DOM-CN; 1%CQDs/Cl/3DOMCN; 1.5%CQDs/Cl/3DOM-CNCl/3DOM-CN; (e) recycle experiment of 1%CQDs/Cl/3DOM-CN composites for the hydrogen evolution [48]. Copyright 2020, American Chemical Society.

properties based on the optimal surface modification. Also, the photo-excited CQDs demonstrated enhanced charge separation as the electron-hole recombination in the bulk and surface was suppressed. CQDs generally work as versatile components in photocatalytic water splitting, such as sole- or co-photocatalyst, electron mediators [7], and photo-sensitizer [80]. More importantly, the multiple effects may occur concurrently in CQDs-assisted photocatalytic systems. For instance, Dong and co-workers prepared ternary components of Ni_4P_2/CQDs/CdS for generation of hydrogen via water splitting by visible light at $\lambda = 420$ nm [26]. The transition of electron was verified from CdS to CQDs, and then to Ni_4P_2. CQDs worked as electron acceptors and donors under light irradiation, which reduced the recombination of charge carriers within the composites and hindered photo-corrosion. The transferred electrons accumulated on the surface of Ni_4P_2 to reduce H_2O or protons (H^+) into H_2 and the evolution rate of hydrogen achieved up to 145 μmol g_{cat}^{-1} h^{-1}. A simultaneous generation of H_2 and H_2O_2 was realized. Benjamin et al. used CQDs as a primary photosensitizer and combined with a Ni molecular catalyst to produce hydrogen [81]. Other studies also reported the incorporation of metal nanoparticles or single metal atoms in CQDs for improved hydrogen generation [81–85]. The doped metal nanoparticles can enhance light absorption via surface plasmon resonance (SPR) effects.

CQDs can also be employed as an electron reservoir for trapping photogenerated electrons and inhibiting the recombination of electron-hole pairs. CQDs can be coupled with plasmonic metal nanoparticles such as Cu [85], Ni [81] and Ag [83] to utilize their surface plasmon resonance (SPR) effects for photocatalysis. For instance, Zhang et al. designed a Cu/CQDs catalyst using lactic acid and copper acetate as the precursors [85]. Cu NPs exhibited an excellent absorption in the near-infrared region and could be excited under the irradiation within the wavelength range of 700–900 nm to form resonant photon-induced electrons. CQDs acted as the electron reservoir to trap these electrons, improving the photocatalytic ability and leading to a high rate of hydrogen evolution using lactic acid as a sacrificial agent.

In addition, to minimize the secondary pollution, CQDs-based metal-free hybrids were applied in photocatalysis. For example, Liu et al. synthesized a three-dimensional-ordered macro-porous carbon nitride (CN) composite of CQDs/Cl/3DOM-CN as a photocatalyst [48]. The synthesis steps are demonstrated in Fig. 4a. The chloride doping and CQDs modification on carbon nitride were achieved via a colloidal template crystal method. Though the 3D structures of CN are beneficial for light absorption and mass transfer, the photocatalytic activity of 3DOM-CN was limited by the fast recombination of charge carriers. This work revealed that CQDs could accelerate photoelectron migration and act as a photosensitizer for better light absorbance. The intercalation of Cl^- facilitated charge separation by capturing holes at the catalyst

Table 1
Representative CQDs based photocatalysis for hydrogen evolution.

Photocatalyst	Roles of CQDs	Light Source	H_2 generating rate	Ref.
CQDs/TiO_2	electron reservoir photosensitiser	UV–visible light ($\lambda > 450$ nm)	9.1 μmol h^{-1}	[80]
r-CQDs/Ni	photosensitiser	Visible light ($\lambda > 455$ nm)	398 μmol h^{-1}	[81]
Ag/CQDs/g-C_3N_4	electron reservoir	Visible light	626.93 μmol g^{-1} h^{-1}	[83]
Cu NPs/CQDs	electron reservoir	Visible light	64 μmol h^{-1}	[85]
g-C_3N_4/CQDs	–	Sunlight	3538.3 μmol g^{-1} h^{-1}	[87]
N-CQDs-P-dots	electron reservoir	Visible light	1075 μmol g^{-1} h^{-1}	[67]
x-CQDs/3DOM/Cl/CN	photosensitiser	Visible light	8120 μmol g^{-1} h^{-1}	[48]

surface, further enhancing the photocatalytic performance. Fig. 4b shows the mechanism of electron-hole separation and transfer in 1% CQDs/Cl/3DOM-CN under visible-light irradiation. Fig. 4c-d compared the amount of hydrogen evolved by 3DOM-CN and modified catalysts. Only 3.56 mmol/g of H_2 was produced from 3DOM-CN within 2 h, while Cl/3DOM-CN and 1% CQDs/Cl/3DOM-CN produced 10.24 and 16.24 mmol/g, respectively. Fig. 4e demonstrated the remarkable stability of 1%CQDs/Cl/3DOM-CN after 4 runs.

CQDs implanted graphitic carbon-nitride nanotube exhibited a higher activity in hydrogen generation than the individual components. CQDs facilitated photoelectron transport and simultaneously suppressed charge carriers' recombination. Embedding CQDs in g-C_3N_4 could optimize the electronic structure of the composite and reduce the barriers for charge transfer [27,48]. The presence of CQDs reduced the bandgap of the composite and expanded its light absorption in the visible light region [80,86]. Therefore, the CQDs can not only combine with the metal or metal oxide to generate hydrogen, but also form a composite catalyst with metal-free materials to boost hydrogen production (Table 1).

4.2. Peroxide hydrogen production

Hydrogen peroxide has been widely used in various fields of water purification, biomedicine, and chemical production [88,89]. Anthraquinone oxidation is the industrial process for production of hydrogen peroxide via direct transformation of H_2 and O_2 [90]. However, this manufacturing method is an energy-intensive process and involves toxic materials to drive H_2O_2 production [91]. Alternatively, many new techniques have been developed to generate H_2O_2, such as electrochemical catalysis [91,92], photocatalysis [90,93,94], and photo-electrocatalysis [95]. H_2O_2 can be generated by photocatalysis via two pathways. H_2O can be simultaneously oxidized into H_2O_2 and O_2 by photogenerated holes. Meanwhile, the dissolved O_2 can accept two photoelectrons to form H_2O_2 [93]. In recent years, various semiconductor catalysts including metal- [83], nonmetal- [93], and composite-based materials [2] have been developed for photocatalytic H_2O_2 production. However, most of these studies involve the utilization of sacrificial reagents. It is a challenge to exploit a new photocatalytic system without scarification reagents for H_2O_2 production.

CQDs have demonstrated an excellent solar spectrum utilization, abundant catalytic active site, and superior electron accepting/donating capacity [26,94]. As a result, CQDs are an ideal candidate cocatalyst to combine with semiconductors to produce H_2O_2 [89,92,96]. For instance, Dong et al. constructed a Ni_4P_2-CQDs/Cd hybrid where CQDs acted as both an electron donor and acceptor and Cd acted as the light harvester [26]. Then the composites combined with a Ni-containing polyoxometalate (PM) catalyst can split water to generate hydrogen

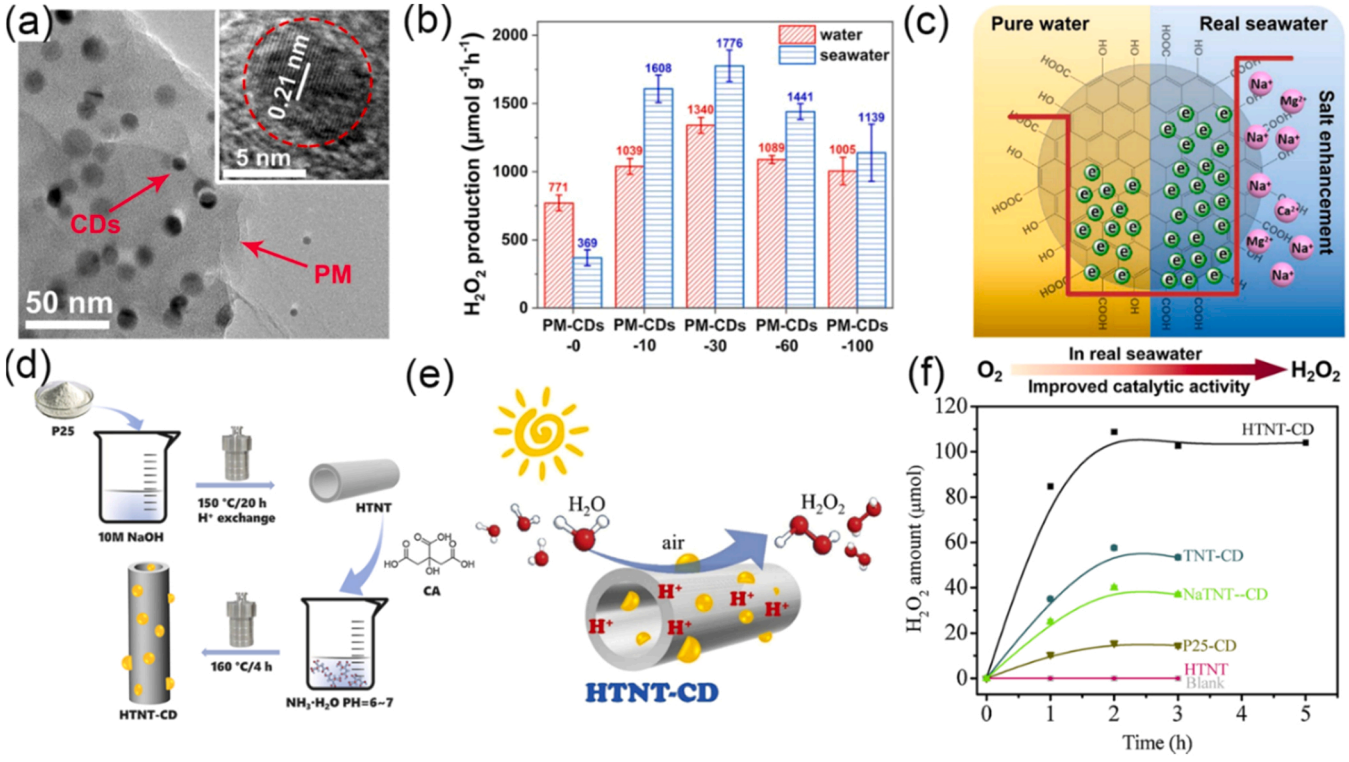

Fig. 5. (a) TEM image of PM-CDs-30 and HRTEM image (inset). (b) Comparison of H_2O_2 production among various loading CDs dose photocatalysts with different CDs contents in pure water and seawater, respectively. (c) Schematic mechanism of PM-CDs-30 photocatalytic reaction to produce H_2O_2 in seawater [94]. Copyright, 2021 Springer Nature. (d) Synthesis procedures of HTNT-CD. (e) Formation of H_2O_2 by using HTNT-CD under visible light. (f) The amount of H_2O_2 over various CD catalysts under UV illumination ($\lambda > 365$ nm) [96]. Copyright, 2018 Elsevier.

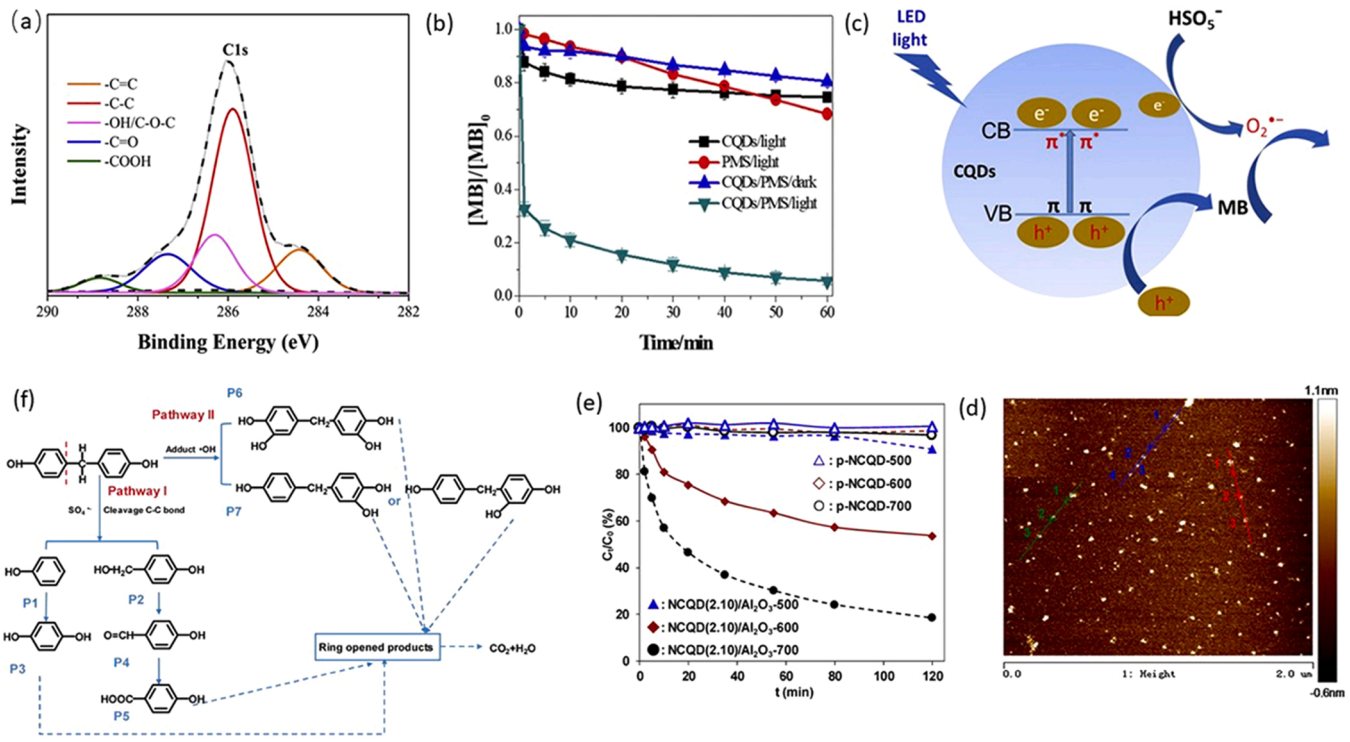

Fig. 6. (a) High-resolution XPS of C1s of CQDs. (b) The degradation of TC-HCl varied with time, with and without CQDs at LED lights irradiating. (c) Proposed mechanism for MB degradation via CQDs/PMS process [107]. Copyright, 2020 Elsevier. (d) The loading amounts of NCQDs over NCQD (x)/ Al_2O_3-700 by activating PDS for BPF degradation. AFM of NCQDs and (e) the influence of synthesis temperature of catalyst on the degradation of BPF over p-NCQD-y and NCQD (2.10)/ Al_2O_3-y. Reaction conditions: 1 mM PDS, 0.1 mM BPF, 0.25 g L^{-1} catalyst, 25 °C, and pH 6.4. (f) Proposed degradation pathways of BPF in NCQD (2.10) /Al_2O_3-700/PDS system [98]. Copyright, 2018 Elsevier.

and hydrogen peroxide under visible light irradiation without any external sacrificial reagent. During this reaction, electrons moved from Cd to CQDs and then transferred to Ni_4P_2. These photoinduced electrons would accumulate on Ni_4P_2 and reduce H_2O to generate H_2. Also, holes from Cd transferred to the surface of CQDs to oxidize H_2O into H_2O_2.

Wu et al. fabricated an organic photocatalyst (PM-CDs) to generate H_2O_2 from seawater [94]. The PM-CDs-x (x represents the loading of CDs) photocatalysts were metal-free, composed of carbon dots, 4-methoxy benzaldehyde, and organic dye molecule procyanidins, synthesized by a phenolic condensation method. It was shown that the synthetic CDs had an average size of 6–16 nm, which was uniformly distributed in the lamellar layer of the PM-CDs-30 polymer (Fig. 5a). PM-CDs-30 can effectively utilize visible light to produce electron-hole pairs. The photogenerated electrons were transferred to CDs, while the holes remained on the surface of the polymer. The electrons on the CDs surface reduced the dissolved oxygen to form hydrogen peroxide. Furthermore, the holes on the polymer surface would oxidize water to oxygen. All these reactions occurred simultaneously as two parallel reactions. In Fig. 5b, PM-CDs-30 showed the best activity in both seawater and pure water compared with other catalysts, and the production rates of H_2O_2 reached 1776 and 1340 μmol g^{-1} h^{-1} in seawater and pure water ($\lambda \geq 420$ nm; 34.8 g_{cat}^{-1} mW cm^{-2}), respectively. As shown in Fig. 5c, some functional groups were ionized at the external surface of CDs because of the cations in seawater, which would act as electron sinks on CDs. Thus, CDs can restrain electrons on their surface, prolonging the lifetime of separated electrons and holes.

CDs can be combined with inorganic metal oxides for H_2O_2 production. Ma et al. developed an effective photocatalyst containing TiO_2 nanotube and carbon dot (HTNT-CD) for visible-light-driven H_2O_2 evolution [96]. The synthesis procedures are shown in Fig. 5d. The loading of CDs was up to 2.6 wt%. Fig. 5f presents the dependence of H_2O_2 production along with time over different CD-catalysts. The HTNT-CD catalyst produced 95.3 μmol of H_2O_2 under visible light irradiating ($\lambda > 420$ nm) for 3 h. Notably, the acidic protons on the catalyst surface could dramatically speed up the generation of H_2O_2 and effectively reduce its decomposition. As a result, the H_2O_2 production rate of HTNT-CD (4.24 mmol g_{cat}^{-1} h^{-1}) was 4.9 times as high as that of commercial P25.

4.3. Coupling CQDs with persulfate oxidation

Advanced oxidation processes (AOPs) are appealing in water remediation due to their high efficiency, wide pH range tolerance, and deep mineralization by reactive oxygen species (ROS). A variety of ROS can be produced by activating oxidants such as persulfates, ozone, and hydrogen peroxide and used to degrade organic pollutants [97]. In particular, AOPs, which generate sulfate radicals (SR) from the activation of peroxydisulfate (PDS, $S_2O_8^{2-}$) and peroxymonosulfate (PMS, HSO_5^-) show a high oxidation capacity and can completely degrade contaminants into CO_2 and H_2O [98]. Many driven forces (e.g., thermal, alkaline, ultraviolet light, ultrasound) and catalysts (e.g., transition metals, graphene) have been applied to activate persulfates to produce $SO_4^{\bullet-}$ and hydroxyl radical (•OH) [99]. Carbonaceous materials are emerging green catalysts for PDS and PMS activation, attributing to their large surface areas, versatile functionality, low cost, low toxicity, no secondary contamination, good tolerance, and a wide applicable pH range [100]. A diversity of carbonaceous materials such as graphene [101], nanodiamonds [102], carbon nanotube [103], and graphene oxide [104] have been successfully applied for persulfate activation. Defects, oxygen groups, and heteroatoms on these carbonaceous materials are potential active sites for persulfate activation [105,106].

CQDs bear all the merits of carbons and are featured with quantum-size effects and photo-responsive properties. CQDs were also applied to SR-AOPs and showed significant efficiency for persulfates activation. For instance, Han et al. used a CQDs/PMS system to improve the degradation efficiency of methylene blue (MB) under LED light

Table 2
Summary of CQDs-based photocatalysts for the degradation of organic dyes, pharmaceuticals, and gaseous organic compounds.

Photocatalyst	Light source	Contaminants	Dominated ROS	Ref.
Ag/CQDs/g-C_3N_4	LED lights	Naproxen	$^1O_2/O_2^{\bullet-}$	[14]
CQDs/g-C_3N_4	300 W Xenon ($\lambda > 400$ nm)	Diclofenac	$O_2^{\bullet-}$	[16]
MoO_3CQDs/g-C_3N_4	350 W Xenon lamp ($\lambda = 420$ nm)	Tetracycline	$O_2^{\bullet-}$	[111]
CQDs/$BiPO_4$	Visible light 350 W Xenon	Indomethacin	$O_2^{\bullet-}$/•OH	[112]
N-CQDs/TiO_2	UV–visible	Methylene Blue	$O_2^{\bullet-}$/•OH	[108]
Sized-CQDs	Xenon light source (310 W)	Rhodamine B (RhB) and MB	$O_2^{\bullet-}/h^+$	[1]
CQDs/Bi_3WO_6	500 W Xenon lamp $\lambda > 400$ nm	Gaseous volatile Acetone toluene Gas (VOCs)	$O_2^{\bullet-}$	[15]
Au/CQDs	A 450-W Xenon lamp	Cyclohexane	•OH	[109]

irradiation [107]. The XPS analysis in Fig. 6a indicated that functional groups were formed on CQDs, and that the peaks of different carbon species at 284.4, 285.9, 286.3, 287.3, and 288.8 eV represent sp^2 (C═C), sp^3 (C—C), —OH/C–O—C, C═O and —COOH, respectively. CQDs had high water solubility due to surface functionalization. PMS was activated by photo-generated electrons on the surface of CQDs to form reactive $O_2^{\bullet-}$. Fig. 6b shows that the degradation efficiency of MB under visible light irradiation reached at 25.4% and 31.7% in the CQDs and PMS systems, respectively. When PMS and CQDs were co-added into the reaction system, under light irradiation, the holes and electrons were firstly produced on the excited CQD. The generated electrons reacted with PMS to form hydrogen superoxide radicals ($HO_2^{\bullet}$) and a sulfate ion. Finally, $HO_2^{\bullet}$ transformed into H^+ and $O_2^{\bullet-}$ to attack MB. The generated oxidative holes on CQDs also attacked MB, which suppressed the recombination of the charge carriers (Fig. 6c).

Additionally, CQDs@metal oxide composites have been designed to promote persulfate activation efficiency towards degradation of organic pollutants in water. For instance, Hou et al. integrated nitrogen-doped CQDs (NCQDs) with metal oxides (i.e., γ-Al_2O_3, SiO_2, and $CeZrO_2$) as a composite catalyst for PDS activation [98]. NCQDs had strong electrostatic interactions with Al_2O_3 and $CeZrO_2$, resulting in high dispersion on their surface. However, the repulsive interactions generated by NCQDs and SiO_2 support caused the aggregation of N-CQDs on SiO_2 surface. Al_2O_3/N-CQDs could activate PDS efficiently and showed the highest catalytic performance for bisphenol-F (BPF) degradation. This is due to the superior dispersion of Al_2O_3/N-CQDs and the stronger adsorption capacity of BPF on the catalyst. As shown in Fig. 6d, the sizes of NCQDs were below 3 nm. Thus, NCQDs were mainly consisted of single to multi-layers of graphitic carbons. Fig. 6e exhibits the effects of various calcination temperatures activated on the p-NCQD-y (p: the loading of the NCQD, y: calcination temperature) and NCQDs (2.10)/Al_2O_3 (2.10 means the loading amount of CQDs is 2.10%). The catalytic activities of NCQDs ((2.10)/Al_2O_3-y) increased with the elevated calcination temperature. BPF removal efficiency was 9.4%, 46.3%, and 81.5% over NCQDs (2.10)/Al_2O_3-500, NCQDs (2.10)/Al_2O_3-600 and NCQDs (2.10)/Al_2O_3-700, respectively. Fig. 6f shows the degradation pathways starting with the attack of $SO_4^{\bullet-}$ to break the Ce-C bond, resulting in the generation of intermediates of P1 and P2. Then, the produced intermediate P1 would be hydroxylated to P3, while P2 was oxidized into P4 and P5. Another degradation way was initiated by the BPF hydroxylation after adducting •OH, producing P6 and P7. Finally, all intermediates and BPF were transferred to CO_2 and H_2O in the NCQD(2.10)/Al_2O_3-700/PDS system [98].

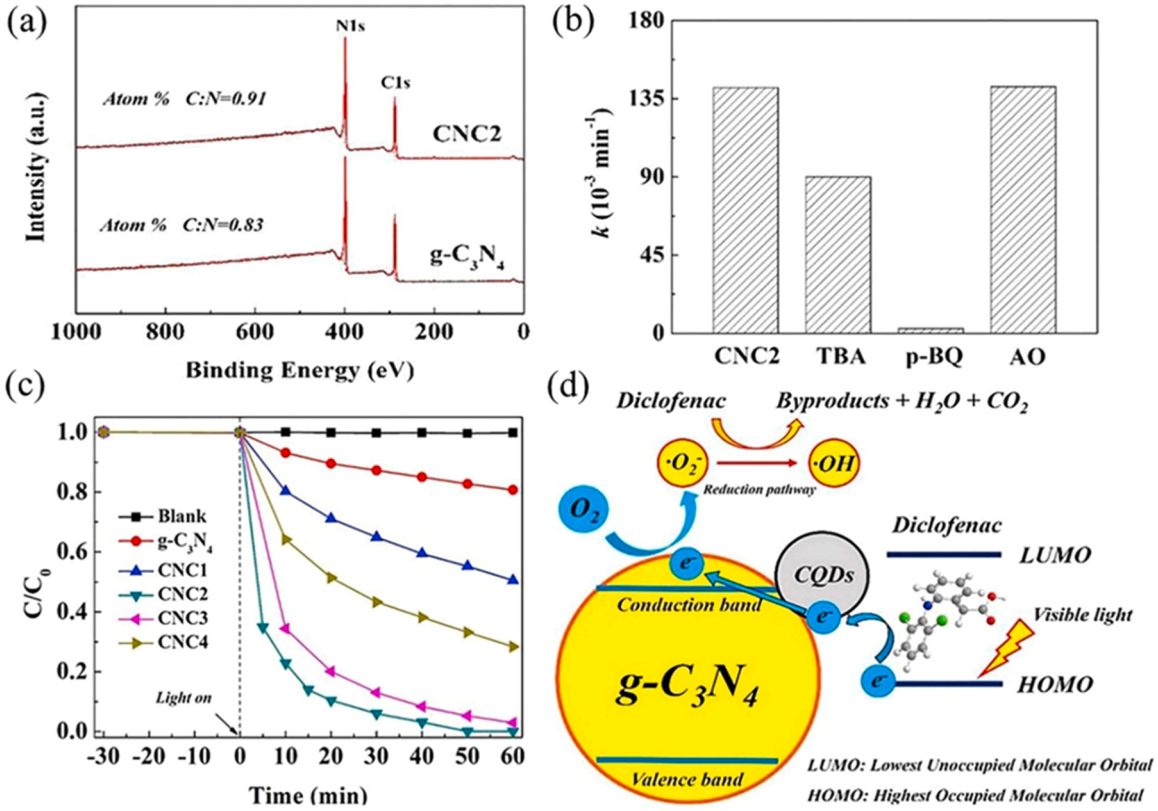

Fig. 7. The mechanism of diclofenac degradation over CQDs/g-C_3N_4. (a) XPS Survey of spectra g-C_3N_4 and CNC2; (b) Degradation kinetics of DCF under diverse scavengers effects (100 mM TBA, 50 mM p-BQ, 1 mM AO) on the degradation kinetics of DCF; (c) Degradation kinetics of DCF over different photocatalysts; (d) Schematic illustration of the photocatalytic degradation of DCF [16]. Copyright, 2018 Elsevier.

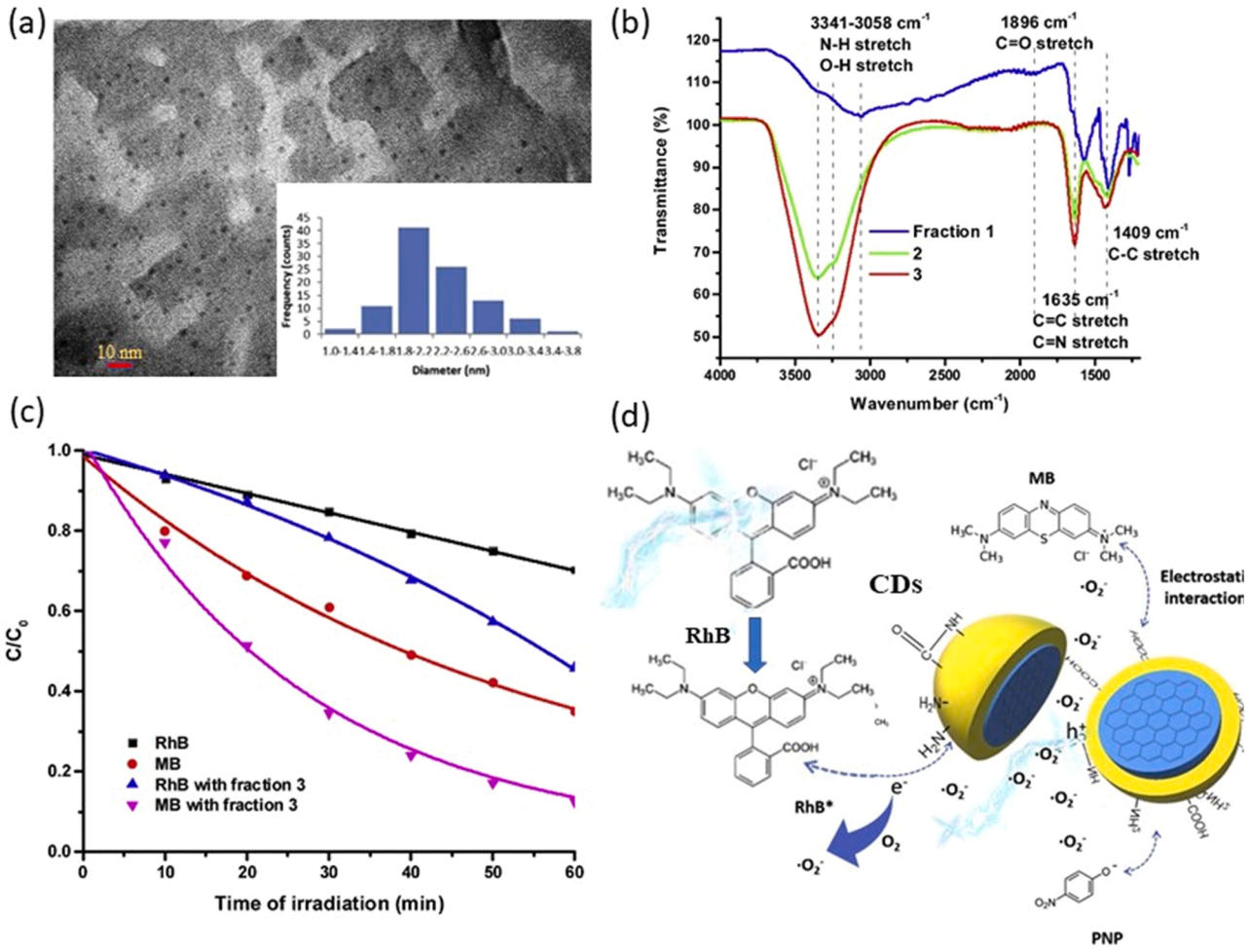

Fig. 8. (a) Modified Schematic diagram of the interactive mechanism between dyes and CQDs in photocatalytic degradation (fraction 3 represents the CQDs with the average size of 2 nm) [1]; (b) The FTIR spectra of fraction 1, 2 and 3 in a solid state. (c) Photocatalytic degradation of MB and RhB along with illuminating time; (d) Schematic diagram of the interaction between dyes and CQDs [1]. Copyright, 2019 Elsevier.

4.4. Photocatalytic degradation of pollutants

To date, photodegradation of pollutants has received growing research interest in removing different chemicals such as pharmaceuticals and volatile organic compounds. CQDs have the unique photoluminescence characteristics and superior up-conversion capability, showing a good potential for environmental remediation applications [14,16,108]. In addition, CQDs can also be used as a cocatalyst to regulate the band structure and active site of common photocatalysts. Various metals, metal oxides, and non-metal materials have been used to hybridize with CQDs for photocatalytic degradation of pollutants in the aqueous environment under light irradiation [109,110]. This section will demonstrate the degradation of organic contaminants (such as pharmaceuticals) and toxic gases using CQDs. Some representative studies on photodegradation using CQDs are listed in Table 2.

CQDs-loaded g-C_3N_4 has been extensively used as a photocatalyst to degrade pharmaceuticals. For instance, Liu et al. successfully prepared CQDs/g-C_3N_4 (CNCs, s represents number 1–4, indicated CQDs solution of 10, 50, 100, 150 μL, respectively) photocatalysts via a facile thermal polymeric approach for purifying diclofenac (DCF) in water [16]. The XPS spectra indicated that the value of atomic ratio between C and N was 0.83 for g-C_3N_4, while the CNC2 increased to 0.91, which further proved the CQDs was incorporated into g-C_3N_4 (Fig. 7a). CQDs/g-C_3N_4 demonstrated an excellent performance for photocatalytic oxidation of DCF, and the reaction rate was nearly 15 times higher than g-C_3N_4 (Fig. 7c) at visible light. The adsorption-desorption equilibrium was achieved between DCF and photocatalysts within 30 min in dark conditions, and DCF cannot be degraded by photolysis without the photocatalyst. According to the quenching experiments (Fig. 7b), DCF was primarily oxidized by $O_2^{\bullet-}$ while •OH played a minor role. Visible light would excite CQDs to generate photoinduced electrons, which would then transfer to the conduction band (CB) of g-C_3N_4. The excited electrons at the CB of g-C_3N_4 would reduce dissolved oxygen to $O_2^{\bullet-}$ through a photosensitive process, and a little amount of $O_2^{\bullet-}$ can be converted to •OH through water oxidation (Fig. 7d).

Wang's group synthesized a ternary composite photocatalyst consisting of single atom silver, CQDs, and ultrathin g-C_3N_4 (SDAg-CQDs/UCN) [14]. The composite demonstrated a strong photo-response within a wide-range spectrum, collectively ascribed to the surface plasmon resonance effect of single-atom Ag as well as the prominent characteristics of CQDs. The excellent charge separation narrowed bandgap and up-converted fluorescent nature of CQDs significantly improved the photocatalytic activity of the composites. According to scavenging experiments and electron spin resonance (ESR) analysis, $^1O_2$ and $O_2^{\bullet-}$ radical account for the main role ROS for naproxen (NPX) degradation.

In recent years, CQDs have been also used as a catalyst to degrade MB [29,36,108], cyclohexane [109], RhB [1,36] under visible light irradiation. For example, Zhou et al. utilized microwave to synthesize CQDs, which acted as a photocatalyst to degrade RhB and MB [1]. CQDs were separated into three fractions with different sizes via size exclusion chromatography. The average particle size (4.48 ± 1.38, 3.61 ± 0.92 and 2.24 ± 0.45 nm) was confirmed by the TEM images (Fig. 8a). The

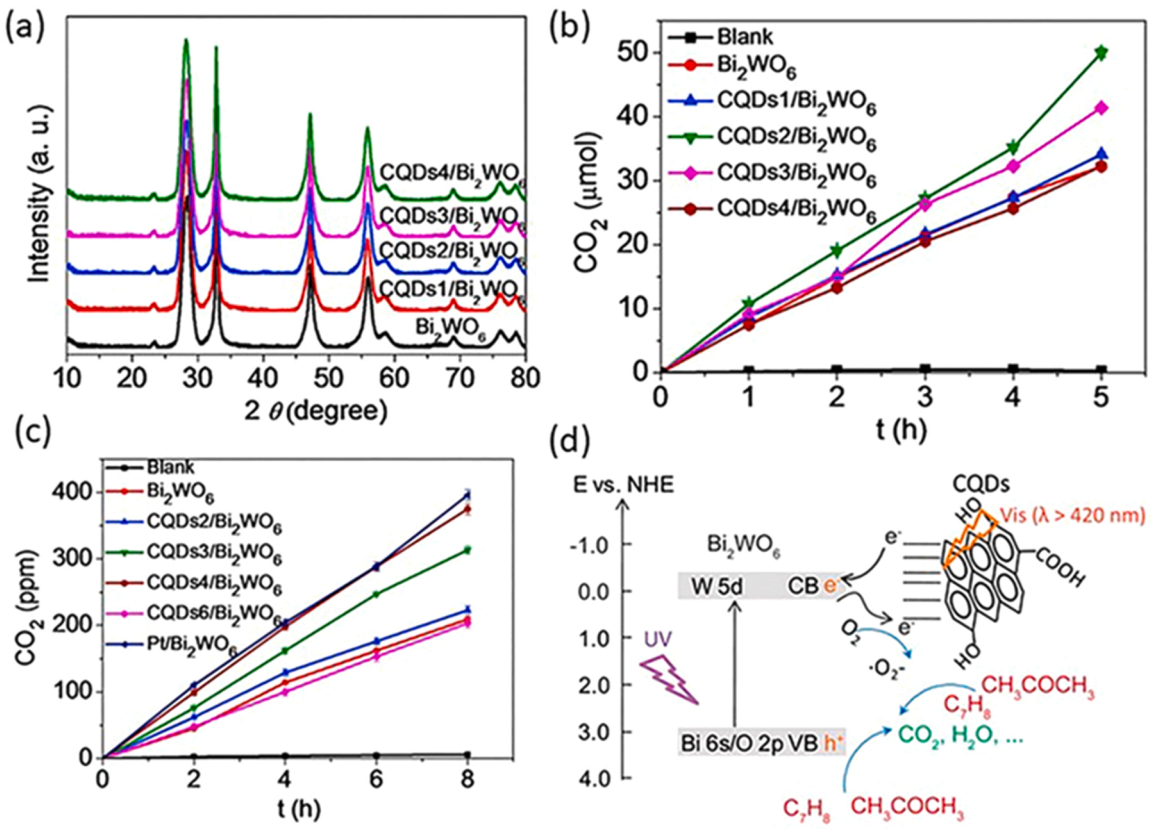

Fig. 9. (a) XRD patterns of pristine Bi_2WO_6 and CQDs/Bi_2WO_6 nanoflake aggregates. (b) CO_2 productivity for CQDs, pristine Bi_2WO_6 and CQDs decorated on the Bi_2WO_6 nanoflake with diverse loading dosages for photocatalytic oxidation of acetone at $\lambda = 420$ nm visible light illuminating. (c). CO_2 production by pristine Bi_2WO_6 and CQDs/Bi_2WO_6 at $\lambda > 420$ nm visible light irradiating. (d) The mechanism of CQDs/ Bi_2WO_6 photocatalyst for the photocatalytic oxidation of VOCs under the irradiation of UV–vis and visible light [15]. Copyright, 2016 Elsevier.

ATR-FTIR results in Fig. 8b reveals that three fractions share similar functional groups while relative contents of functional group and elemental compositions are different. Fig. 8c shows that fraction 3 (about 2 nm CDs) attained fast photocatalytic degradation of MB (60%) and RhB (20%) within 60 min. Interestingly, RhB molecules may convert into RhB* radicals by visible light excitation. Fig. 8d shows that the generated RhB* radicals could be adsorbed at the external of CDs. The electrons from CB of CDs reduced the dissolved O_2 and generated $O_2^{\bullet-}$, which promoted RhB degradation. With the presence of EDTA, the degradation rate significantly decreased, which indicated the contribution of holes to dye decolorization. Also, self-photosensitization of RhB molecules had a significant contribution to the photodegradation.

Apart from aqueous phase degradation, CQDs have been applied to remove gaseous volatile organic compounds (VOCs) via photocatalysis. For instance, Qian et al. fabricated a CQDsX/Bi_2WO_6 (X refer to the loading amount of CQDs) heterostructure to remove VOCs under UV-Vis light irradiation [15]. When the mass content of CQDs increased, the crystal structure of Bi_2WO_3 remained unchanged (Fig. 9a). The decoration of CQDs led to the redshift of the absorption band of the hybrid photocatalyst, which enhanced the photocatalytic activity. Moreover, CQDs can accept and donate electrons, which significantly accelerates the transformance of charges at the interface of Bi_2WO_6 and CQDs. Compared with Bi_2WO_6, CQDs surface-decorated Bi_2WO_6 exhibited a higher photocatalytic activity toward acetone and toluene degradation and could finally mineralize VOCs into CO_2 via gas-solid reactions (Fig. 9b). The CO_2 generation rate over CQDs/Bi_2WO_6 was 48 ppm/h, almost the same as Pt/Bi_2WO_6 (Fig. 9c). The authors proposed the photocatalytic oxidation mechanism of VOCs over CQDs/Bi_2WO_6. Aromatic rings of CQDs in the composites may enhance the capture of VOCs compared with pristine Bi_2WO_6 (Fig. 9d). Bi_2WO_6 was excited by light to generate e^-/h^+ pairs. h^+ has a strong oxidative ability upon VOCs. Besides, O_2 would capture the accumulated electrons on CQDs and convert to $O_2^{\bullet-}$.

5. Conclusions and outlook [1–113]

In summary, CQDs feature in excellent optical properties, low cost, environmental friendliness, and abundant resources, making them an ideal candidate in energy and environmental applications. At present, significant progresses have been made in developing CQDs based materials and their utilizations in environmental remediation and energy conversion. The physicochemical properties of CQDs, such as unique fluorescence, photoluminescence, and electronic modulation properties, had been preliminarily studied. Their synthetic methods are varied. CQDs also have excellent electrical conductivity and charge transport ability. Their surface could be functionally modified for engineering the active site, which would be conducive to the generation of free radicals or proton reduction. CQDs also own unique semiconductor characteristics, altering the band structure and light absorption of the CQDs-based composite. Hence, CQDs had been used as photocatalysts alone or as cocatalysts to combine with the substrate semiconductor materials for catalytic reactions, such as photocatalytic production of hydrogen and hydrogen peroxide, photodegradation, and advanced oxidation.

Nevertheless, some issues are still needed to be addressed. Firstly, the reaction mechanism, formation process, and nucleation are still unclear because of the non-standard synthesis methods. Large-scale and systematic manufacturing approaches are required to obtain high-quality CQDs. These CQDs are expected to possess desirable structure and chemistry regarding sizes, shapes, functional groups, and crystallinity. Secondly, a standard purification method of CQDs is required to achieve

high purity. Some host molecular entities are generated on the surface of CQDs in the synthesis process, interfering with their actual applications [42]. Thirdly, the role of the photoelectric properties of CQDs in catalytic reactions is not clearly illustrated. In-situ spectroscopic characterization, such as in-situ infrared and UV–vis measurements, needs to be applied to study the absorption-emission properties of CQDs in catalytic reactions. In addition, the PL mechanisms are controversial because of the various precursors and different reaction conditions. Some researchers reported that the carbon cores and fluorophores determine the PL behaviors, but no definite cognitions of the CQDs structure [113]. The structural features of CQDs should be well-identified to achieve optimal utilization in real life. Finally, the research on applying CQDs in energy and environmental areas is still at the infant stage. The reactivity of pure CQDs in the treatment of organic pollutants and the production of green fuel is still not ideal. More fundamental studies are necessary on improving the properties of CQDs and realizing the full potential of CQDs in the areas. There are still massive opportunities in CQDs synthesis, modification, mechanism, and advanced applications. We believe that controllable synthesis, large-scale production, clear structure-activity relations will significantly advance the applications of CQDs in green catalysis and sustainability.

CRediT authorship contribution statement

Yu Yao: Writing – original draft. **Huayang Zhang:** Writing – review & editing. **Kunsheng Hu:** Writing. **Gang Nie:** Formal analysis. **Yangyang Yang:** Formal analysis. **Yuxian Wang:** Writing – review & editing. **Xiaoguang Duan:** Conceptualization, Supervision, Writing – review & editing. **Shaobin Wang:** Supervision, Writing – review & editing.

Declaration of Competing Interest

The authors declare that they have no known competing financial interests or personal relationships that could have appeared to influence the work reported in this paper.

Acknowledgements

This project was partially supported by the Australian Research Council (DP190103548 and DE210100253).

References

[1] Y. Zhou, E. Zahran, B. Quiroga, J. Perez, K. Mintz, Z. Peng, P. Liyanage, R. Pandey, C. Chusuei, R. Leblanc, Size-dependent photocatalytic activity of carbon dots with surface-state determined photoluminescence, Appl. Catal. B 248 (2019) 157–166.
[2] Y. Fu, C. Zhu, C. Liu, M. Zhang, H. Wang, W. Shi, H. Huang, Y. Liu, Z. Kang, CoMn-S/CDs nanocomposite for effective long wavelength visible-light-driven photocatalytic water splitting, Appl. Catal. B 226 (2018) 295–302.
[3] P. Yang, H. Ou, Y. Fang, X. Wang, A facile steam reforming strategy to delaminate layered carbon nitride semiconductors for photoredox catalysis, Angew. Chem. Int. Ed. 56 (2017) 3992–3996.
[4] Q. Zhang, W. Wang, J. Zhang, X. Zhu, Q. Zhang, Y. Zhang, Z. Ren, S. Song, J. Wang, Z. Ying, R. Wang, X. Qiu, T. Peng, L. Fu, Highly efficient photocatalytic hydrogen evolution by ReS_2 via a two-electron catalytic reaction, Adv. Mater. 30 (2018), 1707123.
[5] Y. Wu, H. Wang, W. Tu, Y. Liu, S. Wu, Y. Tan, J. Chew, Construction of hierarchical ^2D–^2D $Zn_3In_2S_6$/fluorinated polymeric carbon nitride nanosheets photocatalyst for boosting photocatalytic degradation and hydrogen production performance, Appl. Catal. B 233 (2018) 58–69.
[6] Q. Huang, Y. Xiong, Q. Zhang, H. Yao, Z. Li, Noble metal-free MoS_2 modified $Mn_{0.25}Cd_{0.75}S$ for highly efficient visible-light driven photocatalytic H_2 evolution, Appl. Catal. B 209 (2017) 514–522.
[7] F. Li, Y. Liu, B. Mao, L. Li, H. Huang, D. Zhang, W. Dong, Z. Kang, W. Shi, Carbon-dots-mediated highly efficient hole transfer in I-III-VI quantum dots for photocatalytic hydrogen production, Appl. Catal. B 292 (2021), 120154.
[8] A. Rasal, S. Yadav, A. Yadav, A. Kashale, S. Manjunatha, A. Altaee, Jia. Chang, Carbon quantum dots for energy applications: a review, ACS Appl. Nano Mater. 4 (2021) 6515–6541.
[9] X. Du, C. Wang, G. Wu, S. Chen, The rapid and large-scale production of carbon quantum dots and their Integration with polymers, Angew. Chem. Int. Ed. 60 (2021) 8585–8595.
[10] H. Dang, L.-K. Huang, Y. Zhang, C.-F. Wang, S. Chen, Large-scale ultrasonic fabrication of white fluorescent carbon dots, Ind. Eng. Chem. Res. 55 (2016) 5335–5341.
[11] K. Jiang, Y. Wang, X. Gao, C. Cai, H. Lin, Facile, quick, and gram-scale synthesis of ultralong-lifetime room-temperature-phosphorescent carbon dots by microwave irradiation, Angew. Chem. Int. Ed. 57 (2018) 6216–6220.
[12] M. Liu, B. Chen, C. Li, C. Huang, Carbon dots: synthesis, formation mechanism, fluorescence origin and sensing applications, Green Chem. 21 (2019) 449–471.
[13] K. Jiang, S. Sun, L. Zhang, Y. Lu, A. Wu, C. Cai, H. Lin, Red, green, and blue luminescence by carbon dots: full-color emission tuning and multicolor cellular imaging, Angew. Chem. Int. Ed. 127 (2015) 5450–5453.
[14] F. Wang, Y. Wang, Y. Feng, Y. Zeng, Z. Xie, Q. Zhang, Y. Su, P. Chen, Y. Liu, K. Yao, W. Lv, G. Liu, Novel ternary photocatalyst of single atom-dispersed silver and carbon quantum dots co-loaded with ultrathin g-C_3N_4 for broad spectrum photocatalytic degradation of naproxen, Appl. Catal. B 221 (2018) 510–520.
[15] X. Qian, D. Yue, Z. Tian, M. Reng, Y. Zhu, M. Kan, T. Zhang, Y. Zhao, Carbon quantum dots decorated Bi_2WO_6 nanocomposite with enhanced photocatalytic oxidation activity for VOCs, Appl. Catal. B 193 (2016) 16–21.
[16] W. Liu, Y. Li, F. Liu, W. Jiang, D. Zhang, J. Liang, Visible-light-driven photocatalytic degradation of diclofenac by carbon quantum dots modified porous g-C_3N_4: mechanisms, degradation pathway and DFT calculation, Water Res. 151 (2019) 8–19.
[17] A. Zhu, Q. Qu, X. Shao, B. Kong, Y. Tian, Carbon-dot-based dual-emission nanohybrid produces a ratiometric fluorescent sensor for in vivo imaging of cellular copper ions, Angew. Chem. Int. Ed. 51 (2012) 7185–7189.
[18] H. Jia, Z. Wang, T. Yuan, F. Yuan, X. Li, Y. Li, Z. Tan, L. Fan, S. Yang, Electroluminescent warm white light-emitting diodes based on passivation enabled bright red bandgap emission carbon quantum dots, Adv. Sci. 6 (2019), 1900397.
[19] C. Shen, Q. Lou, C. Lv, J. Zang, S. Qu, L. Dong, C. Shan, Bright and multicolor chemiluminescent carbon nanodots for advanced information encryption, Adv. Sci. 6 (2019), 1802331.
[20] Q. Lou, S. Qu, P. Jing, W. Ji, D. Li, J. Cao, H. Zhang, L. Liu, J. Zhao, D. Shen, Water-triggered luminescent "nano-bombs" based on supra-(carbon nanodots), Adv. Mater. 27 (2015), 1315-1315.
[21] A. Hutton, B.B. Martindale, E. Reisner, Carbon dots as photosensitisers for solar-driven catalysis, Chem. Soc. Rev. 46 (2017) 6111–6123.
[22] K.A. Fernando, S. Sahu, Y. Liu, W.K. Lewis, E.A. Guliants, A. Jafariyan, P. Wang, C.E. Bunker, Y.P. Sun, Carbon quantum dots and applications in photocatalytic energy conversion, ACS Appl. Mater. Interfaces 7 (2015) 8363–8376.
[23] T. Wang, C. Nie, Z. Ao, S. Wang, T. An, Recent progress in g-C3N4 quantum dots: synthesis, properties and applications in photocatalytic degradation of organic pollutants, J. Mater. Chem. A 8 (2020) 485–502.
[24] S. Bhattacharyya, F. Ehrat, P. Urban, R. Teves, R. Wyrwich, M. Doblinger, J. Feldmann, A. Urban, J. Stolarczyk, Effect of nitrogen atom positioning on the trade-off between emissive and photocatalytic properties of carbon dots, Nat. Commun. 8 (2017) 1401.
[25] M. Han, S. Lu, F. Qi, S. Zhu, H. Sun, B. Yang, Carbon dots–implanted graphitic carbon nitride nanosheets for photocatalysis: simultaneously manipulating carrier transport in inter-and intralayers, Sol. RRL 4 (2020), 1900517.
[26] Y. Dong, Q. Han, Q. Hu, C. Xu, C. Dong, Y. Peng, Y. Ding, Y. Lan, Carbon quantum dots enriching molecular nickel polyoxometalate over CdS semiconductor for photocatalytic water splitting, Appl. Catal. B 293 (2021), 120214.
[27] Y. Wang, J. Liu, B. Han, X. Hu, F. Yang, Z. Xu, Y. Li, S. Jia, Z. Li, Y. Zhao, Carbon quantum dot implanted graphite carbon nitride nanotubes: excellent charge separation and enhanced photocatalytic hydrogen evolution, Angew. Chem. Int. Ed. 130 (2018) 5867–5873.
[28] K. Wang, R. Jiang, T. Peng, X. Chen, W. Dai, X. Fu, Modeling the effect of Cu doped TiO_2 with carbon dots on CO_2 methanation by H_2O in a photo-thermal system, Appl. Catal. B 256 (2019), 117780.
[29] R. Miao, Z. Luo, W. Zhong, S.-Y. Chen, T. Jiang, B. Dutta, Y. Nasr, Y. Zhang, S. L. Suib, Mesoporous TiO_2 modified with carbon quantum dots as a high-performance visible light photocatalyst, Appl. Catal. B 189 (2016) 26–38.
[30] M. Li, M. Wang, L. Zhu, Y. Li, Z. Yan, Z. Shen, X. Cao, Facile microwave assisted synthesis of N-rich carbon quantum dots/dual-phase TiO_2 heterostructured nanocomposites with high activity in CO_2 photoreduction, Appl. Catal. B 231 (2018) 269–276.
[31] X. Pei, D. Xiong, H. Wang, S. Gao, X. Zhang, S. Zhang, J. Wang, Reversible phase transfer of carbon dots between an organic phase and aqueous solution triggered by CO_2, Angew. Chem. Int. Ed. 130 (2018) 3687–3691.
[32] Z. Liu, Z. Wang, S. Qing, N. Xue, S. Jia, L. Zhang, L. Li, N. Li, L. Shi, J. Chen, Improving methane selectivity of photo-induced CO_2 reduction on carbon dots through modification of nitrogen-containing groups and graphitization, Appl. Catal. B 232 (2018) 86–92.
[33] H. Zhong, R. Sa, H. Lv, S. Yang, D. Yuan, X. Wang, R. Wang, Covalent organic framework hosting metalloporphyrin-based carbon dots for visible-light-driven selective CO_2 reduction, Adv. Funct. Mater. 30 (2020), 2002654.
[34] H. Yu, R. Shi, Y. Zhao, G.I. Waterhouse, L. Wu, C. Tung, T. Zhang, Smart utilization of carbon dots in semiconductor photocatalysis, Adv. Mater. 28 (2016) 9454–9477.
[35] J. Wu, Y. Sun, C. Gu, T. Wang, Y. Xin, C. Chai, C. Cui, D. Ma, Pt supported and carbon coated Bi_2MoO_2 composite for enhanced 2,4–dibromophenol degradation

under visible–light irradiation: insight into band gap structure and photocatalytic mechanism, Appl. Catal. B 237 (2018) 622–632.
[36] X. Miao, X. Yue, Z. Ji, X. Shen, H. Zhou, M. Liu, K. Xu, J. Zhu, G. Zhu, L. Kong, S. A. Shah, Nitrogen-doped carbon dots decorated on g-C_3N_4/Ag_3PO_4 photocatalyst with improved visible light photocatalytic activity and mechanism insight, Appl. Catal. B 227 (2018) 459–469.
[37] S. Zhu, Q. Meng, L. Wang, J. Zhang, Y. Song, H. Jin, K. Zhang, H. Sun, H. Wang, B. Yang, Highly photoluminescent carbon dots for multicolor patterning, sensors, and bioimaging, Angew. Chem. Int. Ed. 52 (2013) 3953–3957.
[38] Y. Wang, A. Hu, Carbon quantum dots: synthesis, properties and applications, J. Mater. Chem. C 2 (2014) 6921.
[39] S. Qu, D. Zhou, D. Li, W. Ji, P. Jing, D. Han, L. Liu, H. Zeng, D. Shen, Toward efficient orange emissive carbon nanodots through conjugated sp^2-domain controlling and surface charges engineering, Adv. Mater. 28 (2016) 3516–3521.
[40] J. Liu, Y. Geng, D. Li, H. Yao, Z. Huo, Y. Li, K. Zhang, S. Zhu, H. Wei, W. Xu, J. Jiang, B. Yang, Deep red emissive carbonized polymer dots with unprecedented narrow full width at half maximum, Adv. Mater. 32 (2020), 1906641.
[41] F. Yuan, Z. Wang, X. Li, Y. Li, Z. Tan, L. Fan, S. Yang, Bright multicolor bandgap fluorescent carbon quantum dots for electroluminescent light-emitting diodes, Adv. Mater. 29 (2017), 1604436.
[42] J. Liu, R. Li, B. Yang, Carbon dots: a new type of carbon-based nanomaterial with wide applications, ACS Cent. Sci. 6 (2020) 2179–2195.
[43] Ru Wang, Z.T.K. Lu, Y. Xu, Recent progress in carbon quantum dots: synthesis, properties and applications in photocatalysis, J. Mater. Chem. A 5 (2017) 3717–3734.
[44] S. Lim, W. Shen, Z. Gao, Carbon quantum dots and their applications, Chem. Soc. Rev. 44 (2015) 362–381.
[45] B.Z.Y. Sun, Y. Lin, W. Wang, K. Fernando, P. Pathak, M. Meziani, B. Harruff, X. Wang, H. Wang, P. Luo, H. Yang, M. Kose, B. Chen, L. Veca, S. Xie, Quantum-sized carbon dots for bright and colorful photoluminescence, J. Am. Chem. Soc. 128 (2006) 7756–7757.
[46] V. Georgakilas, J. Perman, J.J. Tucek, R.R. Zboril, Broad family of carbon nanoallotropes: classification, chemistry, and applications of fullerenes, carbon dots, nanotubes, graphene, nanodiamonds, and combined superstructures, Chem. Rev. 115 (2015) 4744–4822.
[47] H. Tetsuka, R. Asahi, A. Nagoya, K. Okamoto, I. Tajima, R. Ohta, A. Okamoto, Optically tunable amino-functionalized graphene quantum dots, Adv. Mater. 24 (2012) 5333–5338.
[48] W. Liu, G. Liu, N. Shi, D. Liu, F. Wen, Carbon quantum dot-modified and chloride-doped ordered macroporous graphitic carbon nitride composites for hydrogen evolution, ACS Appl. Nano Mater. 3 (2020) 12188–12197.
[49] C. Hu, M. Li, P. Qiu, Y. Sun, Design and fabrication of carbon dots for energy conversion and storage, Chem. Soc. Rev. 48 (2019) 2315–2337.
[50] H. Li, X. He, Z. Kang, H. Huang, Y. Liu, J. Liu, S. Lian, C. Tsang, X. Yang, S. Lee, Water-soluble fluorescent carbon quantum dots and photocatalyst design, Angew. Chem. Int. Ed. 49 (2010) 4430–4434.
[51] E.B.R. Zhang, S. Lee, Size dependence of energy gaps in small carbon clusters the origin of broadband luminescence, Diam. Relat. Mater. 7 (1998) 1663–1668.
[52] M.M.L. Cao, S. Sahu, Y. Sun, Photoluminescence properties of graphene versus other carbon nanomaterials, Acc. Chem. Res. 46 (2012) 171–180.
[53] J. Shen, Y. Zhu, C. Chen, X. Yang, C. Li, Facile preparation and upconversion luminescence of graphene quantum dots, Chem. Commun. 47 (2011) 2580–2582.
[54] Y. Song, S. Zhu, S. Xiang, X. Zhao, J. Zhang, H. Zhang, Y. Fu, B. Yang, Investigation into the fluorescence quenching behaviors and applications of carbon dots, Nanoscale 6 (2014) 4676–4682.
[55] S. Zhu, Y. Song, X. Zhao, J. Shao, J. Zhang, B. Yang, The photoluminescence mechanism in carbon dots (graphene quantum dots, carbon nanodots, and polymer dots): Current state and future perspective, Nano Res. 8 (2015) 355–381.
[56] X.W.L. Cao, M. Meziani, F. Lu, H. Wang, P. Luo, Y. Lin, B. Harruff, L. Veca, D. Murray, S. Xie, Y. Sun, Carbon dots for multiphoton bioimaging, J. Am. Chem. Soc. 129 (2007) 11318–11319.
[57] M. Haase, H. Schafer, Upconverting nanoparticles, Angew. Chem. Int Ed. 50 (2011) 5808–5829.
[58] Z.H. Kang, C.H.A. Tsang, N.B. Wong, Z.D. Zhang, S.T. Lee, Silicon quantum dots: a general photocatalyst for reduction, decomposition, and selective oxidation reactions, J. Am. Chem. Soc. 129 (2007) 12090–12091.
[59] S. Park, H. Lee, E. Park, S. Lee, J. Lee, S. Jeong, C. Kim, Y. Lee, Y. Huh, J. Lee, Photoluminescent green carbon nanodots from food-waste-derived sources: large-scale synthesis, properties, and biomedical applications, ACS Appl. Mater. Interfaces 6 (2014) 3365–3370.
[60] H. Tao, K. Yang, Z. Ma, J. Wan, Y. Zhang, Z. Kang, Z. Liu, In vivo NIR fluorescence imaging, biodistribution, and toxicology of photoluminescent carbon dots produced from carbon nanotubes and graphite, Small 8 (2012) 281–290.
[61] R. Liu, D. Wu, S. Liu, K. Koynov, W. Knoll, Q. Li, An aqueous route to multicolor photoluminescent carbon dots using silica spheres as carriers, Angew. Chem. Int. Ed. 48 (2009) 4598–4601.
[62] H. Ming, Z. Ma, Y. Liu, K. Pan, H. Yu, F. Wang, Z. Kang, Large scale electrochemical synthesis of high quality carbon nanodots and their photocatalytic property, Dalton Trans. 41 (2012) 9526–9531.
[63] S. Tajik, Z. Dourandish, K. Zhang, H. Beitollahi, Q.V. Le, H.W. Jang, M. Shokouhimehr, Carbon and graphene quantum dots: a review on syntheses, characterization, biological and sensing applications for neurotransmitter determination, RSC Adv. 10 (2020) 15406–15429.
[64] X. Li, H. Wang, Y. Shimizu, A. Pyatenko, K. Kawaguchi, N. Koshizaki, Preparation of carbon quantum dots with tunable photoluminescence by rapid laser passivation in ordinary organic solvents, Chem. Commun. 47 (2011) 932–934.
[65] L.C.S. Yang, P. Luo, F. Lu, X. Wang, H. Wang, M. Meziani, Y. Liu, G. Qi, Y. Sun, Carbon dots for optical imaging in vivo, J. Am. Chem. Soc. 131 (2009) 11308–11309.
[66] R.R.X. Xu, Y. Gu, H. Ploehn, L. Gearheart, K. Raker, W. Scrivens, Electrophoretic analysis and purification of fluorescent single-walled carbon nanotube fragments, J. Am. Chem. Soc. 126 (2004) 12736–12737.
[67] M. Elsayed, J. Jayakumar, M. Abdellah, T. Mansoure, K. Zheng, A. Elewa, C. Chang, L. Ting, W. Lin, H. Yu, W. Wang, C. Chung, H. Chou, Visible-light-driven hydrogen evolution using nitrogen-doped carbon quantum dot-implanted polymer dots as metal-free photocatalysts, Appl. Catal. B 283 (2021), 116959.
[68] D. Bouzas-Ramos, J. Cigales Canga, J. Mayo, R. Sainz, J. Ruiz Encinar, J.J. Costa-Fernandez, Carbon quantum dots codoped with nitrogen and lanthanides for multimodal imaging, Adv. Funct. Mater. 29 (2019), 1903884.
[69] C.F. Wang, R. Cheng, W.Q. Ji, K.Z. Ma, L.T. Ling, S. Chen, Recognition of latent fingerprints and ink-free printing derived from interfacial segregation of carbon dots, ACS Appl. Mater. Interfaces 10 (2018) 39205–39213.
[70] F.L. Yuan, Y.K. Wang, G. Sharma, Y.T. Dong, X.P. Zheng, P.C. Li, A. Johnston, G. Bappi, J.Z. Fan, H. Kung, B. Chen, M.I. Saidaminov, K. Singh, O. Voznyy, O. M. Bakr, Z.H. Lu, E.H. Sargent, Bright high-colour-purity deep-blue carbon dot light-emitting diodes via efficient edge amination, Nat. Photonics 14 (2020) 171–176.
[71] S. Qu, X. Wang, Q. Lu, X. Liu, L. Wang, A biocompatible fluorescent ink based on water-soluble luminescent carbon nanodots, Angew. Chem. Int. Ed. 51 (2012) 12215–12218.
[72] Y.H. Chen, M.T. Zheng, Y. Xiao, H.W. Dong, H.R. Zhang, J.L. Zhuang, H. Hu, B. F. Lei, Y.L. Liu, A self-quenching-resistant carbon-dot powder with tunable solid-state fluorescence and construction of dual-fluorescence morphologies for white light-emission, Adv. Mater. 28 (2016) 312–318.
[73] M. Krysmann, A. Kelarakis, P. Dallas, E. Giannelis, Formation mechanism of carbogenic nanoparticles with dual photoluminescence emission, J. Am. Chem. Soc. 134 (2012) 747–750.
[74] J. Wang, C. Wang, S. Chen, Amphiphilic egg-derived carbon dots: rapid plasma fabrication, pyrolysis process, and multicolor printing patterns, Angew. Chem. Int. Ed. 51 (2012) 9297–9301.
[75] P. Long, Y. Feng, C. Cao, Y. Li, J. Han, S. Li, C. Peng, Z. Li, W. Feng, Self-protective room-temperature phosphorescence of fluorine and nitrogen codoped carbon dots, Adv. Funct. Mater. 28 (2018), 1800791.
[76] R.P. Ye, X. Wang, C.H. Price, X. Liu, Q. Yang, M. Jaroniec, J. Liu, Engineering of yolk/core-shell structured nanoreactors for thermal hydrogenations, Small 17 (2021), e1906250.
[77] L. Wang, R. Han, Y. Ma, M.S. Duyar, W. Liu, J. Liu, Spatial location and microenvironment engineering of Pt-CeO_2 nanoreactors for selective hydrogenation of cinnamaldehyde to cinnamyl alcohol, J. Phys. Chem. C 125 (2021) 22603–22610.
[78] C. Shi, S. Ye, X. Wang, F. Meng, J. Liu, T. Yang, W. Zhang, J. Wei, N. Ta, G.Q. M. Lu, M. Hu, J. Liu, Modular construction of prussian blue analog and TiO_2 dual-compartment janus nanoreactor for efficient photocatalytic water splitting, Adv. Sci. 8 (2021), 2001987.
[79] C. Dong, Q. Yu, R.P. Ye, P. Su, J. Liu, G.H. Wang, Hollow carbon sphere nanoreactors loaded with PdCu nanoparticles: void-confinement effects in liquid-phase hydrogenations, Angew. Chem. Int. Ed. 59 (2020) 18374–18379.
[80] H. Yu, Y. Zhao, C. Zhou, L. Shang, Y. Peng, Y. Cao, L. Wu, C. Tung, T. Zhang, Carbon quantum dots/TiO_2 composites for efficient photocatalytic hydrogen evolution, J. Mater. Chem. A 2 (2014) 3344–3351.
[81] B.C. Martindale, G.A. Hutton, C.A. Caputo, E. Reisner, Solar hydrogen production using carbon quantum dots and a molecular nickel catalyst, J. Am. Chem. Soc. 137 (2015) 6018–6025.
[82] W. Li, Y. Liu, M. Wu, X. Feng, S.A.T. Redfern, Y. Shang, X. Yong, T. Feng, K. Wu, Z. Liu, B. Li, Z. Chen, J.S. Tse, S. Lu, B. Yang, Carbon-quantum-dots-loaded ruthenium nanoparticles as an efficient electrocatalyst for hydrogen production in alkaline media, Adv. Mater. 30 (2018), 1800676.
[83] J. Qin, H. Zeng, Photocatalysts fabricated by depositing plasmonic Ag nanoparticles on carbon quantum dots/graphitic carbon nitride for broad spectrum photocatalytic hydrogen generation, Appl. Catal. B 209 (2017) 161–173.
[84] X. Xu, W. Tang, Y. Zhou, Z. Bao, Y. Su, J. Hu, H. Zeng, Steering photoelectrons excited in carbon dots into platinum cluster catalyst for solar-driven hydrogen production, Adv. Sci. 4 (2017), 1700273.
[85] P. Zhang, T. Song, T. Wang, H. Zeng, In-situ synthesis of Cu nanoparticles hybridized with carbon quantum dots as a broad spectrum photocatalyst for improvement of photocatalytic H_2 evolution, Appl. Catal. B 206 (2017) 328–335.
[86] V. Lau, I. Moudrakovski, T. Botari, S. Weinberger, M. Mesch, V. Duppel, J. Senker, V. Blum, B. Lotsch, Rational design of carbon nitride photocatalysts by identification of cyanamide defects as catalytically relevant sites, Nat. Commun. 7 (2016) 12165.
[87] Y. Wang, X. Liu, J. Liu, B. Han, X. Hu, F. Yang, Z. Xu, Y. Li, S. Jia, Z. Li, Y. Zhao, Carbon quantum dot implanted graphite carbon nitride nanotubes: excellent charge separation and enhanced photocatalytic hydrogen evolution, Angew. Chem. Int. Ed. 130 (2018) 5867–5873.
[88] A. Murray, S. Voskian, M. Schreier, T. Hatton, Y. Surendranath, Electrosynthesis of hydrogen peroxide by phase-transfer catalysis, Joule 3 (2019) 2942–2954.
[89] Y. Li, Y. Zhao, H. Nie, K. Wei, J. Cao, H. Huang, M. Shao, Y. Liu, Z. Kang, Interface photo-charge kinetics regulation by carbon dots for efficient hydrogen peroxide production, J. Mater. Chem. A 9 (2021) 515–522.
[90] P. Zhang, Y.Y. Tong, Y. Liu, J. Vequizo, H. Sun, C. Yang, A. Yamakata, F. Fan, W. Lin, X. Wang, W. Choi, Heteroatom dopants promote two-electron O_2

reduction for photocatalytic production of H_2O_2 on polymeric carbon nitride, Angew. Chem. Int. Ed. 59 (2020) 16209–16217.
[91] Y.X. Chuan Xia, Peng Zhu, Lei Fan, Haotian Wang, Direct electrosynthesis of pure aqueous H_2O_2 solutions up to 20% by weight using a solid electrolyte, Science 366 (2019) 226–231.
[92] Y. Dong, J. Su, S. Zhou, M. Wang, S. Huang, C.H. Lu, H. Yang, F. Fu, Carbon-based dots for the electrochemical production of hydrogen peroxide, Chem. Commun. 56 (2020) 7609–7612.
[93] Y. Shiraishi, T. Takii, T. Hagi, S. Mori, Y. Kofuji, Y. Kitagawa, S. Tanaka, S. Ichikawa, T. Hirai, Resorcinol-formaldehyde resins as metal-free semiconductor photocatalysts for solar-to-hydrogen peroxide energy conversion, Nat. Mater. 18 (2019) 985–993.
[94] Q. Wu, J.J. Cao, X. Wang, Y. Liu, Y. Zhao, H. Wang, Y. Liu, H. Huang, F. Liao, M. Shao, Z. Kang, A metal-free photocatalyst for highly efficient hydrogen peroxide photoproduction in real seawater, Nat. Commun. 12 (2021) 1–10.
[95] W. Fan, B. Zhang, X. Wang, W. Ma, D. Li, Z. Wang, M. Dupuis, J. Shi, S. Liao, C. Li, Efficient hydrogen peroxide synthesis by metal-free polyterthiophene via photoelectrocatalytic dioxygen reduction, Energy Environ. Sci. 13 (2020) 238–245.
[96] R. Ma, L. Wang, H. Wang, Z. Liu, M. Xing, L. Zhu, X. Meng, F. Xiao, Solid acids accelerate the photocatalytic hydrogen peroxide synthesis over a hybrid catalyst of titania nanotube with carbon dot, Appl. Catal. B 244 (2019) 594–603.
[97] X. Duan, H. Sun, S. Wang, Metal-free carbocatalysis in advanced oxidation reactions, Acc. Chem. Res. 51 (2018) 678–687.
[98] J. Hou, H. Li, Y. Tang, J. Sun, H. Fu, X. Qu, Z. Xu, D. Yin, S. Zheng, Supported N-doped carbon quantum dots as the highly effective peroxydisulfate catalysts for bisphenol F degradation, Appl. Catal. B 238 (2018) 225–235.
[99] J. Wang, S. Wang, Activation of persulfate (PS) and peroxymonosulfate (PMS) and application for the degradation of emerging contaminants, Chem. Eng. Sci. 334 (2018) 1502–1517.
[100] P. Devi, U. Das, A. Dalai, In-situ chemical oxidation: principle and applications of peroxide and persulfate treatments in wastewater systems, Sci. Total. Environ. 571 (2016) 643–657.
[101] H. Sun, S. Liu, G. Zhou, H. Ang, M. Tade, S. Wang, Reduced graphene oxide for catalytic oxidation of aqueous organic pollutants, ACS Appl. Mater. Interfaces 4 (2012) 5466–5471.
[102] X. Duan, Z. Ao, D. Li, H. Sun, L. Zhou, A. Suvorova, M. Saunders, G. Wang, S. Wang, Surface-tailored nanodiamonds as excellent metal-free catalysts for organic oxidation, Carbon 103 (2016) 404–411.
[103] H. Sun, C. Kwan, A. Suvorova, H. Ang, M. Tadé, S. Wang, Catalytic oxidation of organic pollutants on pristine and surface nitrogen-modified carbon nanotubes with sulfate radicals, Appl. Catal. B 154–155 (2014) 134–141.
[104] X. Duan, Z. Ao, H. Sun, S. Indrawirawan, Y. Wang, J. Kang, F. Liang, Z. Zhu, S. Wang, Nitrogen-doped graphene for generation and evolution of reactive radicals by metal-free catalysis, ACS Appl. Mater. Interfaces 7 (2015) 4169–4178.
[105] X. Duan, H. Sun, J. Kang, Y. Wang, S. Indrawirawan, S. Wang, Insights into heterogeneous catalysis of persulfate activation on dimensional-structured nanocarbons, ACS Catal. 5 (2015) 4629–4636.
[106] Urs Jans, J. Hoigné, Activated carbon and carbon black catalyzed transformation of aqueous ozone into OH- radicals, Ozone Sci. Eng. 20 (1998) 67–90.
[107] W. Han, D. Li, M. Zhang, H. X, X. Duan, S. Liu, S. Wang, Photocatalytic activation of peroxymonosulfate by surface-tailored carbon quantum dots, J. Hazard. Mater. 395 (2020), 122695.
[108] N.C.T. Martins, J. Ângelo, A.V. Girão, T. Trindade, L. Andrade, A. Mendes, N-doped carbon quantum dots/TiO_2 composite with improved photocatalytic activity, Appl. Catal. B 193 (2016) 67–74.
[109] R. Liu, H. Huang, H. Li, Y. Liu, J. Zhong, Y. Li, S. Zhang, Z. Kang, Metal nanoparticle/carbon quantum dot composite as a photocatalyst for high-Efficiency cyclohexane oxidation, ACS Catal. 4 (2013) 328–336.
[110] H. Zhang, H. Ming, S. Lian, H. Huang, H. Li, L. Zhang, Y. Liu, Z. Kang, S. Lee, Fe_2O_3/carbon quantum dots complex photocatalysts and their enhanced photocatalytic activity under visible light, Dalton Trans. 40 (2011) 10822–10825.
[111] Z. Xie, Y. Feng, F. Wang, D. Chen, Q. Zhang, Y. Zeng, W. Lv, G. Liu, Construction of carbon dots modified MoO_3/g-C_3N_4 Z-scheme photocatalyst with enhanced visible-light photocatalytic activity for the degradation of tetracycline, Appl. Catal. B 229 (2018) 96–104.
[112] Q. Zhang, P. Chen, M. Zhuo, F. Wang, Y. Su, T. Chen, K. Yao, Z. Cai, W. Lv, G. Liu, Degradation of indometacin by simulated sunlight activated CDs-loaded $BiPO_4$ photocatalyst: roles of oxidative species, Appl. Catal. B 221 (2018) 129–139.
[113] C. Xia, S. Zhu, T. Feng, M. Yang, B. Yang, Evolution and synthesis of carbon dots: from carbon dots to carbonized polymer dots, Adv. Sci. 6 (2019), 1901316.

Chapter 3: Implanting carbon ring into a carbon nitride matrix for enhanced nonradical photodegradation

3.1 Introduction and Significance

Photocatalysis is a promising and sustainable technique to treat organic pollutants in the aqueous phase. The produced photons further excite photocatalysts to form electron-hole pairs to participate in surface redox reactions. Thus, the wise selection of photocatalysts is important to establish an efficient remediation system and achieve a clean environment. To avoid secondary pollution, metal-free carbon catalysts are an alternative to metal-based semiconductors in photocatalysis. Carbon nitride (CN) is an excellent polymeric semiconductor that has been extensively used in photocatalysis-based environmental treatment. Due to its wider band gap (2.6 eV), CN is hard to be excited to generate more electron-hole pairs under visible light, limiting the photocatalytic ability. Herein, we propose a novel approach to generating CN with abundant aromatic carbon rings via pyrolysis of a mixture of polymer dots and urea. The obtained heterogeneous carbon nitride displays a higher electron-transfer capacity and lower interface impede, which improves the generation of radical and nonradical species to degrade naproxen in the solution. In the reactive process, we further analyze the reactive mechanism by EPR and chemical quenching experiments. Electrons and holes play a dominant role in removing the pollutant. We further identified the reaction pathway and found singlet oxygen originates from energy transfer, which enhances the triplet-exciton yield and reduces singlet-triplet energy gap of the matrix. This facilitates the generation of singlet oxygen through an energy transfer process, rather than electron transfer to dissolved oxygen.

The highlight of this chapter:

1. A friend and low-cost way to synthesize polymer dots.
2. Combined the polymer dots with urea to form a carbon/carbon nitride in-plane heterojunction.
3. The obtained catalyst demonstrated excellent degradation performance using low-dose photocatalysts.
4. The generation of singlet oxygen originates from singlet-triplet energy transfer.
5. The heterojunction photocatalyst demonstrates optimized optical characteristics.

3.2 Implanting carbon ring into a carbon nitride matrix for enhanced nonradical photodegradation

This Chapter is included as it appears as a journal paper published by **Yu Yao**, Jingqiang Zhang*, Kunsheng Hu, Huayang Zhang, Tara Pukala, Xiaoguang Duan*, Shaobin Wang, Implanting carbon ring into a carbon nitride matrix for enhanced nonradical photodegradation, **to be submitted**

Statement of Authorship

Title of Paper	Implanting carbon ring into a carbon nitride matrix for enhanced nonradical photodegradation
Publication Status	☐ Published ☐ Accepted for Publication ☐ Submitted for Publication ☑ Unpublished and Unsubmitted w ork w ritten in manuscript style
Publication Details	Yu Yao, Jinqiang Zhang*, Kunsheng Hu, Huayang Zhang, Tara Pukala, Xiaoguang Duan* and Shaobin Wang, Implanting carbon ring into a carbon nitride matrix for enhanced nonradical photodegradation, **to be submited**

Principal Author

Name of Principal Author (Candidate)	Yu Yao		
Contribution to the Paper	Project design and manuscript drafting.		
Overall percentage (%)	60%		
Certification:	This paper reports on original research I conducted during the period of my Higher Degree by Research candidature and is not subject to any obligations or contractual agreements with a third party that would constrain its inclusion in this thesis. I am the primary author of this paper.		
Signature		Date	20 / 03 / 2023

Co-Author Contributions

By signing the Statement of Authorship, each author certifies that:

i. the candidate's stated contribution to the publication is accurate (as detailed above);

ii. permission is granted for the candidate in include the publication in the thesis; and

iii. the sum of all co-author contributions is equal to 100% less the candidate's stated contribution.

Name of Co-Author	Shaobin Wang		
Contribution to the Paper	Supervision of the work, discussion of this manuscript and manuscript evaluation.		
Signature		Date	21/3/2023

Name of Co-Author	Xiaoguang Duan		
Contribution to the Paper	Supervision of the work, discussion of this manuscript and manuscript evaluation.		
Signature		Date	21/3/2023

Name of Co-Author	Kunsheng Hu		
Contribution to the Paper	Discussion and revision of manuscript.		
Signature		Date	20 /03 /2023

Name of Co-Author	Jinqiang Zhang		
Contribution to the Paper	Supervision of the work, discussion of this manuscript and manuscript evaluation.		
Signature		Date	20 /03 /2023

Name of Co-Author	Tara Pukala		
Contribution to the Paper	Discussion and revision of manuscript.		
Signature		Date	

Name of Co-Author	Huayang Zhang		
Contribution to the Paper	Discussion and revision of manuscript.		
Signature		Date	21/03 /2023

Implanting carbon rings into a carbon nitride matrix for enhanced nonradical photodegradation

Yu Yao[a], Jinqiang Zhang[a,*], Kunsheng Hu[a], Huayang Zhang[a], Tara Pukala[b], Xiaoguang Duan[a,*] and Shaobin Wang[a]

[a] School of Chemical Engineering, The University of Adelaide, Adelaide, SA 5005, Australia

[b] School of Physics, Chemistry and Earth Sciences, The University of Adelaide, SA 5005, Australia

[*] Corresponding authors

E-mail address: jinqiang.zhang@adelaide.edu.au (J. Zhang)

E-mail address: xiaoguang.duan@adelaide.edu.au (X. Duan)

Abstract

Photocatalysis has been proven as a prevailing technology for the remediation of wastewater, where highly reactive radicals with strong oxidation ability are generally necessary. Herein, we adopted a facile and efficient approach to synthesizing carbon/carbon nitride in-plain heterojunctions (CN-PDs), which induced a 100% nonradical photodegradation of naproxen under visible light irradiation. Experimental and characterization results revealed that the incorporated carbon rings in the carbon nitride (CN) matrix significantly accelerate the charge dynamics of excitons, leading to a higher concentration of hot carriers. In addition, a lower intersystem crossing (ISC) energy barrier was observed for the unique nanostructure compared to pristine CN, enabling an efficient energy-transfer-mediated oxygen activation to generate more singlet oxygen. An optimized composition of carbon rings ($CN\text{-}PDs_{0.1}$) enhanced the photodegradation of naproxen compared to CN. This study established the functionality-activity relationships in a nonradical photodegradation process. The findings will benefit the design and development of high-performance nonmetal photocatalysts for highly effective wastewater treatment.

Introduction

Pharmaceuticals and personal care products (PPCPs) have been ubiqueously detected in wastewater matrices, which can pose severe impacts on human health and ecosystems in the absence of reasonable treatment [1-3]. Naproxen (NPX) is a typical antibiotic pollutant, negatively affecting the behavior, development, and expression of genes involved in antioxidant defence of organisms in aquatic environments [2, 4]. More seriously, a high concentration of NPX in drinking water can pose a risk to human health due to its toxic effects on oxidative stress, bioaccumulation, and disruption of the genetic process [5, 6]. Therefore, Fenton/Fenton-like technologies have been utilized to eliminate NPX in wastewater [7, 8]. However, deficiencies of these two advanced oxidation processes (AOPs) include the reliance on activation reagents and the generation of additional pollutants, impeding their practical applications [9]. Alternatively, photocatalysis has been extensively used as a clean and sustainable technology for remediating the environment [10]. Photo-induced electrons (e^-) and holes (h^+) will participate in surface redox reactions to generate reactive oxygen species (ROS) (e.g., •OH, $O_2^{\bullet-}$ and $O_2{}^1$), which are typically highly reactive species [11-13]. Till now, most reported photodegradation processes are radical-based processes [14], and the efficiency is limited by the radical self-quenching and quenching by background substance.

Photocatalysts applied in a photodegradation reaction are primarily comprised of metal nanoparticles with plasmonic properties, organic and inorganic semiconductors, and their composites [3]. However, metal-based catalysts exhibit the limitation of being expensive and the potential for contamination in heterogeneous reactions [9]. To this end, metal-free photocatalysts are appealing for solar light harvesting and environmental remediation. Carbon nitride (CN) has shown great potential for photodegradation [15, 16]. Nevertheless, the efficiencies of CN for solar energy harvesting and waste removal remain unsatisfactory

despite decades of endeavor, due to low light absorption, small specific surface area and sluggish charge dynamics [17, 18]. Hybridization of semiconductors with other active components to establish intrinsic electric fields can improve light response capability and accelerate charge dynamics of carbon nitride photocatalysts [16, 19]. Unfortunately, the enhancement is limited at the interface of the heterojunction, as the bulk property of parent photo-active compounds is still unchanged.

Lateral heterostructures are appealing in carbon nitride-based composites due to the in-plain molecular engineering, which can maximize charge dynamics for improved photocatalysis. Che et al., used glucose as a carbon to incorporate aromatic carbon rings into the host carbon nitride, which remarkably accelerated the separation rate of charge carriers and prolonged their lifetimes for enhanced photocatalysis [20]. Besides, carbon dots have been employed to fabricate carbon ring/carbon nitride in-plane heterojunction [21, 22]. Although significant improvements in photocatalysis have been achieved on the unique structure, the percentage of carbocycles implantation remains low owing to the low and high polymerization of glucose and carbon dots, respectively. Polymer dots (PDs) are emerging organic nanomaterials, which exhibit a larger π-conjugated structure than small organic molecules but are less stable than carbon dots[23]. Therefore, PDs are good candidates as the source of carbon rings for constructing carbon/carbon nitride lateral heterojunctions.

In this work, polymer dots were synthesized and acted as the precursor of carbon rings for the assembly of carbon/carbon nitride in-plane heterojunctions. The abundant amino groups on the surface of polymer dots are beneficial to adsorbing the precursor of CN (i.e., urea molecules) and promoting the epitaxial growth of CN. The resultant planar heterojunction materials were used for the photodegradation of NPX, showing an intensified removal efficiency of organic pollutants via a nonradical mechanism. The structure-function relationship of the lateral heterostructure in photodegradation of NPX was revealed through

experimental results. Carbon rings will expedite the separation and transfer of photo-excited charge carriers in CN. As a result, the introduction of carbon rings into the carbon nitride matrix significantly reduced the energy barrier for intersystem crossing (ISC) from 0.31 eV in CN to 0.07 eV in CN-$PDs_{0.1}$. This reduction enabled enhanced energy-transfer-mediated oxygen activation, resulting in the production of more singlet oxygen, and thus, a higher removal efficiency of organic pollutants via a non-radical mechanism. This work elucidates a non-radical photodegradation process in an unique lateral heterostructure. The findings will help design and manufacture high-performance metal-free photocatalysts for efficient and green treatment of pollutants in water.

Methods and materials

Materials

Citric acid, urea, ammonium oxalate (AO), potassium dichromate ($K_2Cr_2O_7$), ethanol, ethylene diamine tetraacetic acid disodium salt dihydrate (EDTA-2Na), chloroform, 2,3,6-trimethylphenol (TMP), naproxen (NPX), sodium sulfate (Na_2SO_4), HPLC-grade acetonitrile and methanol were all purchased from Sigma-Aldrich. All the chemical reagents in this work were used without contamination. Ultra-pure water (18.2 MΩ·cm) was produced from a Milli-Q water purification system for all aqueous solutions.

Synthesis of PDs

Polymer dots were prepared via a modified hydrothermal method. Briefly, 10 g of citric acid and 10 g of urea were dissolved in 75 mL pure water with continuous magnetic stirring for 30 minutes. The solution was then transferred to a 120 mL Teflon-sealed autoclave, which was heated up to 180 ^{o}C and maintained for 12 hours. After natural cooling to room temperature, the obtained dark green suspension was centrifuged at 10000 rpm for 20 minutes to remove

the bulk particles. PDs were ultimately acquired after dialysis in 750 mL deionized water for 24 hours and a freeze-drying process for 48 hours.

Synthesis of carbon nitride/carbon in-plane heterojunction

Carbon rings were implanted into the carbon nitride matrix by a chemical epitaxial growth strategy. In a typical procedure, 20 g of urea and a certain amount (0.05, 0.1, 0.3 and 0.5 g) of PDs were dissolved into 50 mL pure water, followed by magnetic stirring for 30 mins to form a transparent green solution. The water was then heated on a hot plate at 80 °C. The obtained solid sample was fully ground, and the resultant powder was subsequently calcined in a muffle furnace at 600 ^{o}C for 1.5 h at a ramping rate of 5 ^{o}C min^{-1}. The resultants were denoted as CN-PDs-x (x = 0.05, 0.1, 0.3 and 0.5). For comparison, CN was prepared with the same method in the absence of PDs.

Characterizations

X-ray powder diffraction (XRD) pattern was collected on a Rigaku MiniFlex 600 X-ray diffractometer. Transmission electron microscopy (TEM), high-resolution transmission electron microscopy (HRTEM), high-angle annular dark-field scanning transmission electron microscopy (HAADF-STEM) images and energy-dispersive X-ray spectroscopy (EDS) spectra were obtained on a FEI Titan Themis incorporated a JEOL 2100F microscope and a HAADF detector. A Nicolet 6700 Fourier transform infrared spectrometer was used to analyze functional groups on the prepared samples. X-ray photoelectron spectroscopy (XPS) (Thermo Scientific K-Alpha+) was applied to determine the surface compositions and chemical states of the obtained catalysts. A UV-Vis spectrophotometer (Agilent Technologies, Cary Series) was used to analyze light absorption ability and estimate the bandgap of all the samples. A FLS1000 spectrometer (Edinburgh Instruments, UK) was employed to collect transient-state photoluminescence (PL) spectra and a FLS980

spectrometer (Edinburgh Instruments, UK) was used for measurements of fluorescence and phosphorescence. Steady-state PL spectra were obtained on an RF-5301PC spectro fluorophotometer (Shimadzu, Japan). N_2 adsorption-desorption isotherms were acquired by a physisorption technique (ASAP 2460). Thermogravimetric analysis was performed on a Mettler Toledo thermogravimetric analyzer. Cross-polarization (CP) magic-angle spinning nuclear magnetic resonance (MAS NMR) spectra weres collected on a Varian VNMRS WB spectrometer (^{13}C 100.554 MHz) equipped with a 4 mm MAS probe. Electron paramagnetic resonance (EPR) spectra with *in situ* light irradiation were acquired on a Bruker A300-10/12. Near edge X-ray absorption fine structure (NEXAFS) tests were carried out with the Soft-X-ray beamline from the Australian Synchrotron. Element analysis was carried out on an Elemantar Vario EL cube. Thermogravimetric analysis (TGA) was carried out in a (DSC) 2 instrument with a heat rate 5 °C/min under air atmosphere condition.

Photodegradation tests

Photodegradation performance of naproxen on the prepared photocatalysts was evaluated in a customized reactor under visible light irradiation. Specifically, 3 mg of a photocatalyst was dispersed into 50 mL of naproxen aqueous solution (20 mg/L) with magnetic stirring at 300 rpm for 30 min in the dark to achieve the adsorption-desorption equilibrium. The photocatalytic experiments were initiated using a 350 W Xenon arc lamp with a 420 nm cut-off filter for visible light illumination. The temperature of the reaction system was maintained at 25.0 ± 0.2 °C by circulating water between a double-walled quartz cooling jacket. Subsequently, 1.5 mL of suspension was extracted at specific intervals and filtered through a 0.22 μm Millipore filter for analysis. The concentration of NPX was determined by an ultrahigh performance liquid chromatograph (UHPLC, Thermo scientific 3000) with a C18 column and a UV detector (235 nm).

Photoelectrochemical measurements

Photocurrent tests and electrochemical impedance spectroscopy (EIS) measurements were conducted on a CHI 760E electrochemical workstation (CH Instruments, Inc, USA). The synthesized sample was coated on a glassy carbon electrode (GCE) and was used as the working electrode. A Pt wire and an Ag/AgCl (saturated KCl) electrode was applied as the counter electrode and reference electrode, respectively. Na_2SO_4 (0.5 M) solution was selected as the electrolyte solution. In preparation of the working electrode, 5 mg photocatalyst was dispersed into 500 uL ethanol solution containing 20 uL Nafion, and the slurry was dipped on the surface of GCE. The electrode was naturally dried by exposing in the air for three days. A Xenon lamp (Newport) was used as the light source. The illumination area of the working electrode was 1 cm^2.

Results and Discussions

Catalyst preparation and characterizations

The synthetic process of carbon ring/carbon nitride planar heterojunction (CN-PDs_x) is illustrated in **Fig. 1**a. Polymer dots (PDs) were synthesized by a hydrothermal method using urea and citric acid as precursors. The carboxyl groups of citric acid molecules reacted with amino groups of urea for acylamino groups in the resultant PDs (**Fig. S1**). PDs were then mixed and copolymerized with urea at a medium-high temperature (600 °C). Terminal amino and carboxyl groups on the surface of PDs adsorbed urea molecules, which directionally grew along the carbonated matrix of PDs for CN-PDs_x (**Fig. S6**). As such, a lateral heterostructure integrated of carbocycles and tri-s-triazine rings is acquired as a promising metal-free photocatalyst.

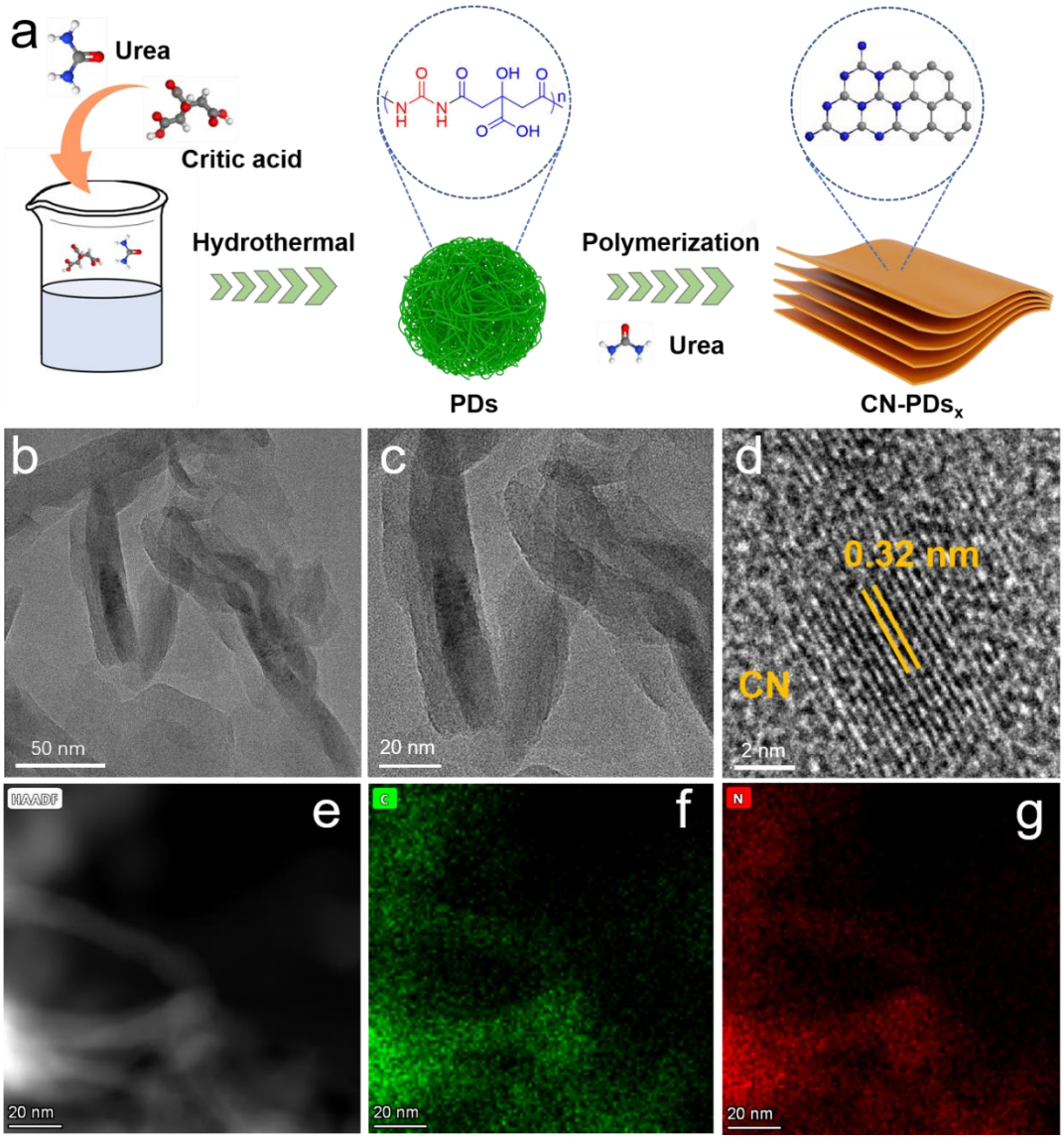

Fig. 1. Material synthesis and characterizations. (a) Illustration of synthesis of metal-free carbon/carbon nitride in-plane heterojunction. (b-c) TEM images. (d) HRTEM image of CN-$PDs_{0.1}$. (e) HAADF-STEM image and (f-g) EDX elemental mapping images of CN-$PDs_{0.1}$.

To observe the fabrication process of CN-PDs_x lateral heterojunction, transmission electron microscopy (TEM) images of PDs were captured, showing the well-defined, monodispersed and uniformly distributed nanospheres at a mean diameter of 23 nm (**Fig. S2-3**). PDs are different from carbon quantum dots as they are unstable under the attack of high energy electron beam owing to the low polymerization degree (**Fig. S2**a-d). TGA results also

confirm that PDs can be easily decomposed by 60% when the temperature rises to 125 ºC (**Fig. S4**). The TEM images depict the process of structure degradation of PDs, showing the transformation from solid spheres to hollow shells (**Fig. S2**) Therefore, PDs show a larger π-conjugated structure than small organic molecules and lower stability than carbon dots. After the copolymerization of PDs with urea at 600 ºC, clear lamellar stacking nanosheets can be observed for CN-$PDs_{0.1}$, where PDs in a nanosphere structure disappeared (**Fig. 1**b-c). By contrast, distinct lattice fringe regions can be seen from HRTEM images (**Fig. 1**d), which are incorporated into the amorphous basal plane of CN. The lattice spacing is estimated to be 0.32 nm, attributed to the interlayer stacking distance of graphene [24, 25]. In addition, we fail to find obvious boundaries or interfaces between the amorphous carbon nitride and inserted carbocycles (**Fig. 1**d), indicating the random assembly of carbon rings and carbon nitride matrix into a planar metal-free heterostructure. Furthermore, elemental mapping images of CN-$PDs_{0.1}$ display that the thin lateral heterojunction is primarily comprised of C and N elements (**Fig. 1**e-g), which are unevenly distributed on CN-$PDs_{0.1}$ as evidenced by the different C/N ratios at the two selected positions (**Fig. S5**), illustrating the existence of heterojunction across the two-dimensional plane.

We also utilized Fourier transform infrared (FTIR) spectra to confirm the process of incorporating carbon rings into the basal plane of carbon nitride. Acylamino groups at 1664 cm^{-1} can be found in the FTIR spectra of PDs, confirming the polymerization of critic acid and urea for the polymer dots (**Fig. S6**) [26]. Meanwhile, terminal carboxyl and amino groups exist on the surface of PDs, which serve as active sites for the epitaxial growth of carbon nitride along PDs. The incorporation of PDs into the carbon nitride matrix leads to a change in the vibrational bands in the FTIR spectra. After the copolymerization of PDs and urea, the intensity of the vibration bands at 806, 1000-1700, and 3000-3400 cm^{-1} **(Fig. 2**a) [26, 27], corresponding to the s-triazine unit, C-N stretching vibrations in the CN heterocycles, and

amino groups (N-H), respectively, gradually decrease with the increased amount of PDs during the fabrication of CN-PDsx. This indicates that the heptazine framework of CN is altered by the generated π-conjugated carbon ring during the carbonation with PDs.

For analysis of the chemical structure in the resultant planar heterojunction, XRD patterns of the as-prepared samples were first collected (**Fig. 2**b). Carbon nitride exhibits two diffraction peaks at 13.1 and 27.5°, where the former (100) peak is assigned to the in-plane structural packing motif of tri-s-triazine units, and the latter (002) peak originates from the interlayer-stacking structure [16]. By contrast, PDs show a broad (002) band near that of graphene reported in the literature, indicating the generation of a graphene-derived structure but with a low graphitic/polymerization degree [28]. It should be noted that the intensity for the (100) peak gradually decreases when increasing the amount of PDs in the synthetic process of CN-PDs_x. In addition, there is a slight upshift of the (002) peaks in the lateral heterojunction (**Fig. 2**c), suggesting the laterally periodic tri-s-triazine structure of carbon nitride is destroyed by the incorporated carbon rings [28, 29].

Solid-state ^{13}C NMR measurement was performed to substantiate the molecular structure before and after the insertion of carbocycles into the carbon nitride matrix. As illustrated in **Fig. 2**d, both CN and CN-$PDs_{0.1}$ show two apparent peaks at approximately 162 and 154 ppm, which are the representative assignments of CN_3 groups in heptazine rings and carbon atoms adjacent to the amino group in the heptazine units of CN, respectively [29, 30]. Additionally, a dominant shoulder peak appears at 116 ppm on CN-$PDs_{0.1}$, ascribing to aromatic C=C [31], proving the formation of carbon rings after the copolymerization of PDs and urea. The implant of carbon rings into carbon nitride basal plane is further confirmed by elemental analysis (EA). The C/N ratio presented in **Table S1** increases from 0.57 to 0.68 when the dosage of PDs in the fabrication of lateral heterojunction increases from 0 to 0.5 g, indicating a controllable content of carbocycles in resultant CN-PDs_x samples. Therefore,

PDs are proven to be an optimal precursor for fabricating carbon ring/carbon nitride lateral heterojunction.

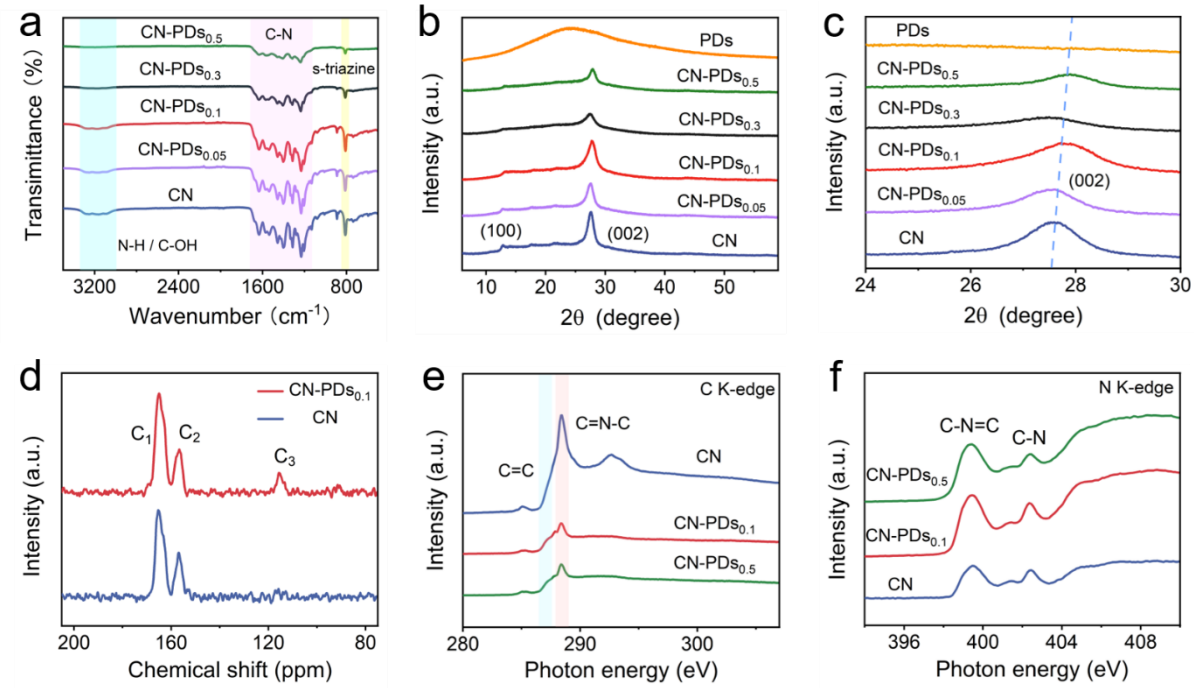

Fig. 2. Characterizations of CN and CN-PDs$_x$, including (a) FTIR spectra. (b) XRD patterns. (c) amplifying XRD patterns between 24 to 30°. (d) solid-state ^{13}C NMR spectra for CN, CN-PDs$_{0.1}$ and CN-PDs$_{0.5}$ NEXAFS results of (e) C K edge and (f) N K edge.

Near-edge X-ray absorption fine structure (NEXAFS) spectra were acquired to gain insight into the chemical structures of all samples. Peaks at 287.2 and 288.4 eV in carbon K-edge spectra **(Fig. 2**e) are assigned to the C=C and C=N-C resonances, respectively. Two typical characteristic resonances at 399.4 and 402.3 eV in the nitrogen K-edge region (**Fig. 2**f) are corresponded to the C-N-C coordination in CN units and N-3C bridging among three tri-s-triazine rings, respectively [31]. Compared with CN, we observed obvious fluctuations of C=C peak for CN-PDs$_{0.1}$ and CN-PDs$_{0.5}$, indicating the creation of carbon rings in CN-PDs-x. X-ray photoelectron spectroscopy (XPS) conforms the results of NEXAFS (**Fig. S7**). The survey XPS spectra show that CN, CN-PDs$_{0.1}$ and CN-PDs$_{0.5}$ are primarily composed of C

and N elements. As shown in C 1s spectra (**Fig. S7**a), the fitted peaks at 284.8 and 288.3 eV are indexed to the C-C/C=C bond and triazine rings (N-C=N), respectively. The N-C=N peak downshifts after the modification by carbon rings. Interestingly, the intensity of C-C/C=C peak is remarkably higher for CN-PDs$_{0.1}$ and CN-PDs$_{0.5}$ than for pristine CN, revealing the successful incorporation of graphitic carbon rings into the CN framework.

A similar trend to the C 1s spectra is also seen in the N 1s spectra (**Fig. S7**b), and three fitted N peaks at 398.7, 399.9, and 401.2 eV are assigned to C=N-C, N-(C)$_3$, and C-NH, respectively. These peaks all shift to lower binding energies with the creation of the lateral structure in CN-PDs$_{0.5}$. As a result, the various characterization techniques used in the study confirmed the successful incorporation of carbon rings into the carbon nitride matrix when PDs are used in the fabrication process.

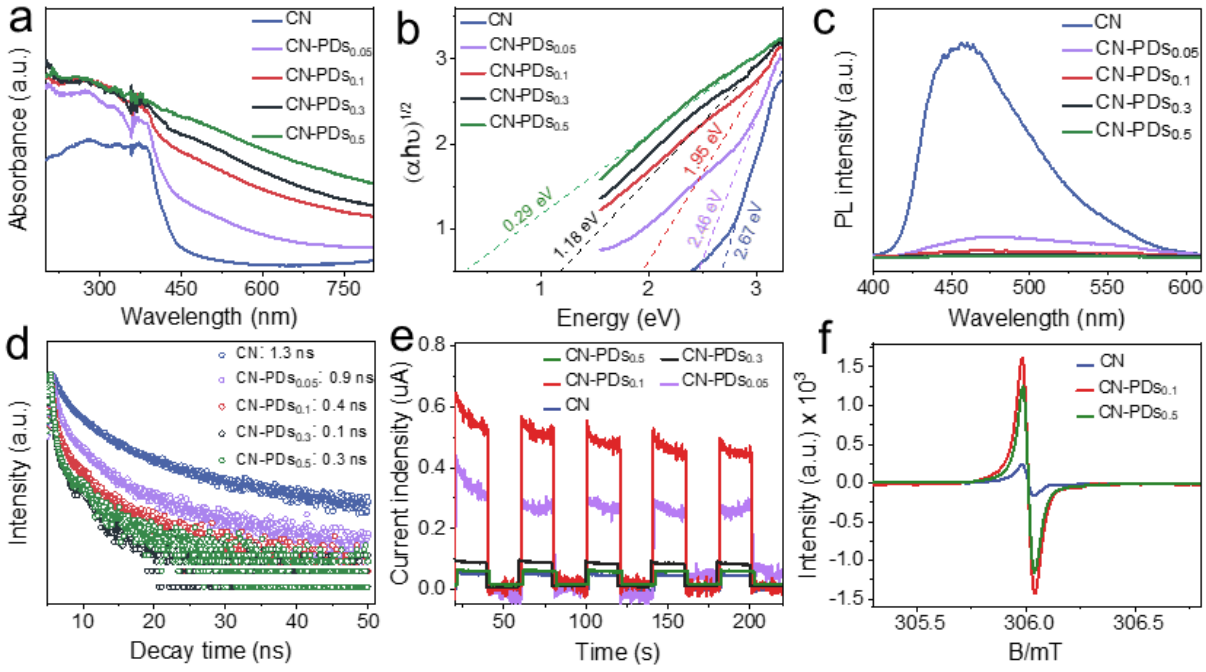

Fig. 3. Optoelectrical properties. (a) UV-Vis absorption spectra and (b) estimated band gap of CN and CN-PDs$_x$. (c) PL spectra. (d) Time-resolved transient PL decay. (e) Transient photo-current response. (f) Solid EPR spectra of CN and CN-PDs$_x$ samples.

Physicochemical properties

Nitrogen adsorption and desorption isotherms were collected to study the specific surface area (SSA) and pore structures of all the prepared samples (**Fig. S8**). CN-PDs$_{0.05}$ and CN-PDs$_{0.1}$ demonstrate lower specific surface areas than other samples, measuring 71.6 and 64.6 m^2/g, respectively. Further increasing the dosage of PDs in the fabrication process of lateral heterostructure results in a larger SSA, as demonstrated by values of 84.2, 90.8 and 90.0 m^2/g for CN, CN-PDs$_{0.3}$ and CN-PDs$_{0.5}$, respectively (**Fig. S8**b). The pore volume and pore size were determined by pore distribution curves (**Fig. S8**c), where mesoporous structures are dominant for all the samples.

Prior to the evaluation of their photocatalytic activities, the light absorption properties and photo-induced charge dynamics were assessed for all the samples. UV-Vis diffuse reflectance spectra (**Fig. 3**a) show a prominent tail, suggesting a significant enhancement in visible light absorption at the in-plane heterojunction. The marginal absorption edges of CN, CN-PDs$_{0.05}$ and CN-PDs$_{0.1}$ are 440, 460 and 520 nm, respectively, illustrating that more carbocycles in the CN-PDs$_x$ lead to intensified light responses. Furthermore, the light response on CN-PDs$_{0.3}$ and CN-PDs$_{0.5}$ even extends to the near infrared region. Based on the data collected, the band gap energy (E_g) was estimated to be 2.67 eV for CN, 2.46 eV for CN-PDs$_{0.05}$, 1.95 eV for CN-PDs$_{0.1}$, 1.18 eV for CN-PDs$_{0.3}$ and 0.29 eV for CN-PDs$_{0.5}$ (**Fig. 3**b). This suggests an approaching conductor property with more aromatic carbon rings in the lattice. The valence positions of 2.17, 2.69, 2.21, 2.16, and 2.33 eV for CN, CN-PDs$_{0.05}$, CN-PDs$_{0.1}$, CN-PDs$_{0.3}$ and CN-PDs$_{0.5}$, respectively, were determined from XPS VB spectra (**Fig. S9**). These values indicate the band structures of pristine CN and CN-PDs$_{0.1}$, which are presented in **Fig. S10**.

The dynamics of photo-induced charge carriers were then investigated for all the samples. First, PL spectra were used to study the separation rate of photo-excited electron-hole pairs (**Fig. 3**c). When excited at the wavelength of 325 nm, pristine CN displays a strong emission

peak at approximately 460 nm. The peak intensity is the highest among all the samples, indicating the fastest recombination rate of electron-hole pairs. Noticeably, PL peak intensity gradually decreases with the increased density of carbon rings in CN-PDs$_x$, demonstrating that carbon motifs within the CN matrix significantly accelerate charge separation and decrease the recombination rate of e^- and h^+ pairs. In addition, the fluorescence lifetime of CN and CN-PDs-x samples is acquired to better analyze photo-induced charge dynamics (**Fig. 3**d). Photo-excited hot electrons exhibit the longest lifetime of 1.3 ns in CN, which is larger than CN-PDs$_{0.3}$ at the value of 0.1 ns. The lifetime of the photo-excited charge carriers decreases as more PDs are added in the fabrication of lateral heterojunction, as illustrated by the lifetime of 0.9, 0.4, and 0.3 ns for CN-PDs$_{0.05}$ CN-PDs$_{0.1}$, and CN-PDs$_{0.5}$, respectively. The shorter transient fluorescence decay lifetime (τ) is related to exciton radiative decay from the conduction band to the valence band. Incorporating carbon rings in the carbon nitride matrix can enhance the separation and transfer of photo-excited charge carriers by efficiently trapping the photogenerated electrons, resulting in a shorter fluorescence decay lifetime (τ).

Furthermore, the enhanced photo-induced charge dynamics in the lateral heterostructure is further verified by the photoelectrochemical measurements. A photocurrent response is recorded to assess the separation and transportation efficiency of photo-induced charge carriers. It can be obviously observed that the photocurrent for CN-PDs$_x$ sharply increases compared to pristine CN, indicating a higher charge separation rate after carbon rings grow along the CN basal plane (**Fig. 3**e). The EIS plots also suggest that CN has the largest radius among all the obtained materials, indicating its higher interface impedance resistance. On the other hand, the addition of more carbon rings in CN-PDs$_x$ remarkably lowers the interface impedance resistance, promoting the migration of photogenerated charge carriers (**Fig. S11**) [32]. EPR spectra confirm the enhanced charge dynamics in CN-PDs$_x$, as the paramagnetic signal at a g factor of 2.003 is ascribed to the unpaired electrons. CN-PDs$_{0.1}$ and CN-PDs$_{0.5}$

show higher EPR peaks than CN (**Fig. 3**f), indicating the addition of carbon rings into carbon nitride improves the separation efficiency of electron and hole pairs [33]. Based on the above results, conclusions can be reached that the electronic structure of CN matrix has been greatly modified via the insertion of carbon ring, leading to efficient photoexcited electron-hole separation and fast charge migration dynamics.

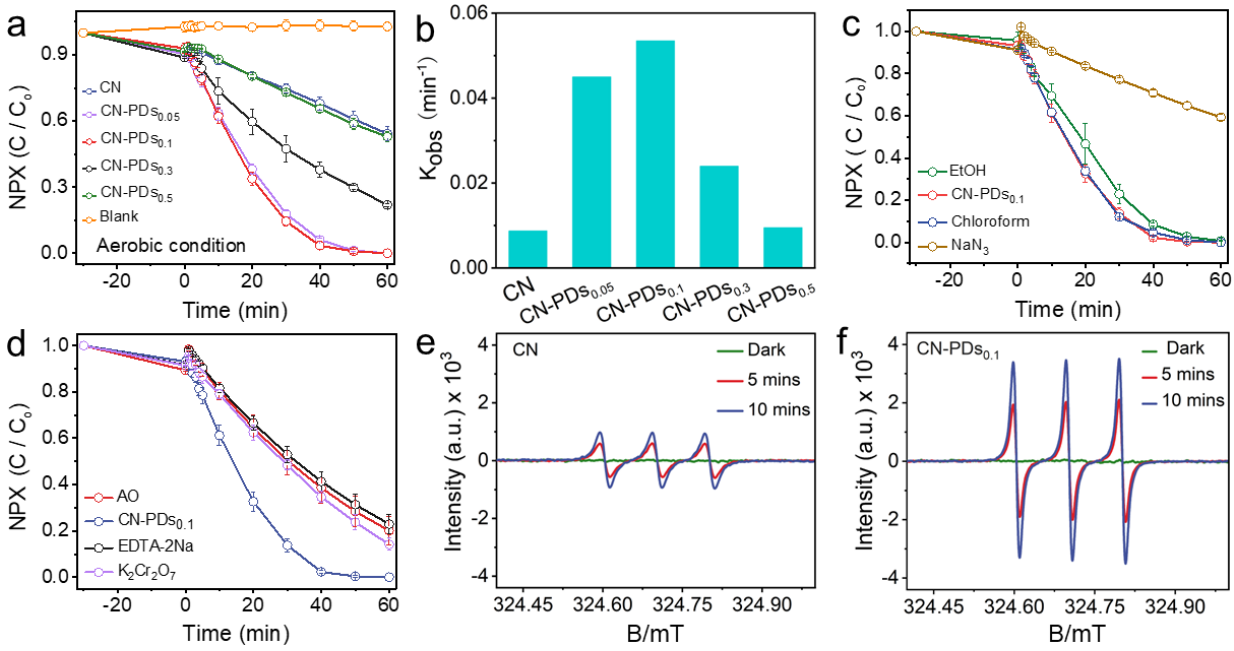

Fig. 4. Performance evaluation. (a) NPX photodegradation efficiency by CN and CN-PDs$_x$. (b) Kinetic constants of NPX photodegradation for all of samples. (c-d) Trapping experiments of CN-PDs$_{0.1}$ based photodegradation of NPX with different scavengers. Catalyst amount: 0.06 g/L; Naproxen concentration: 20 mg/L. (e-f) EPR measurements for singlet oxygen in photodegradation of NPX on CN and CN-PDs$_{0.1}$.

Photodegradation performance

NPX was chosen as the target pollutant to evaluate the photodegradation performance of all the metal-free photocatalysts under visible light irradiation. In the absence of catalysts, no appreciable changes in NPX concentration were observed after 60-min visible light irradiation (blank line in **Fig. 4**a), indicating the neglectable self-photolysis of NPX. A 90-

minute adsorption experiment was conducted for NPX in the absence of light irradiation. The concentration of NPX stops descending after 30 min, meaning the adsorption-desorption equilibrium is reached within half an hour (**Fig. S12**).

Photodegradation process is initiated upon activation of visible light. Using pristine CN, the photodegradation efficiency of NPX is lower, with only approximately 45% of NPX removal within 60 minutes of light irradiation. The lower photodegradation efficiency observed with pristine CN can be largely attributed to sluggish charge dynamics and an unsatisfactory surface area. Implanting carbon rings into the carbon nitride basal plane leads to improved photocatalytic activity for NPX removal in the aqueous solution. Specifically, the NPX removal efficiencies for CN-PDs$_{0.05}$, CN-PDs$_{0.1}$, CN-PDs$_{0.3}$ and CN-PDs$_{0.5}$ are 100%, 100%, 80% and 45%, respectively. CN-PDs$_{0.1}$ with an optimal content of immobilized carbocycles exhibits the highest photocatalytic activity, while further improving the PDs amount during the synthesis results in declined photocatalytic activity. This is because more carbon rings would destroy the semiconducting property of carbon nitride and result in less energetic hot carriers upon light irradiation, despite the improvement in the photo-induced charge dynamics (**Fig. 3**b) [34].

The kinetic constants for the prepared samples in photodegradation of NPX are presented to compare their photocatalytic performances. Pseudo-first order kinetic curves are revealed for all the samples in the photodegradation process (**Fig. 4**b and **Fig. S**13). The kinetic constant for CN-PDs$_{0.1}$ is 0.05 min^{-1}, which is 1.2 and 5.5 times greater than that of CN-PDs$_{0.05}$ and CN, respectively, suggesting the faster photodegradation of NPX on CN-PDs$_{0.1}$.

Reactive species detection and reaction mechanism

To clarify the reaction mechanism of the photodegradation of NPX, we conducted quenching experiments to monitor various reactive species. As shown in **Fig. 4**c-d, the photocatalytic activities remained unaffected after adding ethanol and chloroform as quenchers for •OH and

$O_2^{\bullet-}$, respectively. The results suggest that •OH and $O_2^{\bullet-}$ are not responsible for the degradation of NPX. However, when $K_2Cr_2O_7$ was added to the photodegradation system, the kinetic constant for NPX degradation decreased from 0.05 to 0.03 min^{-1} (**Fig. S14**). Since $K_2Cr_2O_7$ is a typical electron trapping agent, the reduced photocatalytic performance suggests that photo-induced hot electrons are responsible for the photodegradation of NPX.

In addition, adding AO and EDTA-2Na resulted in changes to the kinetic constant from 0.05 min^{-1} to 0.02 and 0.03 min^{-1}, respectively (**Fig. S14**a). These findings demonstrate that photo-excited e^- and h^+ are also reactive species involved in the photodegradation process, contributing to NPX removal. Furthermore, we introduced NaN_3 as a specific quencher of $^1O_2$ into the photocatalytic system (**Fig. 4**c). The results indicate that the involvement of $^1O_2$ in the photocatalytic degradation process, as the NPX removal rate decreased from 0.05 to 0.009 min^{-1} upon the addition of NaN_3 (**Fig. S14**b). The activation of $^1O_2$ by CN-PDs$_{0.1}$ under visible light irradiation was also confirmed by EPR measurements (**Fig. 4**e-f), where a characteristic signal with a peak ratio of 1:1:1 (ascribed to $^1O_2$) was observed after light irradiation. The results confirm that nonradical photodegradation process involves photo-induced hot carriers and $^1O_2$, when using CN-PDs$_x$ as photocatalysts for NPX removal.

To distinguish the contributions of $^1O_2$ and photo-excited hot carriers to the nonradical mechanism, the photodegradation of NPX was performed under an anaerobic condition. As depicted in **Fig. 5**a, the removal efficiencies of CN and CN-PDs$_{0.5}$ under 60-min visible light irradiation were 30% and 28%, respectively. In addition, NPX removal efficiency of 95%, 100% and 50% were achieved using CN-PDs$_{0.05}$, CN-PDs$_{0.1}$ and CN-PDs$_{0.3}$, respectively. The first-order kinetic rate constants for all catalysts were slightly decreased under anaerobic conditions, compared to aerobic conditions (**Fig. 5**b). These results suggest that $^1O_2$ contributes to the photodegradation of NPX. Furthermore, the photodegradation rates of NPX were significantly reduced upon additions of $K_2Cr_2O_7$ and EDTA-2Na, respectively (**Fig.**

S15). Therefore, it can be concluded that photo-induced hot electrons and holes dominate the NPX removal, while singlet oxygen makes a minor contribution to the nonradical photodegradation process in the presence of oxygen. It is noteworthy that CN-PDs$_{0.1}$ exhibits 100% NPX removal efficiency under both aerobic and anaerobic conditions, suggesting it is a promising bifunctional photocatalyst for wastewater treatment.

To investigate the pathway of NPX photodegradation, we analyzed reactive intermediates using LC-MS. Only one by-product with m/z of 201 was detected in the LC-MS spectra (**Fig. S16**). Based on these findings, a possible reaction mechanism can be proposed for the nonradical photodegradation process (**Fig. 5**c). The proposed mechanism suggests that photo-generated hot electrons and singlet oxygen act as scissors, cleaving NPX molecules into 1-(6-methoxynaphtalen-2-yl) ethanol [35]. This intermediate is further mineralized or oxidized by photo-induced hot holes into CO_2 and H_2O.

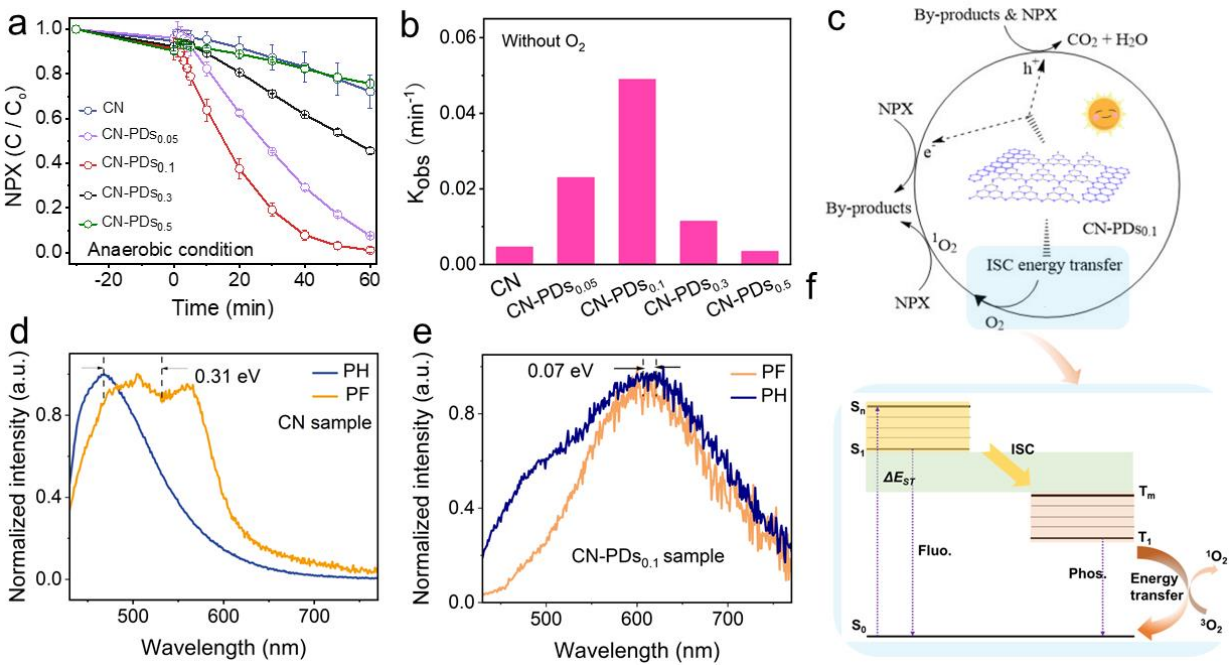

Fig. 5. Structure-performance relationships. (a) Anaerobic photodegradation efficiency for all of samples (N_2 purge). (b) Kinetic constants of anaerobic photodegradation for all of samples. (c) Proposed mechanism of NPX removal under the visible light irradiation conditions. (d-e) Normalized fluorescence (PF) and phosphorescence spectra (PH) of CN and CN-PDs$_{0.1}$ at

room temperature (excitation wavelength at 365 nm and delay time is 1 ms). (f) Diagram of the photoexcitation energy transfer process of CN-PDs$_{0.1}$ for singlet oxygen.

Discussions

The activation of singlet oxygen on the planar heterojunction was studied. Because $O_2^{\bullet-}$ is not detected (**Fig. 4**c), it can be inferred that $^1O_2$ is not generated by an electron transfer mechanism. The introduction of TMP as a quencher for $^1O_2$ into the photocatalytic system with N_2 bubbling can help unveil the origin of $^1O_2$ [36]. The kinetic constant of NPX photodegradation is sharply reduced to 0.0025 min^{-1} (**Fig. S15**), proving the production of $^1O_2$, possibly via an energy-transfer pathway. The singlet-triplet energy gap (ΔE_{st}) for CN and CN-PDs$_{0.1}$ was determined using fluorescence (fluo.) and phosphorescence (phos.) lifetimes in order to estimate the efficiency of the intersystem crossing (ISC) process. The values of ΔE_{st} were calculated to be 0.07 and 0.31 eV for CN-PDs and CN, respectively (**Fig. 5**d-e). This suggests that the immobilization of carbon rings into carbon nitride matrix enables a better triplet-triplet energy transfer process, making the ISC process easier and producing singlet oxygen (**Fig. 5**f). Therefore, the relationship between the structure and performance of the planar heterostructure in the photodegradation of NPX can be revealed. The incorporated carbocycles into the lateral heterostructure significantly accelerate the excitation, separation, and transfer of photo-induced hot carriers, resulting in the degradation of NPX (**Fig. 3c-e**). Additionally, the carbon rings in the planar heterostructure decrease the barrier for intersystem crossing, resulting in improved energy transfer and oxygen activation, ultimately leading to the generation of $^1O_2$ (**Fig. 4**e-f). As a result, the metal-free in-plain heterojunction photocatalyst enables fast charge and energy transfer, leading to enhanced photodegradation of NPX. The photocatalysis harnesses oxidative holes, hot electrons, and singlet oxygen for nonradical oxidation.

Conclusion

In summary, polymer dots were innovatively utilized to fabricate metal-free carbon/carbon nitride in-plane heterostructures. The lower carbonization degree and larger π-conjugated structure were used to produce a resultant lateral heterojunction with controllable contents of carbon ring contents. The incorporated carbocycles significantly expedited the separation and transportation of photo-excited charge carriers in carbon nitride. Meanwhile, the incorporation of aromatic rings significantly reduced the energy barrier of ISC, enabling enhanced energy-transfer-mediated oxygen activation to produce $^1O_2$ without involving radical intermediates. As a result, the photodegradation of NPX was achieved through the combined action of reactive h^+, e^-, and $^1O_2$. This work presents a new type of metal-free plane heterostructure photocatalysts for the purification of antibiotics from water through state-of-the-art nonradical oxidation.

Acknowledgments

The authors acknowledge the help from the analytical lab in the School of Chemical Engineering at The University of Adelaide, and Duan acknowledges the financial support from Australian Research Council under DECRA Scheme (DE210100253).

Declaration of Competing Interest

The authors declare that they have no known competing financial interests or personal relationships that could have appeared to influence the work reported in this paper.

References

[1] Q.G. Fu, T. Malchi, L.J. Carter, H. Li, J. Gan, B. Chefetz, Pharmaceutical and personal care products: from wastewater treatment into agro-food Systems, Environ. Sci. Technol. 53 (2019) 14083-14090.

[2] C. Xu, L. Niu, H. Guo, X. Sun, L. Chen, W. Tu, Q. Dai, J. Ye, W. Liu, J. Liu, Long-term exposure to the non-steroidal anti-inflammatory drug (NSAID) Naproxen causes thyroid disruption in zebrafish at environmentally relevant concentrations, Sci. Total. Environ. 676 (2019) 387-395.

[3] C. Chen, W. Ma, J. Zhao, Semiconductor-mediated photodegradation of pollutants under visible-light irradiation, Chem. Soc. Rev. 39 (2010) 4206-4219.

[4] M. Manrique-Moreno, M. Suwalsky, F. Villena, P. Garidel, Effects of the nonsteroidal anti-inflammatory drug naproxen on human erythrocytes and on cell membrane molecular models, Biophys. Chem. 147 (2010) 53-58.

[5] J. Wang, X.G. Duan, J. Gao, Y. Shen, X.H. Feng, Z.J. Yu, X.Y. Tan, S.M. Liu, S.B. Wang, Roles of structure defect, oxygen groups and heteroatom doping on carbon in nonradical oxidation of water contaminants, Water Res. 185 (2020) 116244.

[6] D. Wojcieszynska, U. Guzik, Naproxen in the environment: its occurrence, toxicity to nontarget organisms and biodegradation, Appl. Microbiol. Biotechnol. 104 (2020) 1849-1857.

[7] J. Kang, H. Zhang, X. Duan, H. Sun, X. Tan, S. Liu, S. Wang, Magnetic Ni-Co alloy encapsulated N-doped carbon nanotubes for catalytic membrane degradation of emerging contaminants, Chem. Eng. J. 362 (2019) 251-261.

[8] J. Wang, X. Duan, J. Gao, Y. Shen, X. Feng, Z. Yu, X. Tan, S. Liu, S. Wang, Roles of structure defect, oxygen groups and heteroatom doping on carbon in nonradical oxidation of water contaminants, Water Res. 185 (2020) 116244.

[9] X.G. Duan, H.Q. Sun, S.B. Wang, Metal-free carbocatalysis in advanced oxidation reactions, Acc. Chem. Res. 51 (2018) 678-687.

[10] Y. Yao, H.Y. Zhang, K.S. Hu, G. Nie, Y.Y. Yang, Y.X. Wang, X.G. Duan, S.B. Wang, Carbon dots based photocatalysis for environmental applications, J. Environ. Chem. Eng. 10 (2022) 107336.

[11] G. Chen, Y. Yu, L. Liang, X. Duan, R. Li, X. Lu, B. Yan, N. Li, S. Wang, Remediation of antibiotic wastewater by coupled photocatalytic and persulfate oxidation system: A critical review, J. Hazard. Mater. 408 (2021) 124461.

[12] F. Zhao, Y. Liu, S.B. Hammouda, B. Doshi, N. Guijarro, X. Min, C.-J. Tang, M. Sillanpää, K. Sivula, S. Wang, MIL-101Fe/g-C_3N_4 for enhanced visible-light-driven photocatalysis toward simultaneous reduction of Cr (VI) and oxidation of bisphenol A in aqueous media, Appl. Catal. B: Environ. 272 (2020) 119033.

[13] J. Ke, X. Duan, S. Luo, H. Zhang, H. Sun, J. Liu, M. Tade, S. Wang, UV-assisted construction of 3D hierarchical rGO/Bi_2MoO_6 composites for enhanced photocatalytic water oxidation, Chem. Eng. J. 313 (2017) 1447-1453.

[14] F.M. Yavitt, T.E. Brown, E.A. Hushka, M.E. Brown, N. Gjorevski, P.J. Dempsey, M.P. Lutolf, K.S. Anseth, The Effect of Thiol Structure on allyl sulfide photodegradable hydrogels and their application as a degradable scaffold for organoid passaging, Adv. Mater. 32 (2020) e1905366.

[15] B. Ai, X.G. Duan, H.Q. Sun, X. Qiu, S.B. Wang, Metal-free graphene-carbon nitride hybrids for photodegradation of organic pollutants in water, Catal. Today 258 (2015) 668-675.

[16] J.Q. Zhang, Y.G. Li, X.L. Zhao, H.Y. Zhang, L. Wang, H.J. Chen, S.J. Wang, X.Y. Xu, L. Shi, L.C. Zhang, J.P. Veder, S.Y. Zhao, G. Nealon, M.B. Wu, S.B. Wang, H.Q. Sun, A hydrogen-initiated chemical epitaxial growth strategy for in-plane heterostructured photocatalyst, Acs Nano 14 (2020) 17505-17514.

[17] Y. Wei, Y. Zhu, Y. Jiang, Photocatalytic self-cleaning carbon nitride nanotube intercalated reduced graphene oxide membranes for enhanced water purification, Chem. Eng. J. 356 (2019) 915-925.

[18] Z. Mo, H. Xu, Z. Chen, X. She, Y. Song, J. Wu, P. Yan, L. Xu, Y. Lei, S. Yuan, H. Li, Self-assembled synthesis of defect-engineered graphitic carbon nitride nanotubes for efficient conversion of solar energy, Appl. Catal. B: Environ. 225 (2018) 154-161.

[19] Y.Z. Liu, H.Y. Zhang, J. Ke, J.Q. Zhang, W.J. Tian, X.Y. Xu, X.G. Duan, H.Q. Sun, M.O. Tade, S.B. Wang, 0D MoS_2/2D g-C_3N_4 heterojunctions in Z-scheme for enhanced photocatalytic and electrochemical hydrogen evolution, Appl. Catal. B: Environ. 228 (2018) 64-74.

[20] W. Che, W. Cheng, T. Yao, F. Tang, W. Liu, H. Su, Y. Huang, Q. Liu, J. Liu, F. Hu, Z. Pan, Z. Sun, S. Wei, Fast photoelectron transfer in (Cring)-C_3N_4 plane heterostructural nanosheets for overall water splitting, J. Am. Chem. Soc. 139 (2017) 3021-3026.

[21] L. Cheng, H. Zhang, X. Li, J. Fan, Q. Xiang, Carbon-graphitic carbon nitride hybrids for heterogeneous photocatalysis, Small 17 (2021) e2005231.

[22] H.R.S. Abdellatif, G. Zhang, X.T. Wang, D.T. Xie, J.T.S. Irvine, J.P. Ni, C.S. Ni, Boosting photocatalytic oxidation on graphitic carbon nitride for efficient photocatalysis by heterojunction with graphitic carbon units, Chem. Eng. J. 370 (2019) 875-884.

[23] M. Semeniuk, Z.H. Yi, V. Poursorkhabi, J. Tjong, S. Jaffer, Z.H. Lu, M. Sain, Future perspectives and review on organic carbon dots in electronic applications, ACS Nano 13 (2019) 6224-6255.

[24] J.Y. Qin, H.P. Zeng, Photocatalysts fabricated by depositing plasmonic Ag nanoparticles on carbon quantum dots/graphitic carbon nitride for broad spectrum photocatalytic hydrogen generation, Appl. Catal. B: Environ. 209 (2017) 161-173.

[25] Q.L. You, Q.X. Zhang, M.B. Gu, R.J. Du, P. Chen, J. Huang, Y.J. Wang, S.B. Deng, G. Yu, Self-assembled graphitic carbon nitride regulated by carbon quantum dots with optimized electronic band structure for enhanced photocatalytic degradation of diclofenac, Chem. Eng. J. 431 (2022) 133927.

[26] F.L. Wang, P. Chen, Y.P. Feng, Z.J. Xie, Y. Liu, Y.H. Su, Q.X. Zhang, Y.F. Wang, K. Yao, W.Y. Lv, G.G. Liu, Facile synthesis of N-doped carbon dots/g-C_3N_4 photocatalyst with enhanced visible-light photocatalytic activity for the degradation of indomethacin, Appl. Catal. B: Environ. 207 (2017) 103-113.

[27] W. Liu, Y.Y. Li, F.Y. Liu, W. Jiang, D.D. Zhang, J.L. Liang, Visible-light-driven photocatalytic degradation of diclofenac by carbon quantum dots modified porous g-C_3N_4: mechanisms, degradation pathway and DFT calculation, Water Res. 150 (2019) 8-19.

[28] Y. Wang, R. Godin, J.R. Durrant, J.W. Tang, Efficient hole trapping in carbon dot/oxygen-modified carbon nitride heterojunction photocatalysts for enhanced methanol production from CO_2 under neutral conditions, Angew. Chem. Int. Ed. 60 (2021) 20811-20816.

[29] Z.H. Chen, T. Li, Y. Zhu, X.Y. Liang, Z.Y. Zhao, D. Wang, J.H. Li, Y.W. Gao, C. Hu, Efficient light-free activation of peroxymonosulfate by carbon ring conjugated carbon nitride for elimination of organic pollutants, Chem. Eng. J. 420 (2021) 129671.

[30] A. Indra, A. Acharjya, P.W. Menezes, C. Merschjann, D. Hollmann, M. Schwarze, M. Aktas, A. Friedrich, S. Lochbrunner, A. Thomas, M. Driess, Boosting visible-light-driven photocatalytic hydrogen evolution with an integrated nickel phosphide-carbon nitride system, Angew. Chem. Int. Ed. 56 (2017) 1653-1657.

[31] J.Q. Zhang, Y.G. Li, X.L. Zhao, L. Wang, H.J. Chen, S.J. Wang, X.Y. Xu, L. Shi, L.C. Zhang, Y.Z. Zhu, H.Y. Zhang, Y.Z. Liu, G. Nealon, S. Zhang, M.B. Wu, S.B. Wang, H.Q. Sun, Aligning potential differences within carbon nitride based photocatalysis for efficient solar energy harvesting, Nano Energy 89 (2021) 106357.

[32] S. Liu, D. Liu, Y. Sun, P. Xiao, H. Lin, J. Chen, X.-L. Wu, X. Duan, S. Wang, Enzyme-mimicking single-atom FeN_4 sites for enhanced photo-Fenton-like reactions, Appl. Catal. B: Environ. 310 (2022) 121327.

[33] J.Q. Zhang, X.H. An, N. Lin, W.T. Wu, L.Z. Wang, Z.T. Li, R.Q. Wang, Y. Wang, J.X. Liu, M.B. Wu, Engineering monomer structure of carbon nitride for the effective and mild photooxidation reaction, Carbon 100 (2016) 450-455.

[34] X.M. Liu, F.T. He, Y.M. Lu, S.L. Wang, C.C. Zhao, S.J. Wang, X.G. Duan, H.Y. Zhang, X.L. Zhao, H.Q. Sun, J.Q. Zhang, S.B. Wang, The double-edged effect of single atom metals on photocatalysis, Chem. Eng. J. 453 (2023) 139833.

[35] N. Jallouli, K. Elghniji, O. Hentati, A.R. Ribeiro, A.M. Silva, M. Ksibi, UV and solar photodegradation of Naproxen: TiO_2 catalyst effect, reaction kinetics, products identification and toxicity assessment, J. Hazard. Mater. 304 (2016) 329-336.

[36] P. Gan, Y. Lu, Y. Li, W. Liu, L. Chen, M. Tong, J. Liang, Nonradical degradation of organic pharmaceuticals by g-C_3N_4 under visible light irradiation: the overlooked role of excitonic energy transfer, J. Hazard. Mater. 445 (2023) 130549.

Supporting Information

Implanting carbon ring into carbon nitride matrix for enhanced nonradical photodegradation

Yu Yao[a], Jinqiang Zhang[a*], Kunsheng Hu[a], Huayang Zhang[a], Tara Pukala[b], Xiaoguang Duan[a*] and Shaobin Wang[a]

[a] School of Chemical Engineering, The University of Adelaide, North Terrace, Adelaide, SA 5005, Australia

[b] School of Physics, Chemistry and Earth Sciences, The University of Adelaide, SA 5005, Australia

[*] Corresponding authors

E-mail address: jinqiang.zhang@adelaide.edu.au (J. Zhang)
E-mail address: xiaoguang.duan@adelaide.edu.au (X. Duan)

Table S1 Elemental analysis for CN and CN-PDs$_x$.

Sample	Element content (%)		Ratio of C/N
	N	C	
CN	60.9	34.6	0.57
CN-PDs$_{0.05}$	60.6	34.7	0.57
CN-PDs$_{0.1}$	59.4	34.3	0.58
CN-PDs$_{0.3}$	56.7	35.6	0.63
CN-PDs$_{0.5}$	54.4	36.9	0.68

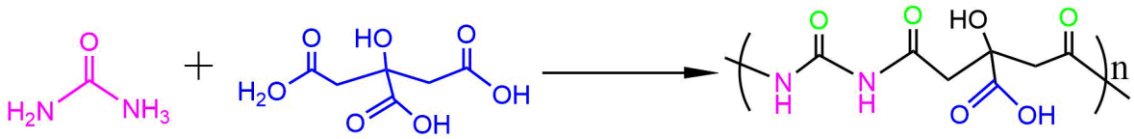

Fig. S1 Polymerization of PDs from critic acid and urea.

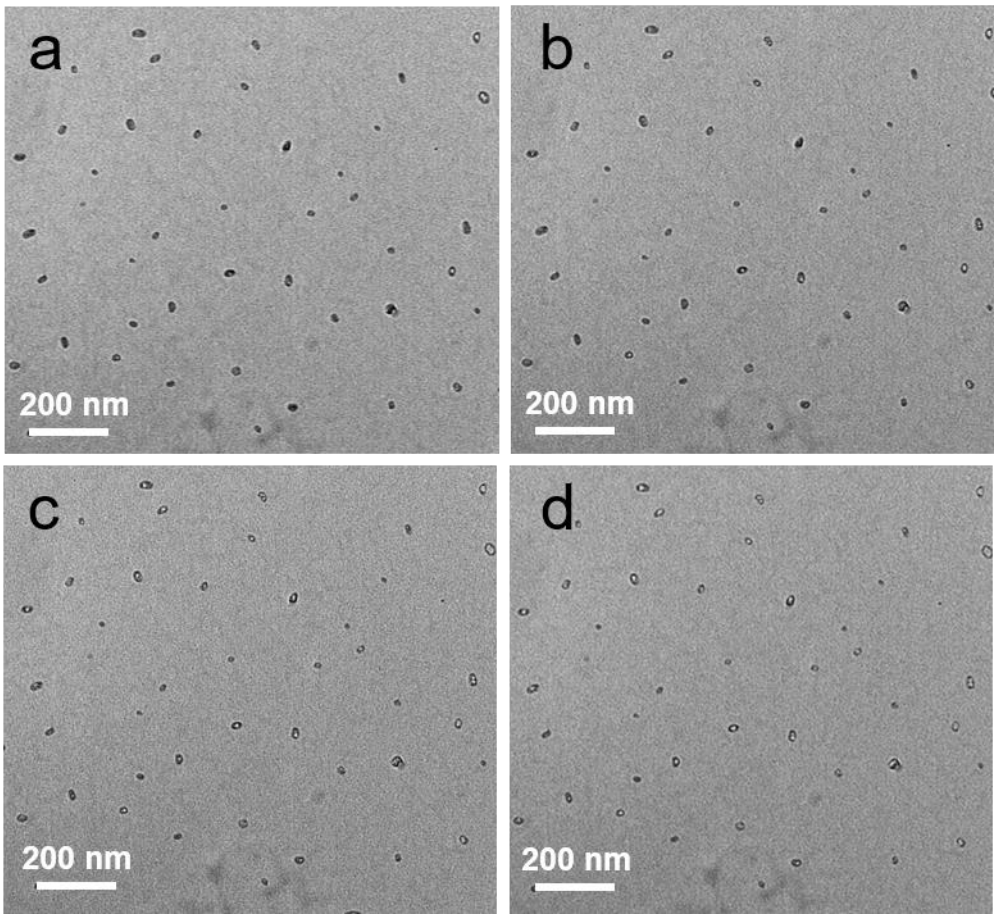

Figure S2. TEM images of PDs. (a-d) The gradual destruction from solid sphere to hollow shells under electron beam irradiation indicates that PDs are easy to decompose.

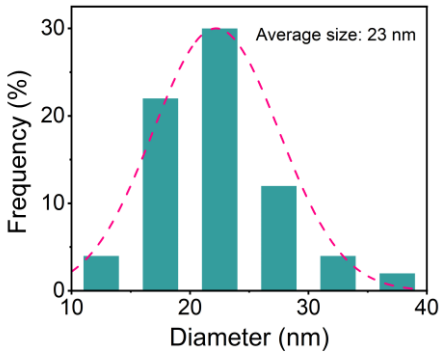

Fig. S3 Size distribution histogram of PDs.

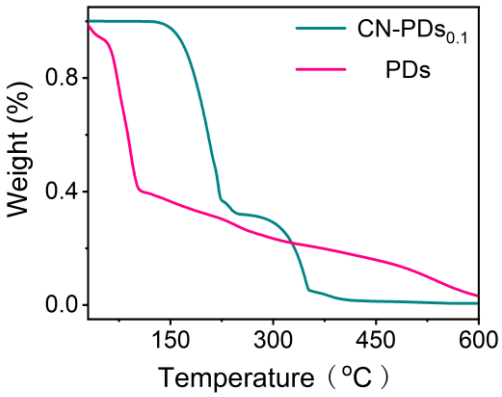

Fig. S4 Thermogravimetry (TGA) curves for PDs and CN-PDs$_{0.1}$.

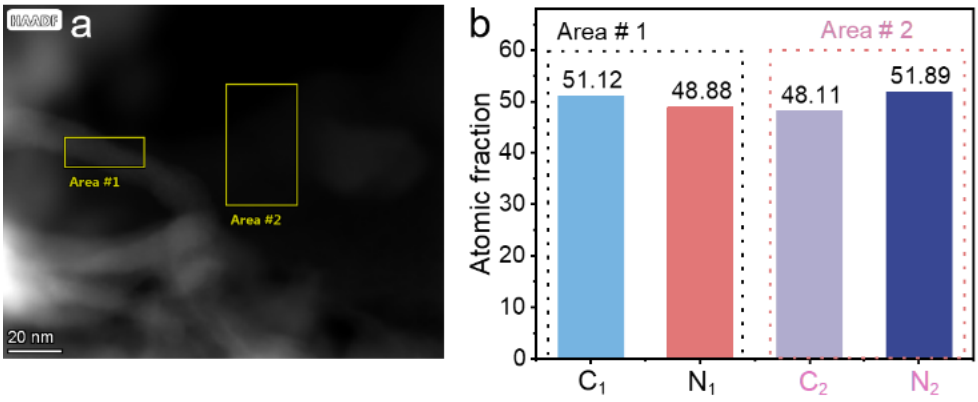

Fig. S5 Elemental distribution on CN-PDs$_{0.1}$ with different C/N ratios at the two selective positions.

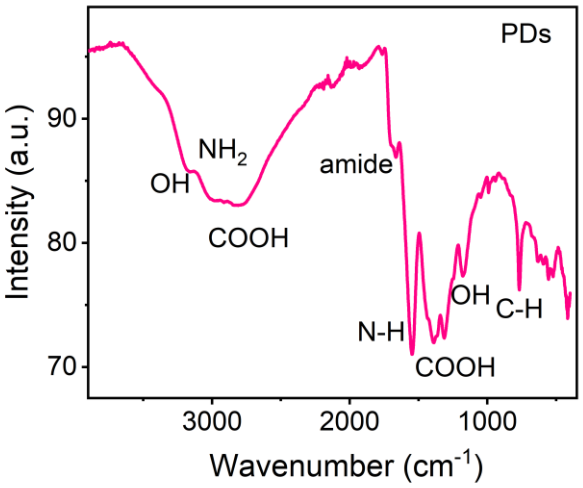

Fig. S6. Fourier transform infrared (FTIR) spectra of PDs.

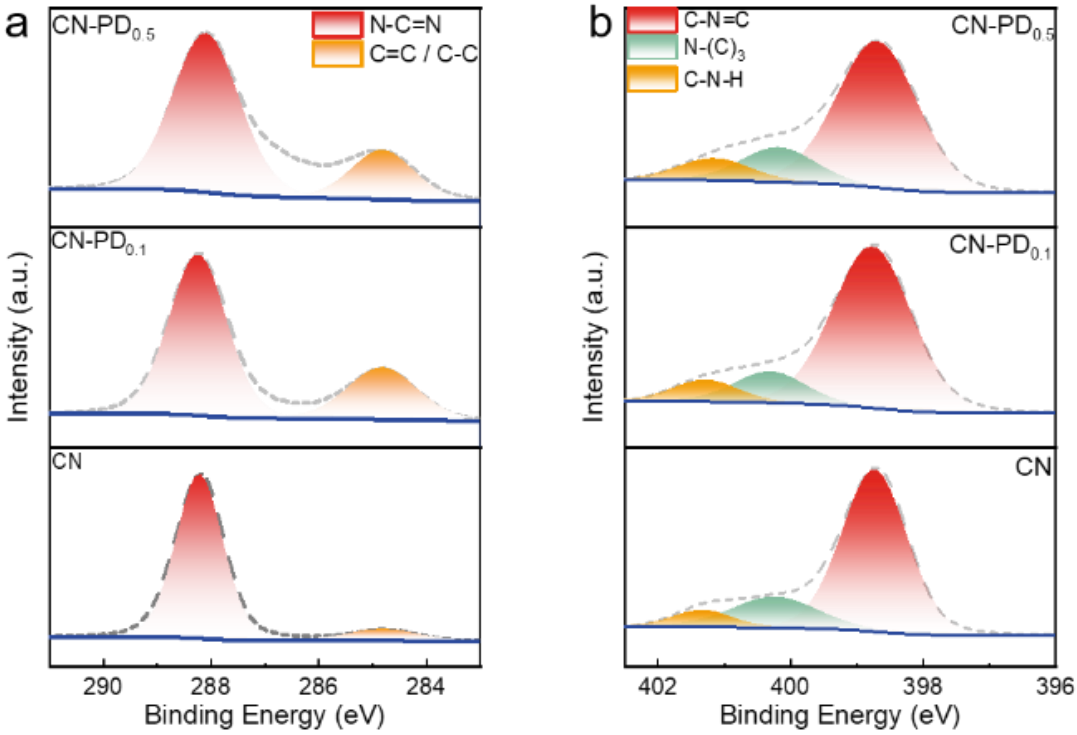

Fig. S7 High-resolution XPS spectra of CN, CN-PDs$_{0.1}$ and CN-PDs$_{0.5}$. (a) C 1s and (b) N 1s.

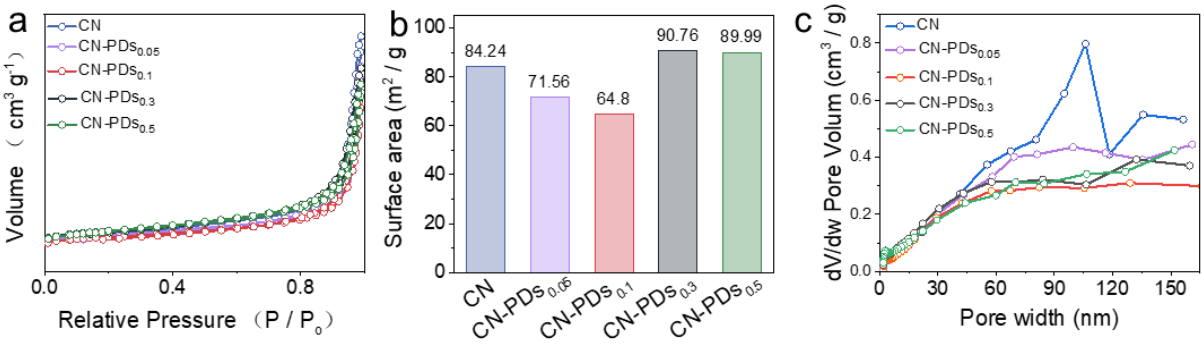

Fig. S8 (a) N_2 adsorption/desorption isotherm curves. (b) specific surface area, and (c) pore size of CN and CN-PDs$_x$.

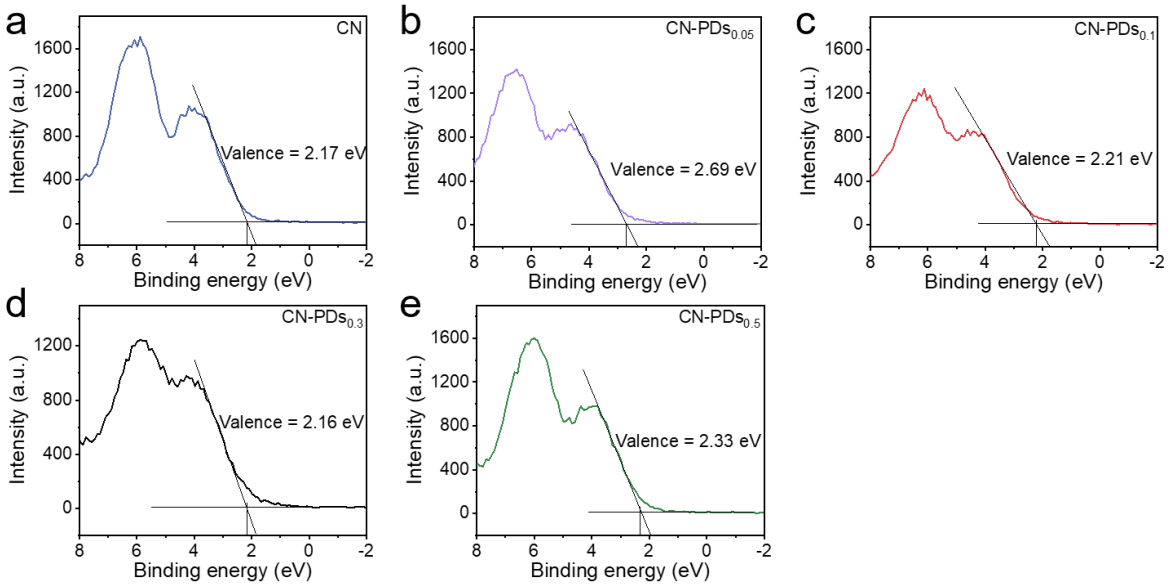

Fig. S9 Valence band XPS spectra of (a) CN. (b) CN-PDs$_{0.05}$. (c) CN-PDs$_{0.1}$. (d) CN-PDs$_{0.3}$, and (e) CN-PDs$_{0.5}$.

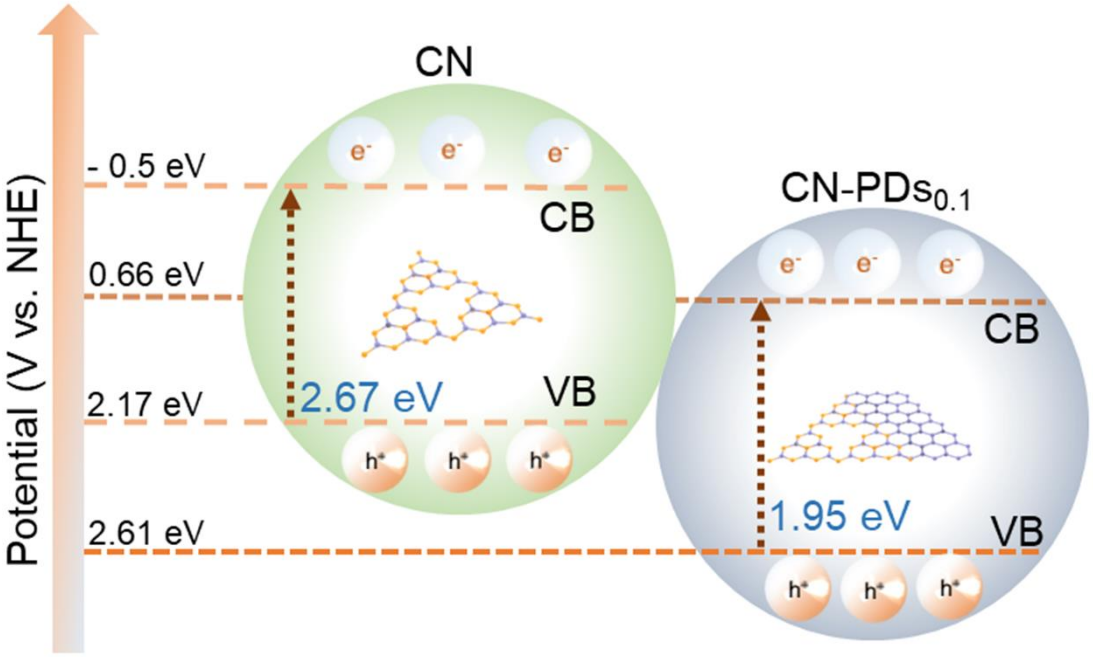

Fig. S10 Band structures of pristine CN and CN-PDs$_{0.1}$.

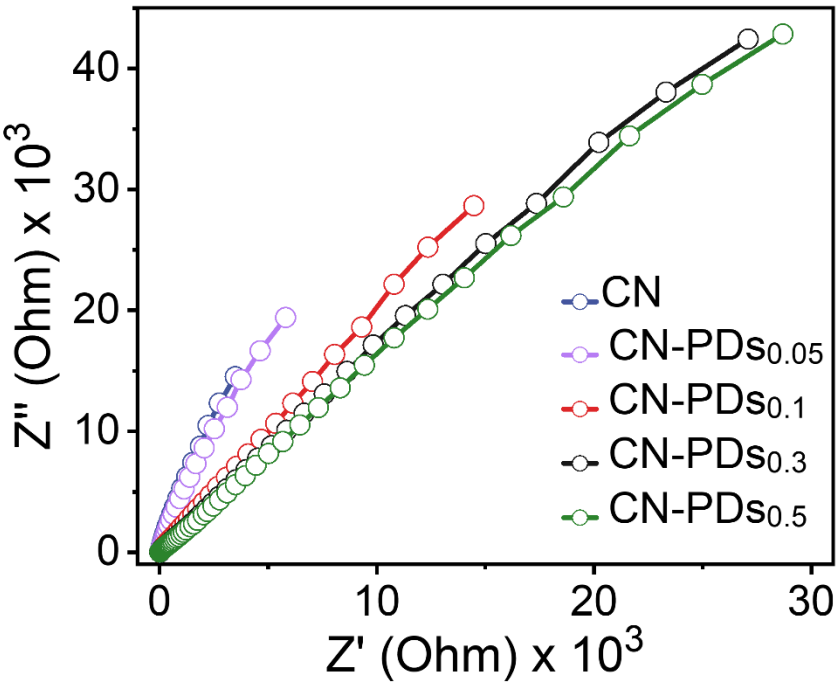

Fig. S11 EIS spectra of CN and CN-PDs$_x$.

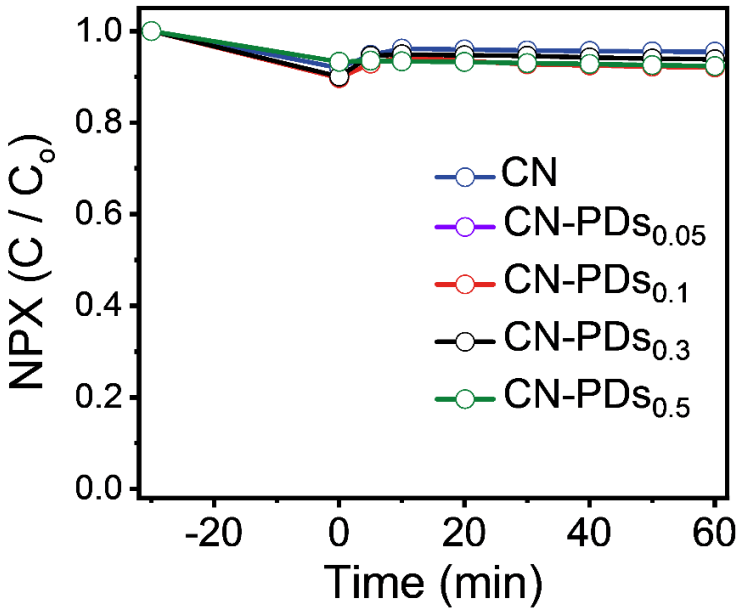

Fig. S12 NPX degradation (adsorption) in dark using different photocatalysts.

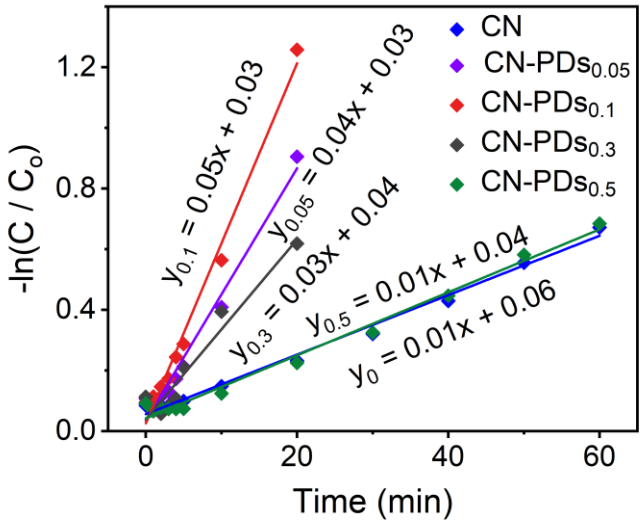

Fig. S13 NPX degradation rate constants (k_{obs}) for all catalysts.

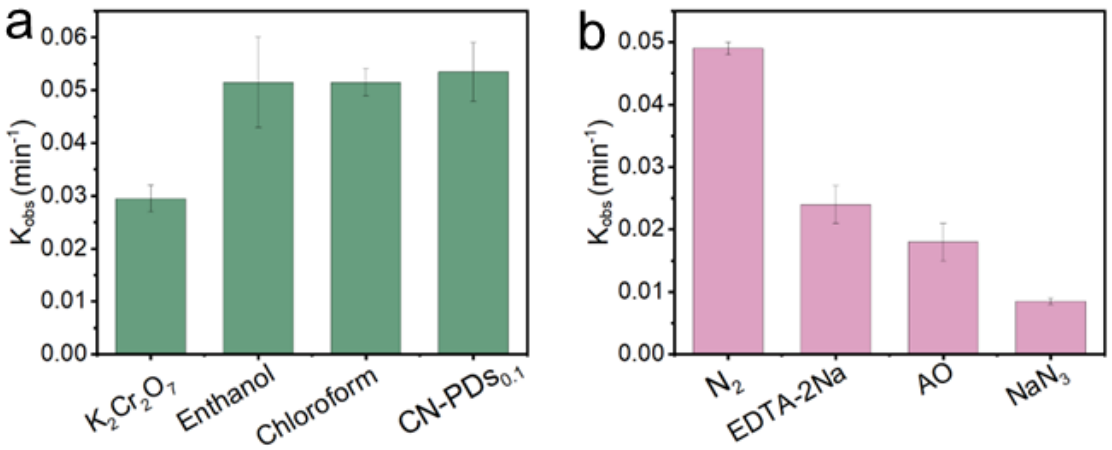

Fig. S14 (a-b) Kinetic constants of photodegradation for CN-PDs$_{-0.1}$ under aerobic conditions with different scavengers.

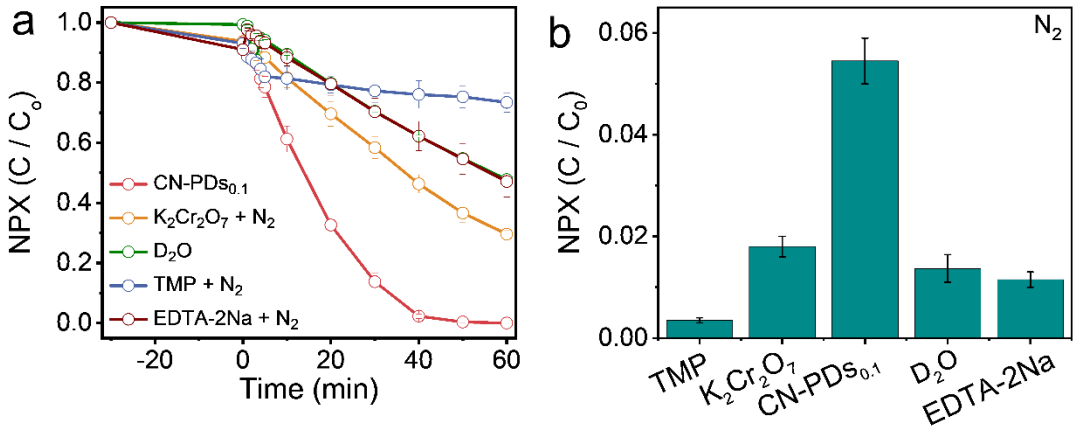

Fig. S15 (a) Quenching experiment of photodegradation efficiency for sample CN-PDs$_{0.1}$ (N_2 purge). (b) Kinetic constants of anaerobic photodegradation.

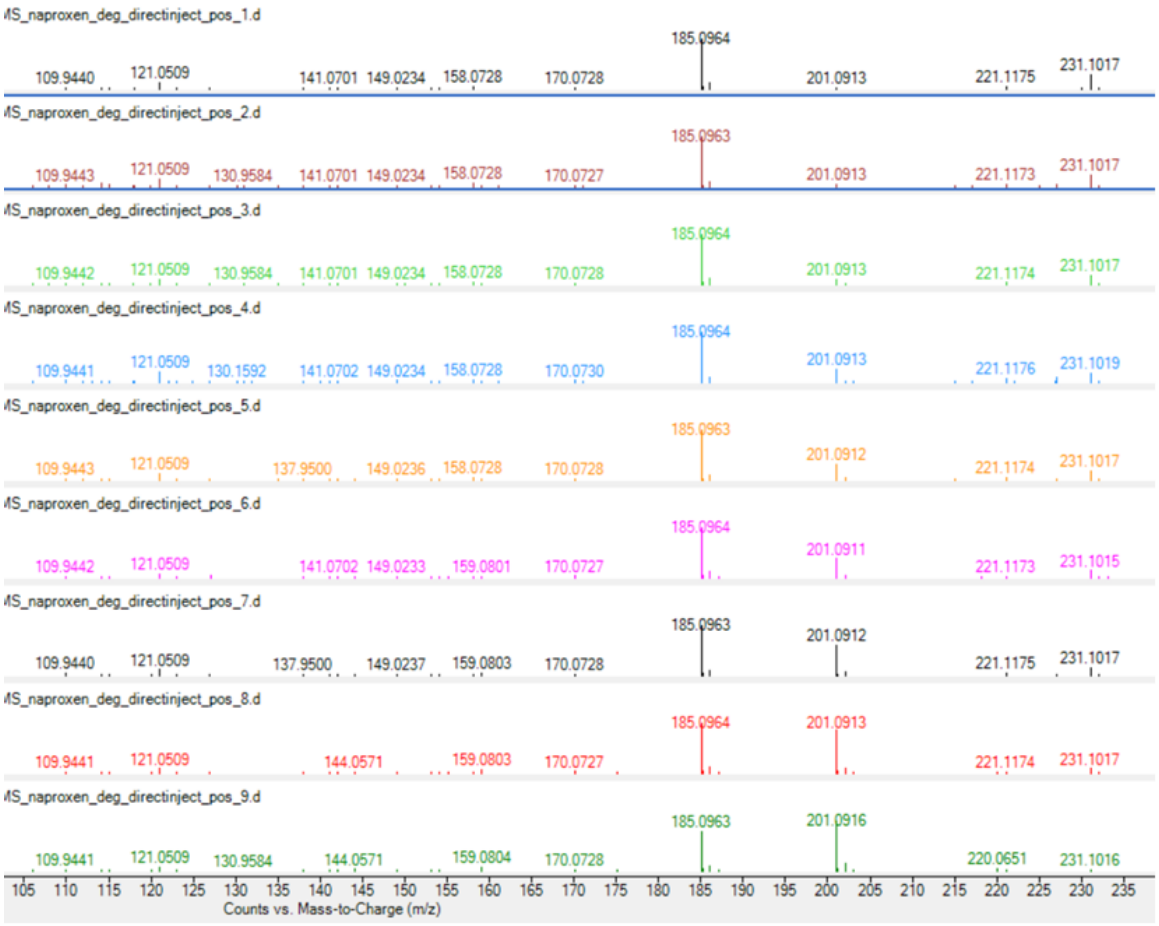

Fig. S16 LCMS results for monitoring reactive intermediates during photodegradation of NPX.

Chapter 4: An epitaxial growth strategy for nitrogen-rich carbon materials to efficiently activate peroxymonosulfate towards wastewater treatment

4.1 Introduction and Significance

In this chapter, we mainly present a facile approach to synthesizing nitrogen-rich carbon materials (N-C) at mild conditions. In the production of the N-doped carbon catalysts, two steps are involved. First, polymer dots are obtained via a hydrothermal method, where urea and citric acid are used as the precursors. The resulting polymer dots are then encapsulated by the urea and subjected to calcination at a relatively low temperature to manufacture N-C. Interestingly, carbon nitride is acquired without the involvement of polymer dots. Various advanced techniques, including transmission electron microscopy, Raman spectroscopy, X-ray diffraction, etc., are adopted to study the morphology and chemical structure of N-C. The developed carbon material with enriched nitrogen is used in peroxymonosulfate (PMS) activation for removal of 1,4-dihydro-2,6-dimethylpyridine-3,5dicarboxylate (1,4-DHP) from wastewater. Compared with traditional carbon-based materials (e.g., graphene and carbon nanotubes), the fabricated N-C demonstrates an excellent catalytic performance, which is attributed to the abundant active sites of doped nitrogen atoms and structural defects.

The highlight points of this paper

1. Synthesis of nanoscaled polymer dots via a simple, low cost and sustainable method;
2. Fabrication of N-C by copolymerization of polymer dots and urea, realizing high contents of N dopant and structural defect at mild conditions;
3. Applying N-C material into PMS activation for 1,4-DHP degradation, achieving a better catalytic performance than carbon nitride, graphene and carbon nanotube.

4.2 An epitaxial growth strategy for nitrogen-rich carbon materials to efficiently activate peroxymonosulfate towards wastewater treatment

This Chapter is included as it appears as a journal paper published by **Yu Yao**, Jingqiang Zhang*, Kunsheng Hu, Yangyang Yang, Shuang Zhong, Zhongshuai Zhu, Xiaoguang Duan*, Shaobin Wang, **to be submitted**

Statement of Authorship

Title of Paper	An epitaxial growth strategy for nitrogen-rich carbon materials to efficiently activate peroxymonosulfate towards wastewater treatment
Publication Status	☐ Published ☐ Accepted for Publication ☐ Submitted for Publication ☑ Unpublished and Unsubmitted w ork w ritten in manuscript style
Publication Details	Yu Yao, Jinqiang Zhang*, Kunsheng Hu, Huayang Zhang, Yangyang Yang, Shuang Zhong, Xiaoguang Duan* and Shaobin Wang, An epitaxial growth strategy for nitrogen-rich carbon materials to efficiently activate peroxymonosulfate towards wastewater treatment, **to be submited**

Principal Author

Name of Principal Author (Candidate)	Yu Yao		
Contribution to the Paper	Project design and manuscript drafting.		
Overall percentage (%)	60%		
Certification:	This paper reports on original research I conducted during the period of my Higher Degree by Research candidature and is not subject to any obligations or contractual agreements with a third party that would constrain its inclusion in this thesis. I am the primary author of this paper.		
Signature		Date	20 / 03 / 2023

Co-Author Contributions

By signing the Statement of Authorship, each author certifies that:

i. the candidate's stated contribution to the publication is accurate (as detailed above);

ii. permission is granted for the candidate in include the publication in the thesis; and

iii. the sum of all co-author contributions is equal to 100% less the candidate's stated contribution.

Name of Co-Author	Shaobin Wang		
Contribution to the Paper	Supervision of the work, discussion of this manuscript and manuscript evaluation.		
Signature		Date	21/3/2023

Name of Co-Author	Xiaoguang Duan		
Contribution to the Paper	Supervision of the work, discussion of this manuscript and manuscript evaluation.		
Signature		Date	21/3/2023

Name of Co-Author	Kunsheng Hu		
Contribution to the Paper	Discussion and revision of manuscript.		
Signature		Date	20 /03 /2023

Name of Co-Author	Jinqiang Zhang		
Contribution to the Paper	Supervision of the work, discussion of this manuscript and manuscript evaluation.		
Signature		Date	21 /03 /2023

Name of Co-Author	Shuang Zhong		
Contribution to the Paper	Discussion and revision of manuscript.		
Signature		Date	20 /03 /2023

Name of Co-Author	Huayang Zhang		
Contribution to the Paper	Discussion and revision of manuscript.		
Signature		Date	21/03 /2023

Name of Co-Author	Yangyang Yang		
Contribution to the Paper	Discussion and revision of manuscript.		
Signature		Date	20 / 03 / 2023

An epitaxial growth strategy for nitrogen-rich carbon materials to efficiently activate peroxymonosulfate towards wastewater treatment

Yu Yao[a], Jinqiang Zhang[a,*], Kunsheng Hu[a], Yangyang Yang[b], Zhongshuai Zhu[a], Shuang Zhong[a], Xiaoguang Duan[a*], and Shaobin Wang[a]

[a] School of Chemical Engineering, The University of Adelaide, Adelaide, SA 5005, Australia

[b] School of Chemistry and Chemical Engineering, Jiangsu University, Zhenjiang 212013, China

[*] Corresponding authors

E-mail address: jinqiang.zhang@adelaide.edu.au (J. Zhang)

E-mail address: xiaoguang.duan@adelaide.edu.au (X. Duan)

Abstract

Nitrogen-doped carbon (N-C) materials as effective and metal-free carbocatalysts have demonstrated great potentials in environmental purification. However, the thermodynamic instability of carbon-nitrogen skeleton makes N-C difficult to achieve a high content of nitrogen and desirable catalytic active sites. Herein, we developed an epitaxial growth approach to synthesize two-dimensional N-C nanosheets. The abundant amino groups on the surface of polymer dots serve as growing sites for urea molecules to achieve a high N content and structural defects in the carbon framework. The resulting N-C exhibits excellent catalytic activity for the activation of peroxymonosulfate (PMS) to remove a pollutant of 1,4-dihydro-2,6-dimethylpyridine-3,5dicarboxylate (1,4-DHP) in aqueous solutions. Experiments and advanced techniques confirmed that N sites and defects in N-C serve as the primary active sites to activate PMS and oxidize 1,4-DHP. This work presents a novel approach to manufacture active carbon materials for highly efficient and sustainable environmental remediation.

Introduction

1,4-dihydro-2,6-dimethylpyridine-3,5-dicarboxylate (1,4-DHP) is extensively used for medical and biological synthesis, such as nifedipine, felodipine, and nimodipine [1, 2]. However, improper handling of 1,4-DHP can cause contamination in oceans and rivers, even in our drinking water [3, 4]. As such, tremendous efforts have been devoted to developing efficient technologies to degrade organic pollutants in wastewater. Photocatalytic technology has drawn increasing attention for degradation of 1,4-DHP in aqueous solution due to its sustainablity and environmentally friendly benignness. Although various homogeneous and heterogeneous photocatalysts have extensively been exploited and applied in the oxidation of 1,4-DHPs, high efficiency remains a challenge due to the low sunlight harvesting efficiency and sluggish charge dynamics of state-of-the-art photocatalysts [5]. As a result, an efficient and clean approach is highly desirable for large scale degradation of 1,4-DHP in wastewater.

Peroxymonosulfate (PMS) as an inexpensive oxidant has widely been applied in advanced oxidation processes (AOPs) for pollutant removal [6, 7], while has yet been reported for the degradation of 1,4-DHP. The generated sulfate radical ($SO_4^{\bullet-}$) after PMS activation exhibits a strong oxidation ability. Therefore, various energy sources, including thermal energy [8], ultrasound [12], ultraviolet and visible light [11, 13] etc. have been introduced to promote the activation of PMS. However, the more external energy consumption and higher costs on facilities impede the practical application of PMS oxidation technology. Alternatively, heterogeneous and homogeneous metal-based catalysts have evidenced to be efficient to activate perdisulfate (PDS) and PMS into reactive species [9]. Unfortunately, metal-containing sludge is inevitable after the wastewater treatment, which may result in secondary pollution in aqueous solutions [14, 15].

Carbonaceous materials [10], especially nitrogen doped carbon (N-C) materials, have emerged as green alternatives to metal catalysts in PMS activation processes owing to their sustainable nature and excellent catalytic activities [15]. In addition, the unsaturated coordination environment of a nitrogen dopant and structural defect generally serve as active sites to accelerate the activation of PMS [15]. However, harsh pyrolysis conditions are highly required in the fabrication of nitrogen doped carbon materials, posing a significant challenge in the synthesis of N-C [17, 18]. More importantly, the N content of the state-of-the-art nitrogen doped carbon materials remains as low as 7.41%, severely hindering their application in wastewater treatment [16]. Therefore, an economic approach is of great significance to prepare high-performance N doped carbon-based catalysts for advanced water purification.

In this paper, we proposed an epitaxial growth approach to synthesize N-C materials. The abundant amino groups on the surface of polymer dots (PDs) enabled the growth of urea to form a N-C catalyst. Compared with the high synthetic temperature (900 ^{o}C) and low content of nitrogen dopant (7.8%) by a conventional N-C preparation method, this strategy could reduce the fabrication temperature to 600 ^{o}C and increase the content of N dopant to 38%. Interestingly, carbon nitride was obtained without PDs in the polymerization of urea. The resulting N-C catalyst was for the first time utilized in the PMS activation to degrade 1,4-DHP. Compared with other carbon-based materials (i.e., carbon nitride, graphene and carbon nanotube), N-C exhibits outstanding catalytic performance in PMS activation for the degradation of 1,4-DHP, attributing to the more N dopants and structural defects. Experimental and characterization results collectively identified the dominant reactive oxygen species (ROS) of singlet oxygen ($^{1}O_2$) and superoxide ($O_2^{\bullet-}$) and revealed the reaction mechanism in the N-C/PMS system for 1,4-DHP removal.

Materials and methods

Chemical regents

Citric acid, urea, ammonium oxalate (AO), multi-walled carbon nanotube (M-CNT), graphene plate (G-plate), ethanol (EtOH), potassium peroxymonosulfate (PMS, Oxone®), chloroform, L(+)-ascorbic acid (L-ac), furfuryl alcohol (FFA), 1,4-dihydro-2,6-dimethylpyridine-3,5-dicarboxylate (1,4-DHP), 5,5-dimethyl-1-pyrroline N-oxide (DMPO) and 2,2,6,6-tetramethyl-4-piperidinol (TEMP) were purchased from Sigma-Aldrich. Pure water was produced by an ultrapure water purifier (18.2 MΩ•cm).

Preparation of PDs

Polymer dots were synthesized via a modified hydrothermal method. Specifically, 10 g of citric acid and 10 g of urea were dissolved in 75 mL of pure water with continuous stirring for 30 minutes. The resulting solution was then transferred to a 120 mL Teflon-sealed autoclave, which was heated at 180 ^{o}C for 12 hours. After natural cooling to room temperature, the obtained dark green suspension was centrifuged at 10000 rpm for 20 minutes to remove the bulk particles. PDs was ultimately acquired after a dialysis process in 750 mL of deionized water for 24 hours.

Synthesis of nitrogen doped carbon

The N-C material was prepared by a chemical epitaxial growth strategy. In a typical procedure, 20 g of urea and 10 mL of PDs solution were added to 50 mL of pure water and stirred continuously for 30 minutes to form a transparent green solution. The water was then thoroughly removed on a hot plate at 80 °C. The solid was fully ground, and the resultant powder was subsequently calcined in a muffle furnace at 600 ^{o}C for 1.5 hours with a ramping rate of 5 ^{o}C min^{-1}. For comparison, graphitic carbon nitride (CN) was prepared using the

same method in the absence of PDs. N-C ($_{CA+U}$) was prepared by calcination of a mixture of 10 g of citric acid and 10 g of urea under the same conditions.

Degradation of 1,4-DHP

The catalytic performance of the samples was evaluated in the PMS activation for degradation of 1,4-DHP. In detail, 25 mg of 1,4-DHP was dissolved into 1 L of ethanol/water (volume ratio of 1:1) with magnetic stirring for 1 hour to obtain 1,4-DHP solution. About 5 mg/L of catalyst was dispersed into 50 mL of 1,4-DHP solution and stirred for 30 mins to achieve adsorption-desorption equilibrium. Then, 0.2 mM of PMS was added to the solution to initiate the reaction. The reaction system temperature was maintained at 25 °C. In the reaction process, 2.5 mL of the reaction solution was periodically extracted through a syringe, and the catalyst was filtered by a 0.22 um polyether sulfone millipore film. The concentration of 1,4-DHP was monitored using a UV-Vis spectrophotometer (Agilent Technologies, Cary Series) to determine the degradation efficiency.

Characterizations

X-ray powder diffraction (XRD) was collected using a Rigaku MiniFlex 600 X-ray diffractometer. Transmission electron microscopy (TEM) images were captured on FEI Tecnai G2 Spirit. High-resolution transmission electron microscopy (HRTEM) images and energy-dispersive X-ray spectroscopy (EDS) spectra were obtained using a FEI Titan Themis microscope incorporated with a JEOL 2100F microscope with a high-angle annular dark field (HAADF) detector. The Brunauer Emmett and Teller (BET) technique was performed using an ASAP 2460 Version 3.0. A Nicolet 6700 Fourier transform infrared spectrometer (FTIR) was used to analyze the functional groups on the prepared samples. X-ray photoelectron spectroscopy (XPS) was used to determine the surface compositions and chemical states of the obtained catalysts. Cross-Polarization magic-angle spinning nuclear magnetic resonance

(MAS NMR) spectra were collected using a Varian VNMRS WB spectrometer (^{13}C 100.554 MHz) equipped with a 4 mm MAS probe. Electron paramagnetic resonance (EPR) spectra using DMPO and TEMP were acquired on a Bruker A300–10/12. A Raman spectroscopy instrument (Horiba Scientific, Germany) equipped with a laser emitting at 532 nm was used.

Results and discussions

Synthesis and characterization of N-C

The synthetic process for the N-C material is illustrated in **Fig. 1**. Initially, PDs were synthesized through a hydrothermal method using urea and citric acid as precursors. TEM image shows that PDs are evenly dispersed with the average size of around 20 nm (**Fig. 2**a-b). Subsequently, the resulting PDs were mixed and copolymerized with urea at 600 °C. Terminal amino and carboxyl groups on the surface of the PDs adsorb urea molecules and serve as growing sites for urea molecules, which assemble into nitrogen doped carbon rings along the carbonated matrix of PDs to form N-C.

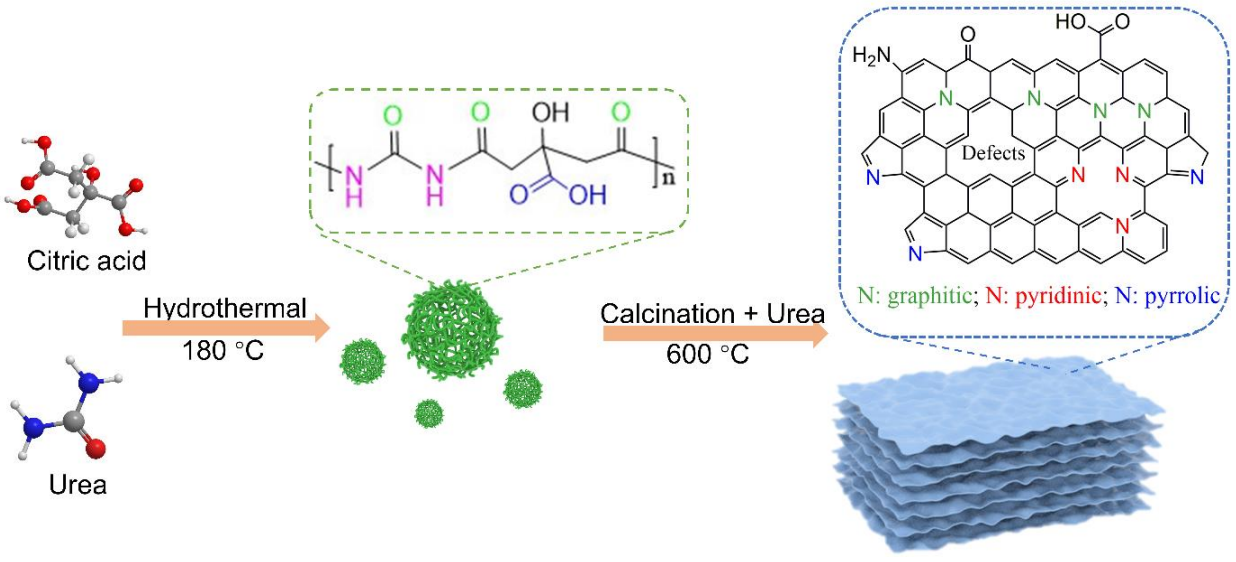

Fig. 1. Illustration of synthesis of metal-free N doped carbon.

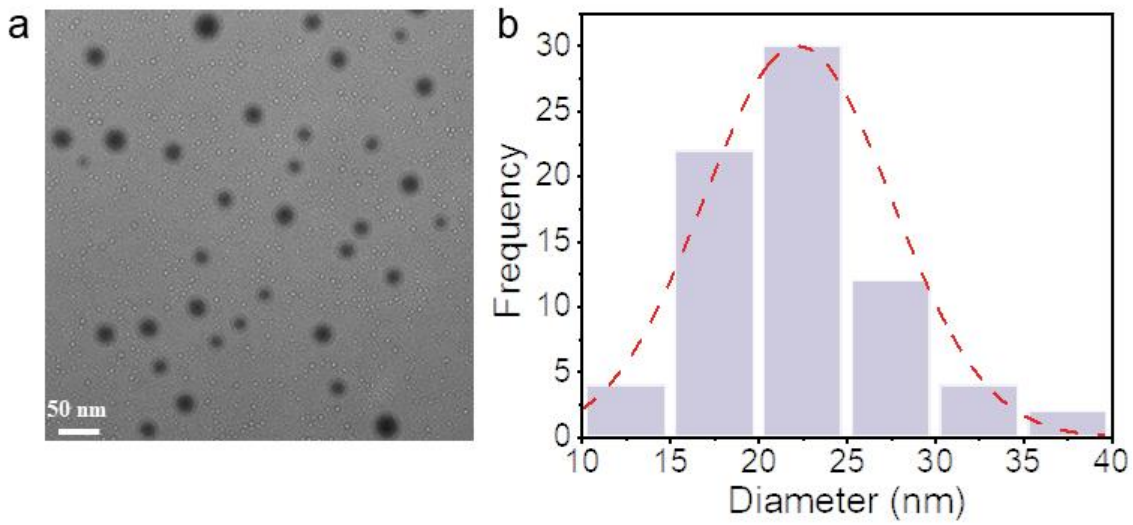

Fig. 2. (a) TEM image and (b) Size distribution histogram of PDs.

The morphology of N-C is displayed in TEM images. N-C demonstrated a sheet-like stacking structure with plentiful pores (**Fig. 3**a-b). Besides, the lattice spacing is estimated to be 0.35 nm (**Fig. 3**c), which corresponds to the interlayer stacking distance of graphene [20]. Further analysis in HAADF-STEM and element mapping images indicated that N-C material is mainly composed of carbon and nitrogen elements (**Fig. 3**d-f).

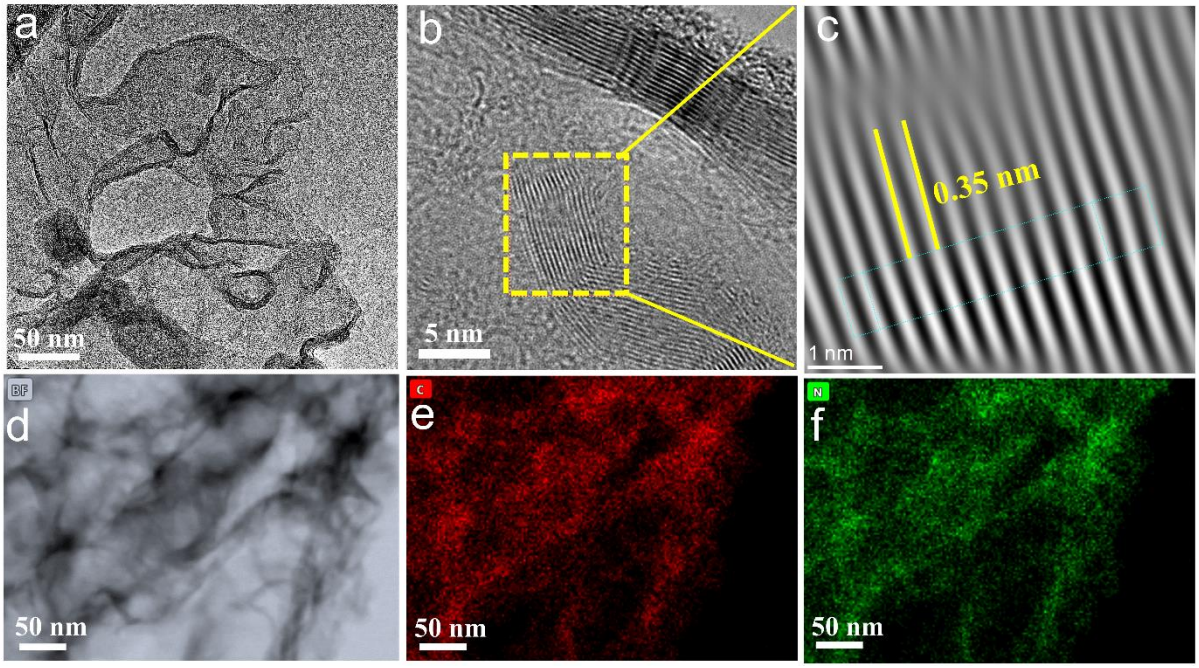

Fig. 3. (a-c) TEM images and (d) HAADF-STEM image and (e-f) EDX elemental mapping images of N-C.

XRD patterns were used to study the crystal structure of all the samples (**Fig. 4**a). CN exhibited two diffraction peaks at 13.1° and 26.7°, which were assigned to the in-plane repeating units of heptazine framework and the interlayer aromatic stacking motifs, respectively [5, 23]. Whereas the diffraction peak at 13.1° vanished after adding a certain amount of PDs in the original synthesis, and the intensity of diffraction peak at 27.4° decreased and shifted to 26.5°, meaning that a carbon material rather than CN was generated [24, 25]. Additionally, N-C displayed a similar peak with N-C ($_{CA+U}$), but exhibited a lower intensity and a larger width at half-maximum (FWHM) than G-plate and M-CNT, suggesting that a low-degree graphitization and a thinner lamellar nanostructure of N-C. These findings are consistent with TEM images, manifesting the porous and 2D thin film structure of N-C. Therefore, urea is evidenced to be transferred into N-doped carbon rather than CN when PDs are added into the polymerization process.

Raman spectra of N-C demonstrated significant differences on microstructural features from CN, G-plate and M-CNT. Two characteristic peaks at 1325 and 1558 cm^{-1} can be observed, which are ascribed to the crystal defects (D band) and the in-plane stretching sp^2 graphitic carbon (G band), respectively (**Fig. 4**b) [26, 27]. Compared with N-C ($_{CA+U}$), commercial G-plate and M-CNT, N-C exhibited a wider G band and a higher D band, indicating more defects in the carbon framework. The intensity ratios (I_D /I_G) are used to determine the proportion of defects and disordered structures in different samples. The values were 0.15, 1.07, 1.16 and 1.16 for G-plate, N-C ($_{CA+U}$), N-C and M-CNT, respectively, meaning that the graphitization degree of N-C was close to M-CNT but lower than commercial graphene plates [28]. Therefore, N-doped carbon with a portion of defects was generated after the

copolymerization of PDs and urea. By contrast, CN was acquired without PDs in the polymerization of urea.

As shown in **Fig. 4**c, the FTIR spectra of CN present the characteristic peaks at 809, 1635 cm^{-1}, corresponding to the triazine unit and CN heterocycles, and 300-3400 cm^{-1} ascribed to the amino group (N-H). Compared to CN, the N-C ($_{CA+U}$) shows the peaks at 1643 (C=N bonding) and 2098 (C=C) cm^{-1}. Meanwhile, the N-C sample revealed the presence of functional groups at 1256 (C-N bonding), 1643 (C=N bonding) and 2098 (C=C) cm^{-1}. This suggests that the surface functional groups of the N-C samples are distinct from those of CN, N-C ($_{CA+U}$), G-plate and M-CNT. Furthermore, this result confirms that the addition of PDs significantly alters the chemical structure of CN.

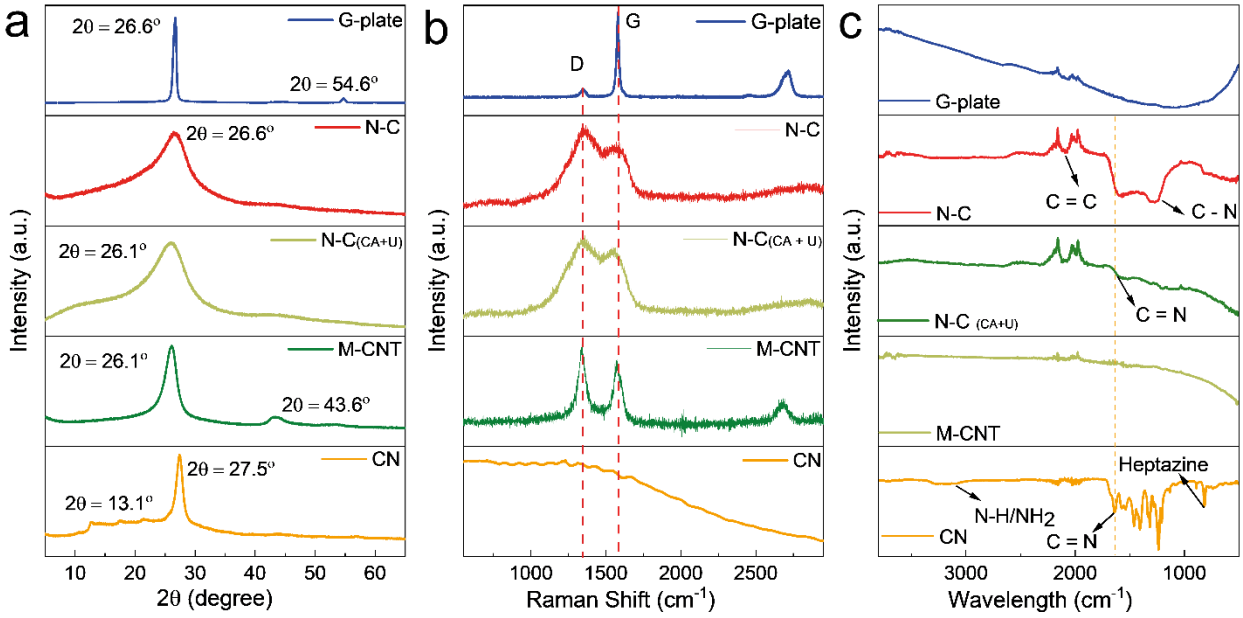

Fig. 4. Characterizations (a) XRD patterns. (b) Raman spectra. (c) FTIR spectra for CN, N-C, M-CNT, N-C ($_{CA+U}$) and G-plate.

Solid-state ^{13}C NMR spectroscopy is a powerful tool to unveil the molecular structure of the synthesized carbon materials. CN shows a dominant peak at 164 ppm, which is assigned to N-C=N in the triazine (**Fig. 6**a). Another peak at around 157 ppm is also observed,

corresponding to C-N_3 in the triazine ring of CN [28]. By contrast, N-C exhibits eight new peaks at 23.4, 48, 64.7, 107, 120, 138, 147.3 and 184.6 ppm. These are attributed to CH_3, C-N, C-O, methylene-pyridine ring, C≡N, C=C, aromatic rings, and C=O [29], respectively. Based on the results presented above, it can be inferred that the co-polymerization of PDs and urea leads to the formation of N doped carbon materials instead of CN. The findings from NMR strongly supports the idea that copolymerization of urea with PDs can produce nitrogen-doped carbon materials with different oxygen-containing functional groups.

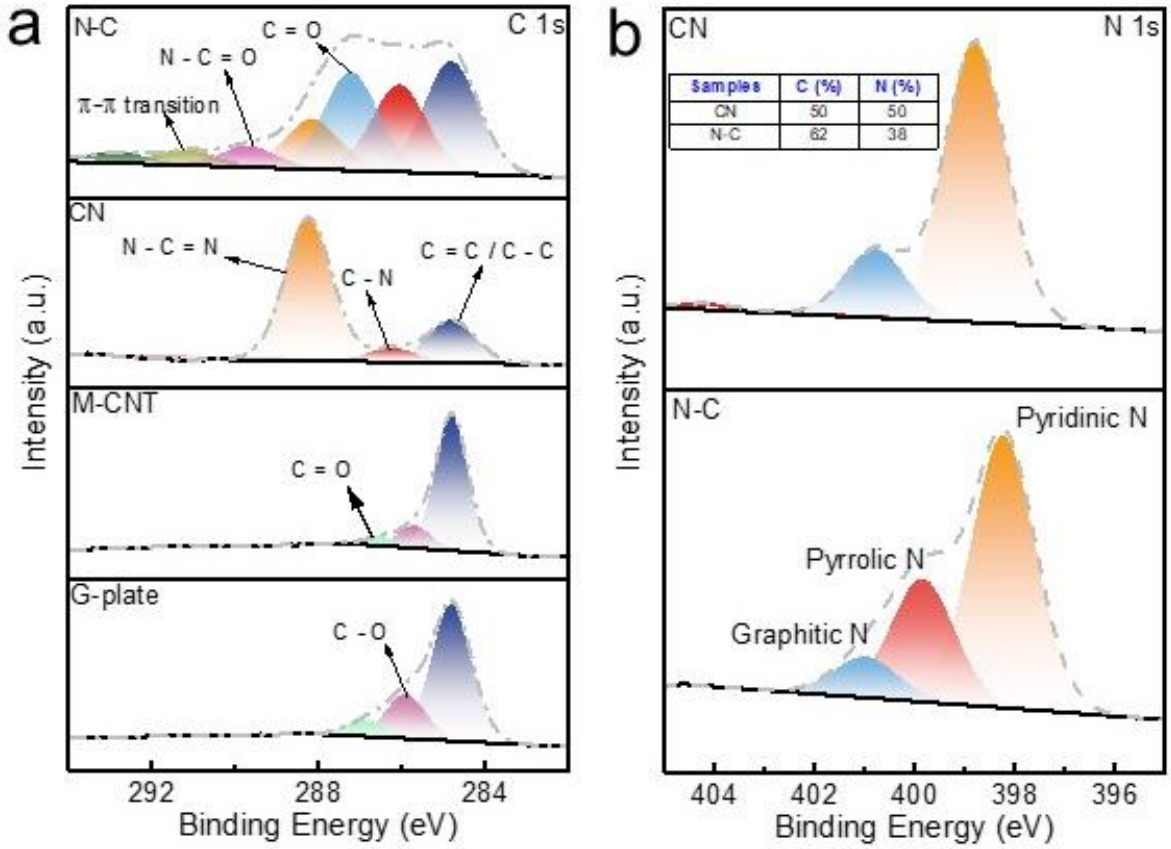

Fig. 5 High-resolution XPS spectra of (a) C 1s and (b) N 1s for N-C, CN, M-CNT and G-plate, (Inset) C and N ratio of CN and N-C.

XPS was used to further investigate the chemical states of carbon and nitrogen atoms and surface functional groups. **Fig. 5**a illustrates the XPS C 1s spectra at 284.8, 286.2 and 288.2 eV in CN, which refer to C–C / C=C, C-N and C-N=C, respectively. For M-CNT and G-

plate, the peaks at 284.8, 286, and 287 eV are C–C / C=C, C–O, and C=O, separately. In contrast, for the N-C catalyst, it presents the peaks at 284.8, 286.2, 287, 288.2, 289.66, and 291.3 eV, which are ascribed to the C–C / C=C, C-N, C=O, C-N=C, N-C=O, and π–π transition, respectively. [30]. In addition, the N 1s spectra of CN are deconvoluted into two peaks, centered at 398.2 and 401.1 eV and assigned to pyridinic N and graphitic N, respectively. Whereas three fitted peaks of N 1s can be identified on N-C, which are attributed to pyridinic N (398.2 eV), pyrrolic N (399.8 eV) and graphitic N (401.1 eV) (**Fig. 5**b) [31,32]. The difference on the type of nitrogen between N-C and CN fully confirms the formation of N doped carbon material after PDs were added in the copolymerization process. The XPS results are also consistent with the findings of NMR analysis. As such, a possible molecular structure is proposed for N-C (**Fig. 1**). It should be noted that the N content is as high as 38% in N-C, which is the highest among all the reported N-doped carbon samples (inset of **Fig. 5**b), confirming the epitaxial growth strategy in this work is effective for preparation of N-C with a high N content and structural defects.

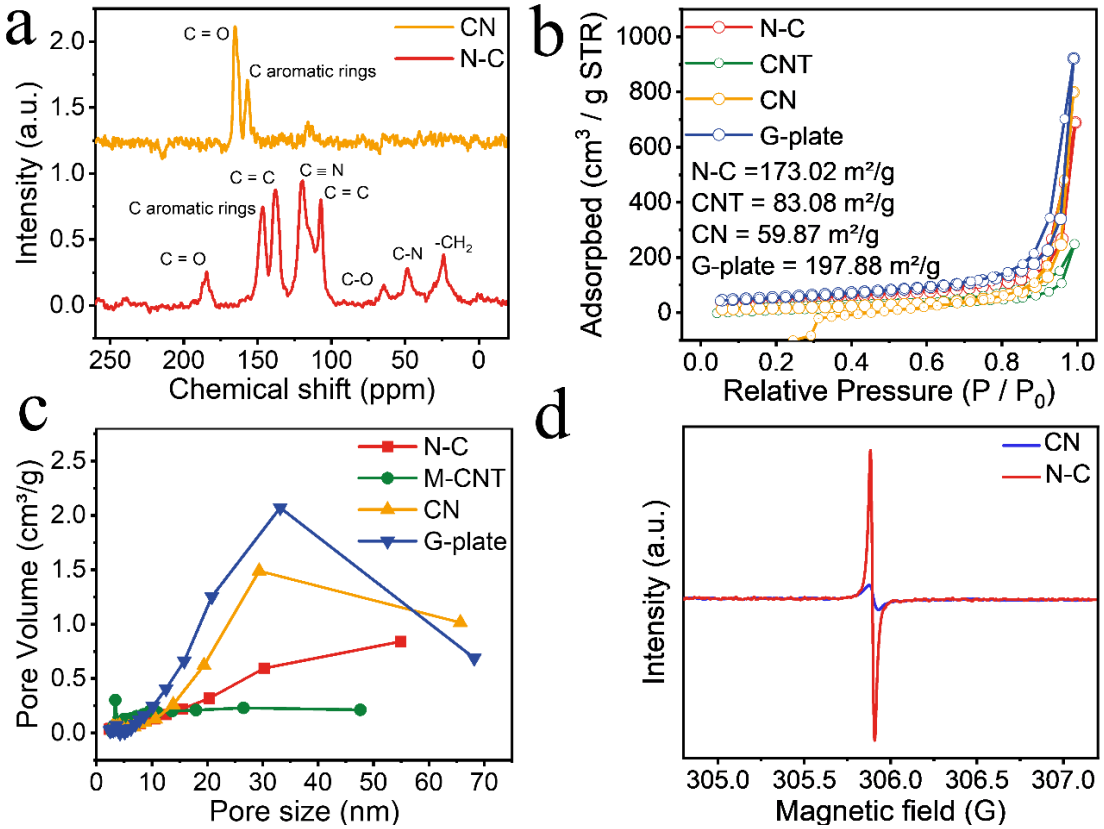

Fig. 6. (a) Solid ^{13}C NMR results for CN and N-C. (b) N_2 adsorption and desorption isotherms and (c) pore size distributions for N-C, CNT, CN and G-plate. (d) Solid EPR spectra for CN and N-C.

N_2 adsorption-desorption isotherms were used to investigate the porosity and surface area of the prepared samples. Typical IV hysteresis loops can be observed in **Fig. 6**b, indicating the presence of mesopores in all the carbon materials. The corresponding BET specific surface areas (S_{BET}) of N-C, G-plate, CN and CNT are 173, 197.9, 59.9 and 83.1 m^2/g, respectively (**Fig. 6**b). As shown in **Fig. 6**c, the pore size distributions determined by the BJH desorption method revealed that the pore sizes are located at 25-35 nm for all of samples (**Fig. 6**b-c).

EPR spectra were collected to study the electronic structure of CN and N-C materials, The solid EPR spectra of both the samples display a significantly paramagnetic signal at a g factor of 2.003, which is attributed to the presence of unpaired electrons. Compared with CN, an intensified peak can be observed on N-C, owing to the different electronegativities between carbon and nitrogen atoms (**Fig. 6**d). The findings indicate that electronic polarization can be engineered through the uneven introduction of nitrogen dopants and creation of structural defects, resulting in the formation of high charge density on N-C.

Performance of PMS activation for 1,4-DHP removal

The catalytic performances of the obtained catalysts were evaluated in PMS activation for the degradation of 1,4-DHP. The results showed that only 18% of 1,4-DHP was removed within 60 mins in the absence of a catalyst, implying that the inactivated PMS oxidant was almost unable to react with 1,4-DHP (**Fig. 7**a). When only the N-C catalyst was added, a 15% removal rate of 1,4-DHP was obtained, suggesting that the catalyst alone is insufficient for the oxidation of 1,4-DHP. However, the combination of PMS and catalysts significantly enhanced the removal efficiency of 1,4-DHP. The efficiency is 30% for N-C ($_{CA+U}$), 65% for M-CNT, and 20% for the G-plate, indicating that pure carbon has the lowest catalytic

activity. By contrast, N-C presented the highest degradation efficiency for 1,4-DHP in PMS system, with a 100% degradation efficiency of 1,4-DHP achieved within 20 minutes. This suggests that N-C significantly enhances the catalytic activity in PMS activation to degrade 1,4-DHP through increasing N-dopant active sites and defects. These results suggest that the N-dopant and defects on N-C play crucial roles in enhancing the catalytic activity of N-C, while the highly graphitized carbon of G-plate showed low catalytic activity and efficiency in PMS activation and 1,4-DHP degradation.

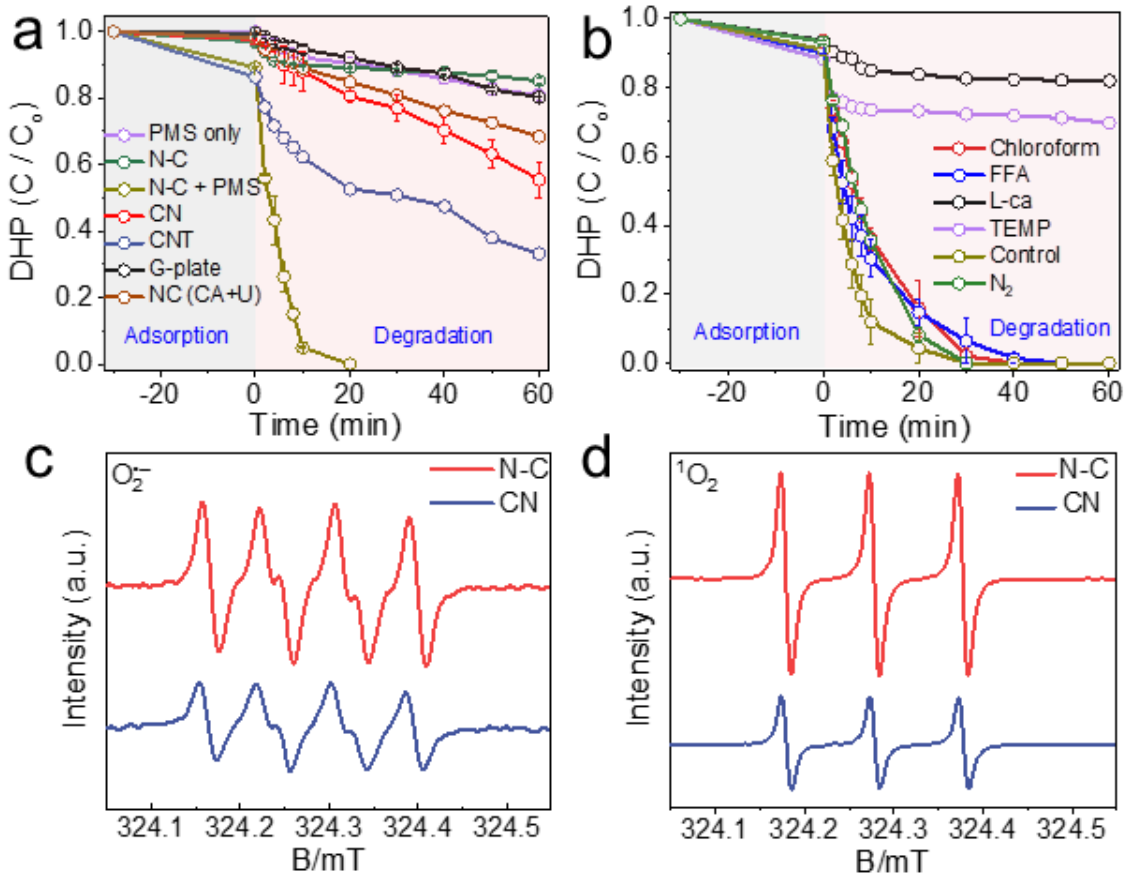

Fig. 7. (a) Degradation efficiency of CN, N-C, M-CNT, and G-plate, catalyst amount = 0.05 g / L; PMS dosage = 0.2 mM; 1,4 DHP concentration = 25 ppm. (b) Trapping experiments with different scavengers in PMS activation for degradation of 1,4-DHP using N-C as the catalyst. Chloroform = 1 mM, FFA = 1 mM, L-ca = 1 mM, TEMP = 1 mM, EPR measurements for monitoring. (c) $O_2^{\bullet-}$ (DMPO) and (d) $^1O_2$ (TEMPO) in PMS activation process for degradation of 1,4-DHP.

Identification of reactive oxygen species in N-C/PMS system for 1,4-DHP removal

Quenching experiments were conducted to investigate the intrinsic reactive oxygen species (ROS) in the PMS activation process for the degradation of 1,4-DHP. •OH, $SO_5^{\bullet-}$ and $SO_4^{\bullet-}$ are generally produced in a PMS activation process. However, in this experiment, both the •OH and $SO_4^{\bullet-}$ radicals were quenched because ethanol was present in the solvent. Therefore, their contributions to the removal of 1,4-DHP can be ignored. Although ethanol is present in the solvent, the efficiency of degradation is still high in N-C/PMS system, meaning that $^1O_2$, $O_2^{\bullet-}$ and e^- may contribute to the degradation of 1,4-DHP. As such, quenchers (1 mM) are added into the reactive system to analyze the contribution of ROS to the degradation of 1,4-DHP. L-ac or chloroform was added in N-C/PMS system to capture $O_2^{\bullet-}$, and FFA or TEMP was added as for trapping $^1O_2$. The removal efficiency of 1,4-DHP sharply decreased from 100% to 17% and 27% after the addition of TEMP and L-ca, respectively (**Fig. 7**b). This suggests that both $^1O_2$ and $O_2^{\bullet-}$ have significant impacts on 1,4-DHP removal in the N-C/PMS system. Besides, the reactive efficiency was effectively impeded when either FFA or chloroform was added in the degradation system (**Fig. 7**b), fully proving $^1O_2$ and $O_2^{\bullet-}$ are the dominated ROS in the degradation of 1,4-DHP.

Additionally, EPR measurement was performed to in situ monitor the ROS in the N-C/PMS based degradation system. Characteristic peaks of DMPO-$O_2^{\bullet-}$ are presented in **Fig. 7**c with an intensity ratio of 1:1:1:1, suggesting the production of $O_2^{\bullet-}$. In addition, TEMP was selected as a spin trapping agent for identification of $^1O_2$. A triplet signal with an intensity ratio of 1:1:1 was observed in the N-C/PMS/1,4-DHP system (**Fig. 7**d), verifying the contribution of $^1O_2$ to the degradation of 1,4-DHP. Therefore, both $^1O_2$ and $O_2^{\bullet-}$ species are proven to be the main ROS in the process of PMS activation for the removal of 1,4-DHP.

To unveil the pathways for the formation of $^1O_2$ and $O_2^{\bullet-}$ in this reactive system, a controlled experiment was conducted under nitrogen bubbling to remove dissolved oxygen (DO) from

the reactive solvents. The 1,4-DHP removal efficiency was significantly decreased, indicating that DO is the main source for $^1O_2$ and $O_2^{\bullet-}$ (**Fig. 7**b). Considering the more unpaired electrons on N-C, it can be inferred that N-C acted as an electron donor to DO for the generation of $O_2^{\bullet-}$. On the other hand, the HSO_5^- as acceptor receiving electron from N-C to become $HSO_5^{\bullet-}$. Moreover, the generated $O_2^{\bullet-}$ will further react with $HSO_5^{\bullet-}$ to generate $^1O_2$ and oxide the 1,4-DHP. The resulting $O_2^{\bullet-}$ and $^1O_2$ finally oxidize 1,4-DHP radical to realize the degradation of 1,4-DHP. Therefore, the reactive mechanism of PMS activation for the degradation of 1,4-DHP is presented in **Scheme 1**.

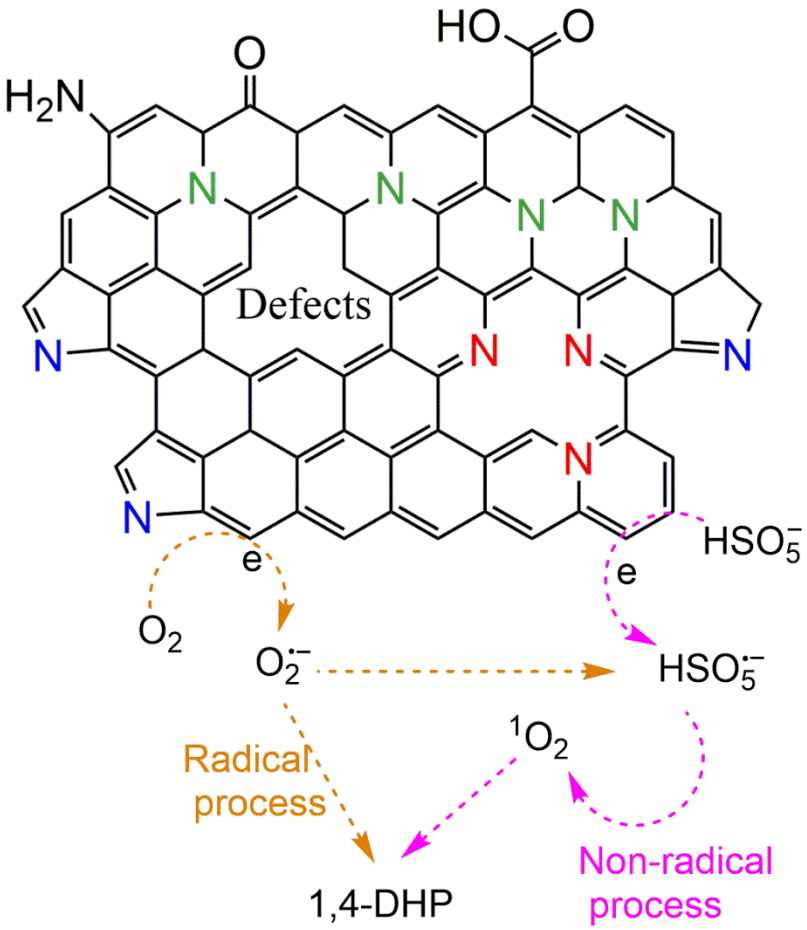

Scheme 1. Proposed mechanism of PMS activation for the degradation of 1,4-DHP.

Conclusion

In summary, we utilized a facile and effective approach to synthesize nitrogen riched carbon materials at relatively low temperature. The resulting N-C exhibited abundant N dopant and structural defects compared with commercial graphene and multi-wall carbon nanotube. Characterization results confirmed that urea grew along the functional groups on the surface of PDs to form N-doped carbon. Moreover, the obtained N-doped carbon catalyst exhibited the best removal efficiency for 1,4-DHP in the PMS activation system. Quenching experiments and EPR measurement collectively analyzed the degradation mechanism of 1,4-DHP in N-C/PMS system and revealed the main active species of $^1O_2$ and $O_2^{\bullet-}$. This work provides in-depth insights into the manufacture of highly active N-C materials for environmental remediation.

References

[1] X.J. Wei, L. Wang, W.L. Jia, S.F. Du, L.Z. Wu, Q. Liu, Metal-free-mediated oxidation aromatization of 1,4-dihydropyridines to pyridines using visible light and air, Chinese J. Chem. 32 (2014) 1245-1250.

[2] K.K. Borowicz, M. Gasior, Z. Kleinrok, S.J. Czuczwar, Influence of isradipine, niguldipine and dantrolene on the anticonvulsive action of conventional antiepileptics in mice, Eur. J. Pharmacol. 323 (1997) 45-51.

[3] S.D. Dhengale, V.M. Naik, G.B. Kolekar, C.V. Rode, P.V. Anbhule, Solvent free, environment benign synthesis of 1,4-dihydropyridines and polyhydroquinolines by using heterogeneous Zn/MCM-41 catalyst, Res. Chem. Intermed. 47 (2021) 3263-3287.

[4] H. Saffarian, F. Karimi, M. Yarie, M.A. Zolfigol, Fe_3O_4@SiO_2@$(CH_2)_3$ -urea-quinoline sulfonic acid chloride: A novel catalyst for the synthesis of coumarin containing 1,4 dihydropyridines, J. Mol. Struct. 1224 (2021) 129294.

[5] J. Zhang, X. An, N. Lin, W. Wu, L. Wang, Z. Li, R. Wang, Y. Wang, J. Liu, M. Wu, Engineering monomer structure of carbon nitride for the effective and mild photooxidation reaction, Carbon, 100 (2016) 450-455.

[6] X.G. Duan, Z.M. Ao, D.G. Li, H.Q. Sun, L. Zhou, A. Suvorova, M. Saunders, G.X. Wang, S.B. Wang, Surface-tailored nanodiamonds as excellent metal-free catalysts for organic oxidation, Carbon 103 (2016) 404-411.

[7] X.G. Duan, H.Q. Sun, M. Tade, S.B. Wang, Metal-free activation of persulfate by cubic mesoporous carbons for catalytic oxidation via radical and nonradical processes, Catal. Today 307 (2018) 140-146.

[8] J.L. Wang, S.Z. Wang, Activation of persulfate (PS) and peroxymonosulfate (PMS) and application for the degradation of emerging contaminants, Chem. Eng. J. 334 (2018) 1502-1517.

[9] X.G. Duan, C. Su, J. Miao, Y.J. Zhong, Z.P. Shao, S.B. Wang, H.Q. Sun, Insights into perovskite-catalyzed peroxymonosulfate activation: maneuverable cobalt sites for promoted evolution of sulfate radicals, Appl. Catal. B: Environ. 220 (2018) 626-634.

[10] X.G. Duan, H.Q. Sun, Z.M. Ao, L. Zhou, G.X. Wang, S.B. Wang, Unveiling the active sites of graphene-catalyzed peroxymonosulfate activation, Carbon 107 (2016) 371-378.

[11] A.B. Alayande, S. Hong, Ultraviolet light-activated peroxymonosulfate (UV/PMS) system for humic acid mineralization: effects of ionic matrix and feasible application in seawater reverse osmosis desalination, Environ. Pollut. 307 (2022) 119513.

[12] W.Y. Han, D.G. Li, M.Q. Zhang, X.M. Hu, X.G. Duan, S.M. Liu, S.B. Wang, Photocatalytic activation of peroxymonosulfate by surface-tailored carbon quantum dots, J. Hazard Mater. 395 (2020) 122695.

[13] G. Nie, L. Xiao, J.X. Bi, S.B. Wang, X.G. Duan, New insight to piezocatalytic peroxymonosulfate activation: the critical role of dissolved oxygen in mediating radical and nonradical pathways, Appl. Catal. B: Environ. 315 (2022) 121584.

[14] X.G. Duan, C. Su, L. Zhou, H.Q. Sun, A. Suvorova, T. Odedairo, Z.H. Zhu, Z.P. Shao, S.B. Wang, Surface controlled generation of reactive radicals from persulfate by carbocatalysis on nanodiamonds, Appl. Catal. B: Environ. 194 (2016) 7-15.

[15] X.G. Duan, S. Indrawirawan, H.Q. Sun, S.B. Wang, Effects of nitrogen-, boron-, and phosphorus-doping or codoping on metal-free graphene catalysis, Catal. Today 249 (2015) 184-191.

[16] H.R. Li, J.Y. Tian, Z.G. Zhu, F.Y. Cui, Y.A. Zhu, X.G. Duan, S.B. Wang, Magnetic nitrogen-doped nanocarbons for enhanced metal-free catalytic oxidation: integrated

experimental and theoretical investigations for mechanism and application, Chem. Eng. J. 354 (2018) 507-516.

[17] S.H. Ho, Y.D. Chen, R.X. Li, C.F. Zhang, Y.M. Ge, G.L. Cao, M. Ma, X.G. Duan, S.B. Wang, N.Q. Ren, N-doped graphitic biochars from C-phycocyanin extracted spirulina residue for catalytic persulfate activation toward nonradical disinfection and organic oxidation, Water Res. 159 (2019) 77-86.

[18] W.J. Tian, H.Y. Zhang, X.G. Duan, H.Q. Sun, G.S. Shao, S.B. Wang, Porous carbons: structure-oriented design and versatile applications, Adv. Funct. Mater. 30 (2020) 1909265.

[19] X Yuan, S Dong, Q Zheng, W Yang, and T Huang, Novel and efficient curcumin based fluorescent polymer for scale and corrosion inhibition, Chem. Eng. J. 389 (2020) 124296.

[20] S Indrawirawan, H.Q. Sun , X. G. Duan, S. B. Wang, Low temperature combustion synthesis of nitrogen-doped graphene for metal-free catalytic oxidation, J. Mater. Chem. A 3(7) (2015) 3432-40.

[21] Zhuang Z, Giles SA, Zheng J, Jenness GR, Caratzoulas S, Vlachos DG, Yan Y. Nickel supported on nitrogen-doped carbon nanotubes as hydrogen oxidation reaction catalyst in alkaline electrolyte, Nat. Commun. 7(1) (2016) 10141.

[22]L.H. Lin, W. Ren, C. Wang, A.M. Asiri, J. Zhang, and X.C. Wang, Crystalline carbon nitride semiconductors prepared at different temperatures for photocatalytic hydrogen production, Appl. Catal. B: Environ. 231 (2018) 234-241.

[23] J.Q. Zhang, Y.G. Li, X.L. Zhao, L. Wang, H.J. Chen, S.J. Wang, X.Y. Xu, L. Shi, L.C. Zhang, Y.Z. Zhu, H.Y. Zhang, Y.Z. Liu, G. Nealon, S. Zhang, M.B. Wu, S.B. Wang, H.Q. Sun, Aligning potential differences within carbon nitride based photocatalysis for efficient solar energy harvesting, Nano Energy 89 (2021): 106357.

[24] Y.W. Gao, T. Li, Y. Zhu, Z.H. Chen, J.Y. Liang, Q.Y. Zeng, L. Lyu, C. Hu, Highly nitrogen-doped porous carbon transformed from graphitic carbon nitride for efficient metal-free catalysis, J. Hazard. Mater. 393 (2020) 121280.

[25] Y.W. Gao, Z.H. Chen, Y. Zhu, T. Li, C. Hu, New insights into the generation of singlet oxygen in the metal-free peroxymonosulfate activation process: important role of electron-deficient carbon atoms, Environ. Sci. Technol. 54 (2020) 1232-1241.

[26] W. Zhang, Y. Li, X.B. Fan, F.B. Zhang, G.L. Zhang, Y.A. Zhu, W.C. Peng, S.B. Wang, X.G. Duan, Synergy of nitrogen doping and structural defects on hierarchically porous carbons toward catalytic oxidation via a non-radical pathway, Carbon 155 (2019) 268-278.

[27] P. Liang, C. Zhang, X.G. Duan, H.Q. Sun, S.M. Liu, M.O. Tade, S.B. Wang, An insight into metal organic framework derived N-doped graphene for the oxidative degradation of persistent contaminants: formation mechanism and generation of singlet oxygen from peroxymonosulfate, Environ. Sci. Nano 4 (2017) 315-324.

[28] J. Li, Y. Zhang, X. Zhang, J. Han, Y. Wang, L. Gu, Z. Zhang, X. Wang, J. Jian, P. Xu, B. Song, Direct transformation from graphitic C_3N_4 to nitrogen-doped graphene: an efficient metal-free electrocatalyst for oxygen reduction reaction, ACS Appl. Mater. Interfaces 7 (2015) 19626-19634.

[29] T. Wang, Y Sun, L. L. Zhang , K. Q. Li, Y. K. Yi, S.Y. Song, M. T. Li, Z. A. Qiao, S. Dai, Space-confined polymerization: controlled fabrication of nitrogen-doped polymer and carbon microspheres with refined hierarchical architectures. Adv. Mater. 31(16) (2019) 1807876.

[30] W.J. Tian, J.K. Lin, H.Y. Zhang, X.G. Duan, H.Q. Sun, H. Wang, S.B. Wang, Enhanced removals of micropollutants in binary organic systems by biomass derived porous carbon/peroxymonosulfate, J. Hazard. Mater. 408 (2021) 124459.

[31] D.G. Li, X.G. Duan, H.Q. Sun, J. Kang, H.Y. Zhang, M.O. Tade, S.B. Wang, Facile synthesis of nitrogen-doped graphene via low-temperature pyrolysis: The effects of precursors and annealing ambience on metal-free catalytic oxidation, Carbon 115 (2017) 649-658.

[32] X. Chen, X.G. Duan, W.D. Oh, P.H. Zhang, C.T. Guan, Y.A. Zhu, T.T. Lim, Insights into nitrogen and boron-co-doped graphene toward high-performance peroxymonosulfate activation: maneuverable N-B bonding configurations and oxidation pathways, Appl. Catal. B: Environ. 253 (2019) 419-432.

Chapter 5 presents the conclusions and further work on the design of metal-free photocatalysts.

5.1 Conclusions

This thesis focuses on synthesis of polymer dots (PDs) and their application for environmental purification using a hydrothermal method. The low cost and environmentally friendly citric acid and urea are selected as the carbon and nitride precursors, respectively, to produce the PDs. This thesis demonstrates that PDs serve as a source of carbon rings in generating rich nitrogen dopant on the carbon surface for new functional carbon materials. The PDs not only improve the optical properties of heterojunction carbon nitride (CN) for photocatalysis, but also produce N-rich doped carbon with abundant defects, which can activate peroxymonosulfate (PMS) and remove pollutants from aqueous solutions. Based on the research presented in this thesis, the following conclusion can be drawn.

In the introduction of the thesis, the literature review primarily introduces the current background of carbon dots, including their optical characteristics and applications in the environment. It explains their adsorption, photoluminescence, and up-conversion properties. Additionally, both top-down and bottom-up fabrication methods for carbon dots are presented. Finally, the environmental applications of carbon dots are discussed, such as hydrogen production, hydrogen peroxide generation, persulfate activation, and photodegradation of contaminants in aqueous solutions.

Implanting carbon rings into carbon nitride as a 2D heterojunction photocatalyst can efficiently improve the photodegradation of naproxen in the aqueous solution. The generated carbon rings on the surface of CN significantly improve its visible light absorption, reduce its lower band gap, and lower its impedance, which facilitate the transition of electrons. The

study also reveals that both electrons and holes make a significant contribution to the removal of pollutants. It is confirmed that single oxygen ($^1O_2$) plays a role in the degradation of naproxen, and that the generation of $^1O_2$ in this reaction occurs via the energy transfer from the singlet to triplets' states, rather than relying on dissolved oxygen.

The PDs were used as nitrogen dopants on the carbon surface and can be transformed with urea into N-rich doped carbon(N-C) for activation of PMS. The ratio of doped nitrogen can be greatly increased by adding PDs. Compared to CN, the instinct structure of N-C is greatly modified, and more carbon bands are confirmed by NMR. Despite having a lower degree of graphite compared to commercial graphene plates and carbon nanotubes, N-C demonstrates excellent catalytic activity towards activating PMS and oxidizng 1,4-DHP. The quenching experiments and EPR have confirmed that the main oxygen species responsible for oxidizing 1,4-DHP are both $^1O_2$ and $O_2^{\bullet-}$.

In summary, polymer dots can serve dual roles in synthesizing two materials: CN with carbon rings and N-dopant carbonaceous catalysts. These materials can be used in photocatalytic and AOP systems to degrade pollutants in aqueous solutions. The polymer dots serve as a template in both experiments, as they can act as a carbon source to generated carbon rings on the CN and improve its optical and catalytic properties. Moreover, it can also be used as a nitrogen source doped carbon with high active ability in the PMS system to remove pollutants. Furthermore, it exhibits a high degree of N ratio compared to other previous studied N-doped carbon materials.

5.2 Future work

Although various methods and techniques have been used to synthesize carbon dots with different characteristics, there are still some issues regarding CDs that needed to be addressed in the environmental field. Firstly, the reaction mechanism, formation process, and nucleation

of CDs are still unclear due to the use of non-standard synthesis methods. To obtain high-quality CDs, large-scale and systematic manufacturing approaches are required. These CDs are anticipated to exhibit desirable characteristics in terms of their size, shape, functional groups, and crystallinity. Furthermore, a standardized purification method is necessary to achieve a high purity of the CDs. During the synthesis process of CDs, certain host molecular entities may form on their surface, which can interfere with their practical applications. In addition, the role of the photoelectric properties of CDs in catalytic reactions has not been clearly demonstrated.

To investigate the absorption and emission properties of CDs in catalytic reactions, in-situ spectroscopic techniques such as infrared and UV–vis measurements should be utilized. Moreover, the photoluminescence (PL) mechanisms of CDs are controversial due to the variety of precursors and reaction conditions used. Some researchers have reported that the PL behavior is determined by the carbon cores and fluorophores, but there is no definitive understanding of the structure of CDs. Accurately identifying the structural features of CDs is essential to fully utilize in situ diffuse reflectance infrared spectroscopy for their potential in real-life applications.

Overall, research on the application of CDs in the energy and environmental sectors is still in its infancy. The reactivity of pure CDs in the treatment of organic pollutants and the production of green fuel is not yet optimal. Further fundamental studies are needed to enhance the properties of CDs and fully realize their potential in these areas. Despite the progress made in CDs synthesis, modification, and mechanism, there remain significant opportunities for further advancement and innovation in their applications. We firmly believe that the ability to control synthesis, achieve large-scale production, and establish clear structure-activity relationships will significantly advance the applications of CDs in green catalysis and sustainability.